Doctoral Dissertation
Doctoral Program in Energy Engineering (37th Cycle)

New Processes in Aluminium Alloys

By

Elisa Fracchia
******

Supervisor:

Prof. M. Actis Grande, Supervisor

Doctoral Examination Committee:

Prof. Mattia Merlin, Referee, Università degli Studi di Ferrara

Prof. Eleonora Santecchia, Referee, Università Politecnica delle Marche

Politecnico di Torino

2024

Declaration

I hereby declare that, the contents and organization of this dissertation constitute my own original work and does not compromise in any way the rights of third parties, including those relating to the security of personal data.

Elisa Fracchia

2024

* This dissertation is presented in partial fulfillment of the requirements for **Ph.D. degree** in the Graduate School of Politecnico di Torino (ScuDo).

Abstract

This research work was funded by the Foundry Teksid S.p.A., with the aim of studying the recycling of aluminium alloy internal scraps, namely rejected parts. Teksid Aluminium is the compartment dedicated to aluminium alloy casting, is part of the Stellantis group and is located in Carmagnola (Turin, Piedmont). Teksid Aluminium is specialized in casting cylinder heads, cylinder blocks, gear boxes and suspension components through different production processes: Gravity Casting (GC), Low-Pressure Die Casting (LPDC) and High-Pressure Die Casting (HPDC).

Two alloys from Teksid production were selected for the recycling studies: AlSi7Cu0.5Mg and AlSi9Cu3(Fe).

The focus on alloy recycling represents a compelling need for the actual market, particularly the automotive market, to reduce greenhouse emissions, energy consumption and the rejected production.

Nowadays, the circular economy pushes for reducing carbon emissions: in this sense, multiple re-use of alloys without further melt treatments represents a viable alternative to reduce the carbon footprint in foundries and costs.

The primary objective of this research was to assess the recyclability of scrap alloys through a study of the alloys' mechanical properties and microstructures as a function of the scrap alloy performances after re-meltings.

Contents

In the first recycling route proposed, the gravity casting process was chosen to perform multiple castings of the alloys and evaluate the recyclability in terms of microstructures obtained. From this perspective, alloy AlSi7Cu0.5Mg, from the low-pressure die-casting production line, and AlSi9Cu3(Fe), from the high-pressure die-casting production line, were re-melted and studied. Scraps from the high-pressure die-casting process may contain a certain amount of micro-porosities that may represent a limitation in gravity casting if specific degassing processes are not performed.

Since additive manufacturing represents an attractive and highly potential new production process to realize aluminium components, the gas atomization and printing through the Laser Powder Bed Fusion (L-PBF) process were considered in order to ennoble the scrap alloy recycling, with the aim to produce powder and evaluate the mechanical properties after printing.

Al alloy AlSi9Cu3(Fe) in both ingot and scrap forms was atomized through gas atomization. The obtained powders showed excellent rheological properties and a high grade of sphericity.

The obtained powder was then printed through L-PBF. In particular, the printing process required studying the printing parameters since the alloy AlSi9Cu3(Fe) scrap represents a new alloy for the additive manufacturing sector. The selection of printing parameters leads to obtaining highly dense specimens with high mechanical properties.

Remarkably, this thesis work aims to give a strong relation between the recycling process and obtained materials/ properties. Such properties will be evaluated form an industrial applicability poin of view, to assess if a specific process/ production/ recycling route could positively affect the industrial production.

Contents

In conclusion, the thesis explores the valuable methods of recycling scraps that rise during production, suggesting promising and viable solutions to combine the themes of cost savings, circular economy, and high materials performance.

Keywords: Aluminium alloys, Gravity Casting, Re-melting, Recycling, Gas Atomization, Laser Powder Bed Fusion, Microstructure Characterization, Metal Powders, Mechanical Tests.

Contents

1 Introduction 18

1.1 General introduction 19

1.2 Aluminium-Silicon alloys in the automotive industries. Design, properties and limits 22

1.3 Recycling of Aluminium alloys: state of the art and future possibility 25

1.4 Aim of the work 28

2 AlSi9Cu3(Fe) and AlSi7Cu0.5Mg cast alloys properties 30

2.1 Introduction 31

2.2 Defects in Al-Si casting alloys 33

2.3 Intermetallic phases in cast Al-Si alloys 36

2.3.1 Iron Chinese script 36

2.3.2 β-Fe and δ-Fe phases 37

2.3.3 π-Fe phases 38

2.3.4 θ-Al_2Cu and Q-phase 39

2.4 Effect of Fe on the castability of Al-Si alloys 40

2.4.1 Why remelting? Literature results 42

2.4.2 AlSi7Cu0.5Mg for casting purposes: state-of-the-art 44

2.4.3 AlSi9Cu3(Fe) for casting purposes: state-of-the-art 46

2.4.4 Heat treatments and intermetallic phases 49

2.5 Recyclability Protocol: Gravity Casting 52

3 Additive manufacturing: AlSi9Cu3(Fe) and AlSi10Mg alloys 58

3.1 Introduction 59

3.2 Defects in AM components 62

3.3 Strengthening intermetallic phases in AM Al-Si alloys 64

3.4 AlSi10Mg: the state-of-the-art in Aluminium AM 64

3.5 AlSi9Cu3(Fe) for AM purposes 66

Contents

3.6 Heat treatment in AM Al-Si alloys 68
3.7 Recyclability protocol by atomization 70
4 Recycling AlSi7Cu0.5Mg by GC 74
4.1 Materials and Methods 76
4.1.1 Alloy feedstock and casting process 76
4.1.2 Microstructural characterizations 81
4.1.3 Mechanical tests 83
4.2 Results 84
4.2.1 Microstructural characterizations: scrap AlSi7Cu0.5Mg 84
4.2.2 Re-melting tests 86
4.2.3 Casting with variable amounts of scrap 93
4.3 Discussion 98
5 Recycling AlSi9Cu3(Fe) by GC 104
5.1 Materials and Methods 106
5.1.1 Alloy feedstock and casting process 106
5.1.2 Microstructural characterizations 108
5.1.3 Mechanical tests 108
5.2 Results 109
5.2.1 Microstructural characterizations: scrap AlSi9Cu3(Fe) 109
5.3 Discussion 124
6 Recycling AlSi9Cu3(Fe) by AM 128
6.1 Introduction 129
6.2 Materials and Methods 129
6.2.1 Alloy feedstock and atomization 129
6.2.2 Powder characterizations 132
6.2.3 L-PBF 133

Contents

6.2.4 Residual stress analysis 133
6.2.5 Heat treatments 134
6.2.6 Mechanical tests 135
6.3 Results 135
6.3.1 Powder characterizations 135
6.3.2 L-PBF 140
6.3.3 As-built microstructure 144
6.3.4 Residual stresses 146
6.3.5 Heat treatments 148
6.3.6 Mechanical properties 157
6.4 Discussion 163
7 Conclusions and Outlook 166
7.1 Results 166
7.1.1 AlSi7Cu0.5Mg 166
7.1.2 AlSi9Cu3(Fe) 167
7.1.3 Sustainability 169
7.2 Outlook 169
8 References 170

List of Figures

Figure 1. Al-Si phase diagram up to 30 wt% of Si adapted from [14].....23

Figure 2. XRD analyses of dross collected from the holding furnace.....34

Figure 3. α-Fe shapes in T1- AlSi9Cu3(Fe) alloys having different amounts of Cr. B, Blocky; E, Exploded; P, Polyhedral; and S, Star-like. Image reproduced with permission of the publisher [10] 36

Figure 4. β-Fe observed in AlSi9Cu3 alloy. Image reproduced with permission of the publisher [50].....37

Figure 5. π-Fe, Q-phase and Mg_2Si phase observed in AlSiMgCu alloy. Image reproduced with permission of the publisher [52] 38

Figure 6. Intermetallic phases θ-Al_2Cu, Q, Mg_2Si and α-Fe in alloy AlSiCuMg alloys. Image reproduced with permission of the publisher [55]. 39

Figure 7. Cooling rate vs Secondary Dendrite Arm Spacing (SDAS) with different casting processes for AlSi9Cu3 alloy. GDC, Gravity Die Casting; GSC, Gravity Sand Casting; HPDC, High-Pressure Die Casting; S, M, and L refer to different HPDC sample sizes. Image adapted from [72]. 43

Figure 8. Block-diagram. Investigation protocol 52

Figure 9. Dross and Straube Pfeiffer tests apparatus. A: Instrument; B: chamber to perform tests; C: crucible for Dross test and Straube Pfeiffer test; D: obtained sample. 53

Figure 10. Cast and mould. A: cast for mechanical samples; B: mould to cast mechanical samples; C: cast for microstructure characterizations; D: crucible used to cast samples for microstructural characterizations. 54

Figure 11. Ishikawa diagram cause-effect considered during the GC. 55

Figure 12. First set-up in recycling alloys by gravity casting. 55

Figure 13. Second set-up in recycling alloys by gravity casting. 56

Figure 14. Melting process (a), atomization (b), final powder (c) and scheme of gas atomization apparatus (d). Image reproduced with permission of the publisher [92]. 60

Figure 15. OM (a) Microstructures of HPDC alloy AlSi9Cu3(Fe) and (b) L-PBF AlSi9Cu3(Fe). Image reproduced from [110]. 68

Figure 16. OM and SEM images of L-PBF AlSi9Cu3 alloy. Image reproduced with permission of the publisher [97]. 69

Figure 17. Block-diagram. Investigation protocol 70

Figure 18. Ishikawa diagram cause-effect considered during the AM..... 71

Figure 19. Steps in recycling alloys through atomization and printing route. 72

Figure 20. AlSi7Cu0.5Mg feedstock. A: scraps; B: ingot..... 76

Figure 21. Ingot (left side) and Scraps (right side) alloys AlSi7Cu0.5Mg. A. Dross test sample; B: Straube Pffeifer sample..... 77

Figure 22. Casted samples and mould. A: samples for mechanical tests; B: mould for casting samples for mechanical tests; C: sample for microstructural analyses; D: crucible used for casting samples for microstructural analyses. 78

Figure 23. Manual gravity casting. A: casting procedure; B: cast for mechanical samples; C: mould for mechanical samples. 79

Figure 24. Subsequent melting steps in cast AlSi7Cu0.5Mg alloy. 81

Figure 25. Optical microscope images, magnification 500 X (marker 30 μm). Intermetallic phases in AlSi7Cu0.5Mg. A: ingot alloy; B: scrap alloy. On the bottom side, details of intermetallic phases observed by SEM. 85

Figure 26. DSC thermograms. A: ingot alloy AlSi7Cu0.5Mg. B: scrap alloy AlSi7Cu0.5Mg. 85

Figure 27. DSC. Heating curves in re-melted samples. 87

Figure 28. SEM-EDS analyses in re-melted specimens type ‘a’ 89

Figure 29 SEM-EDS analyses in re-melted specimens type ‘b’ 90

Figure 30. SEM-EDS analyses in re-melted specimens type ‘c’. 91

Figure 31. SDAS results in box plot for AlSi7Cu0.5Mg alloy with and without Cr additions after different re-melting steps. 91

Figure 32. Microhardness values in re-melted specimens. 92

Figure 33. Box plots micro-hardness for each sample. 1, 2 and 3 indicate the re-melting steps. 93

Figure 34. Microstructures of samples. a: 100 % ingot alloy; b: 25 % scrap; c: 50% scrap; d: 75 % scrap and e:100 % scrap. 94

Figure 35. Details on intermetallic phases in alloys AlSi7Cu0.5Mg (OM images). 94

Figure 36. Box plot of micro-hardness measures 95

Figure 37. Box plots for tensile test results. 96

Figure 38. Fracture surfaces in tensile specimens. 97

Figure 39. Box plot for impact test results. 98

Figure 40. Fracture surfaces in impact test samples 98

Figure 41. Upper images: details of eutectic silicon change during re-melting of AlSi7Cu0.5Mg. Lower images: details of intermetallic phase change during progressive re-melting of AlSi7Cu0.5Mg 99

Figure 42. Upper images: details of eutectic silicon change during re-melting of AlSi7Cu0.5Mg plus 1 wt% Cr. Lower images: details of intermetallic phase change during progressive re-melting of AlSi7Cu0.5Mg plus 1 wt% Cr.....100

Figure 43. Upper images: details of eutectic silicon change during re-melting of AlSi7Cu0.5Mg plus 1 wt% Cr. Lower images: details of intermetallic phase change during progressive re-melting of AlSi7Cu0.5Mg plus 1 wt% Cr.....100

Figure 44. Main effect calculated by Minitab. Effect of Cr amount and Re-melting on SDAS. Cr: -1 indicates no Cr, 0 indicates 1 wt% Cr, 1 indicates 2 wt% Cr. Re-melt: -1 indicates first re-melt, 0 indicates the second re-melt and 1 indicates the third re-melt. 101

Figure 45. Main effect calculated by Minitab. Effect of Cr amount and Re-melting on Eutectic micro-hardness. Cr: -1 indicates no Cr, 0 indicates 1 wt% Cr, 1 indicates 2 wt% Cr. Re-melt: -1 indicates first re-melt, 0 indicates the second re-melt and 1 indicates the third re-melt. 101

Figure 46. Probability plot for micro-hardness 102

Figure 47. Probability plots for tensile properties.....103

Figure 48. Probability plots for absorbed energy (impact tests) 103

Figure 49. AlSi9Cu3(Fe) feedstock. Left side: scrap; right side: ingot 107

Figure 50. Optical microscope images, magnification 500 X (marker 30 μm). A: ingot AlSi9Cu3(Fe); B: scrap AlSi9Cu3(Fe). On the bottom side, details of intermetallic phases observed by SEM.....110

Figure 51. Qualitative scheme of Sludge Factor SF versus melt temperature. Adapted from [134]. 111

Figure 52. Dross test results – Scrap (left side) and ingot (right side) AlSi9Cu3(Fe) alloy. Numbers indicate different intermetallic phases. 1: α-Al; 2: Sieu; 3: Cu-containing phases; 4: Fe-containing phases; 5: β-Fe. Yellow arrows indicates sludge particles noticed on the dross test surfaces. 112

Figure 53. DSC. Heating curves in: A, ingot alloy AlSi9Cu3(Fe). B, scrap alloy AlSi9Cu3(Fe).....112

Figure 54. Microstructures (OM) of specimens based on AlSi9Cu3(Fe) 113

Figure 55. Intermetallic phases in alloy AlSi9Cu3(Fe) type 1 - 0.5 wt% Cr and 0.5 wt% Ni 114

Figure 56. Intermetallic phases in alloy AlSi9Cu3(Fe) type 2 - 1 wt% Cr and 1 wt% Ni 115

Figure 57. Intermetallic phases in alloy AlSi9Cu3(Fe) type 3 - 1 wt% Cr ..116

Figure 58. Intermetallic phases in alloy AlSi9Cu3(Fe) type 4 – 0.5 wt% Cr 117

Figure 59. Intermetallic phases in alloy AlSi9Cu3(Fe) type 5 – 0.5 wt% Ni 118

Figure 60. Intermetallic phases in alloy AlSi9Cu3(Fe) type 6 – 1 wt% Ni .119

Figure 61. SDAS results in box plot.....120

Figure 62. Box plot of micro-hardness measures: (left side: α-Al results, right side: eutectic results).....121

Figure 63. SEM images - samples' surfaces after pin-on-disk tests 122

Figure 64. Average values of COF and wear rate. 123

Figure 65. A: Wear rate vs COF, B: COF vs eutectic micro-hardness and C: specific weight vs lost weight. 124

Figure 66. Details of eutectic region change during re-melting of AlSi9Cu3(Fe). Numbers indicates specimen types. Details of eutectic silicon in scrap component were reported. 125

Figure 67. Main effect plots micro-hardness vs Cr/ Ni amount (left side) and SDAS vs Cr/ Ni amount (right side). 126

Figure 68. Main effect plots wear rate vs Cr/ Ni amount (left side) and COF vs Cr/ Ni amount (right side).....126

Figure 69. Bluish patina and oxide skins into the Alumina crucible after atomization of ingot AlSi9Cu3(Fe). 130

Figure 70. Main PSD size in first ingot and scrap powder atomization at different inlet pressures.....131

Figure 71. SEM-BSD images of the two alloy powder batches.....131

Figure 72. Residual stress analysis. Directions of analyses and analyzed points 134

Figure 73. PSD and SEM images of powders. Left side: scrap powders. Right side: ingot powders. 137

Figure 74. Qualitative Radar diagram and obtained rheological parameters in scrap powder, ingot powder (EN AC 46000) and state-of-the-art AlSi10Mg powder [149]. 138

Figure 75. XRD in ingot and scrap powders (20-63 μm size). 139

Figure 76. SEM-EDS analysis. Intermetallic compositions 140

Figure 77. Printing setup. Microstructures (OM) and density percentage. First setup (left side) power vs hatch distance; second setup (right side) point distance vs exposure time. 142

Figure 78. L-PBF specimens. a) tensile specimens; b) cubs with pins; c) impact samples (bars). 143

Figure 79. L-PBF specimens. Defects during printing 143

Figure 80. Optical Microscope images of the two alloys in the as-built state. 144

Figure 81. SEM images - ingot and scrap specimens printed by L-PBF. 145

Figure 82. Details in L-PBF scrap sample (as-built). Melt pools (left side) and cellular structure (right side). 146

Figure 83. Residual stress measures on L-PBF ingot dog bone specimen ... 147

Figure 84. Residual stress measures on L-PBF ingot bar specimen 147

Figure 85. Eutectic Silicon evolution in T6 heat treatments at 470 °C and 515 °C 148

Figure 86. Effect of different solution temper temperatures on the silicon particle dimension and intermetallic phases. 149

Figure 87. SEM-BSE electron images at 500x magnification. Porosities arise after heat treatments. 150

Figure 88. Relation between micro-hardness and ageing times. Box plots for T6 heat treatments at 470 °C and 515 °C solution temperatures. 151

Figure 89. Heat treatments T6, natural ageing. 152

Figure 90. Heat treatments T6, artificial ageing 6 h at 160 °C. 153

Figure 91. Heat treatments T6, artificial ageing 12 h at 160 °C. 154

Figure 92. Heat treatments T6, artificial ageing 18 h at 160 °C. 154

Figure 93. Heat treatments T6, artificial ageing 24 h at 160 °C 155

Figure 94. Microstructure of ingot and HPDC scrap before and after T6 HT. 156

Figure 95. Mechanical test results – $R_{p0,2}$, R_m, A% and absorbed energy (average values). 159

Figure 96. Fracture surfaces in tensile test specimens. 160

Figure 97. Boxplot for L-PBF_Scrap samples. Mechanical properties with the platform at 30 °C or 165 °C (average values).....161

Figure 98. Fracture surfaces in impact test specimens. 162

Figure 99. Main effects. Effects of process parameters on samples density 163

List of Tables

Table 1. Aluminium alloys nomenclature. 20

Table 2. Literature research. Use of alloys AlSi7Cu0.5Mg, AlSi9Cu3(Fe) and AlSi10Mg in ingot and scrap form in different production processes. 22

Table 3. Recycling routes followed in the research.....29

Table 4. Defects in cast Aluminium-Silicon alloys. 35

Table 5. AlSi7Cu0.5Mg composition limits - standard BS EN 1706:202 + A1:2021 44

Table 6. Properties of Alloy AlSi7Cu0.5Mg - standard BS EN 1706:202 + A1:2021. 45

Table 7. AlSi9Cu3(Fe) composition limits - standard BS EN 1706:202 + A1:2021 47

Table 8. Properties of Alloy AlSi9Cu3(Fe) - standard BS EN 1706:202 + A1:2021. 48

Table 9. Intermetallic phases in Cast Al-Si alloys.....52

Table 10. Defects in L-PBF 63

Table 11. Literature L-PBF printing parameters AlSi10Mg 65

Table 12. AlSi10Mg composition designed for additive manufacturing 66

Table 13. Literature L-PBF printing parameters AlSi9Cu3 67

Table 14. AlSi9Cu3(Fe) composition designed for additive manufacturing..67

Table 15. Intermetallic phases in AM Al-Si alloys 69

Table 16. AlSi7Cu0.5Mg compositions measured through SEM-EDS 77

Table 17. Metallic Cr powder. Physical and chemical properties (producer data). 78

Table 18. AlSi7Cu0.5Mg remelting tests. Roman numerals indicate the number of re-melting. (Type 1 samples). 80

Table 19. AlSi7Cu0.5Mg cast with variables charge. (Type 2 samples). 81

Table 20. Recyclability Protocol and tests on AlSi7Cu0.5Mg alloy 83

Table 21. Peaks observed in DSC analyses of alloys AlSi7Cu0.5Mg. 86

Table 22. Microstructures in re-melted specimens AlSi7Cu0.5Mg 88

Table 23. AlSi9Cu3(Fe) compositions provided by Teksid S.p.A. 106

Table 24. Metallic Ni powder. Physical and chemical properties provided by the producer. 107

Table 25. Castings compositions 107

Table 26. Recyclability Protocol and tests on AlSi9Cu3(Fe) alloy 108

Table 27. Measured densities 120

Table 28. L-PBF print parameters in AlSi9Cu3(Fe) 133

Table 29. Powder composition measured through SEM-EDS 136

Table 30. L-PBF parameters 143

Table 31. L-PBF samples composition measured through SEM-EDS 145

Table 32. Mechanical properties of L-PBF and HPDC AlSi9Cu3 from literature. 158

Table 33. Comparison of energy density of scrap alloy AlSi9Cu3(Fe) and state of the art in AlSi10Mg and AlSi9Cu3 164

Abbreviations

AM	**A**dditive **M**anufacturing
BSD	**B**acks**s**catter **D**etector
EDX	**E**nergy **D**ispersive **X**-Rays
GC/ GDC	**G**ravity **C**asting/ **G**ravity **D**ie **C**asting
HPDC	**H**igh **P**ressure **D**ie **C**asting
LPBF	**L**aser **P**ower **B**ed **F**usion
OM	**O**ptical **M**icroscope
SEM	**S**canning **E**lectron **M**icroscope
SE	**S**econdary **E**lectrons
SSSS	**S**uper **S**aturated **S**olid **S**olution

Chapter 1

1 Introduction

This chapter introduces the use of Aluminium Alloys with the main focus on the automotive sector. The main alloying elements and the crucial topic of recycling are introduced.

The last part of this introductive chapter depicts the aim of the work.

1.1 General introduction

The utilization of aluminium alloys in automotive manufacturing has experienced a significant surge in recent years owing to their combination of properties and benefits. From enhanced fuel efficiency to improved performance and sustainability, aluminium alloys have become a cornerstone material in the automotive sector [1].

Aluminium cast alloys are crucial to modern automotive manufacturing, offering significant benefits in weight reduction, fuel efficiency, and performance enhancement. Despite challenges, ongoing advancements in alloy development and processing techniques continue to expand the Al application in the automotive industry.

Three main types of aluminium alloys are used in automotive: Al-Cu, Al-Mg, and Al-Si.

- Aluminium-copper alloys are mainly used in automotive for high-strength applications, like suspension components. Such alloys can offer superior mechanical properties after the heat treatment, thanks to the high Cu amount.
- Aluminium-magnesium alloys are used to produce wheels, structural components, and chassis parts. They can offer high ductility and high corrosion resistance.
- The more diffused cast alloys are the aluminium-silicon ones. They are mainly used to cast engine blocks, cylinder heads and transmission cases. Overall, such alloy compositions are characterized by high thermal conductivity, good wear resistance and good castability. Moreover, the Al-Si alloys can be alloyed with elements such as Cu and Mg, making them heat-treatable for achieving higher mechanical properties.

All the aluminium cast alloys are reported in ASTM B179 – 18 [2] and BS EN 1706:2020+A1:2021 [3] standards, along with their attended chemical composition and the suggested casting process.

The most common designations of Al alloys are the Aluminium Association designation and the European designation, as shown in **Table 1**.

Table 1. Aluminium alloys nomenclature.

EN (European)		**Aluminium Association (American)**	
1xxxx	> 99,50% Aluminium	*1xx.x*	> 99 % Aluminium
2xxxx	Al-Cu	*2xx.x*	Al-Cu
4xxxx	Al-Si / Al-Si-Cu / Al-Si-Mg	*3xx.x*	Al-Si-Cu / Al-Si-Mg
5xxxx	Al-Mg	*4xx.x*	Al-Si
7xxxx	Al-Zn-Mg	*5xx.x*	Al-Mg
8xxxx	Others (Al-Mg-Fe, Al-Li-Cu)	*7xx.x*	Al-Zn
9xxxx	Experimental	*8xx.x*	Al-Sn
		9xx.x	Others

As the demand for aluminium components continues to increase, recycling such alloys becomes imperative to reduce emissions from bauxite extraction and companies' internal waste [4]. From such a perspective, alloy recycling in the automotive sector is assumed to be highly important. Currently, traditional casting processes are optimized, but production scraps are still present, and such rejected parts are usually re-inserted into the production lines. In fact, variations in casting defect types and amounts may be noticed even if castings are produced by the same process conditions, indicating the stochastic nature of defects. Conversely, old scraps coming from end-of-life products are collected and melted. If necessary, the melt is treated with casting agents, alloyed, and then cast in ingot forms. After such steps, ingots are ready to be delivered to foundries for use in a new casting process.

Notably, in literature, aluminium silicon alloys were recycled through different processes. The main techniques used in the recycling process are conventional recycling (CR), semi-direct recycling (SDR) and direct recycling (DR) [5]. Conventional recycling, as explained in 1.3, involves the melt of the alloy to generate a secondary ingot. Such secondary ingot has a specific chemical composition aligned with international standards. Semi-direct recycling is a solid-state technique that involves mandatory pre-processing before the primary recycling process to recycle aluminium chip scraps. Such processes include powder metallurgy, hot extrusion, and spark plasma sintering. Finally, direct recycling is a solid-state recycling process involving the direct recycling of scraps.

In additive manufacturing technology, the Laser Powder Bed Fusion L-PBF process is used to produce complex-shaped components. From this perspective, the use of Al powder is promising mainly thanks to its high thermal conductivity and lightweight. The most printable alloys are the AlSiMg alloys, but other types of alloys can be successfully printed: AlCu alloys Ti containing, AlMg alloys called Scalmalloy ® [6] and AlZn alloys with high Zn amount [7]. Conversely, a few drawbacks limit the Al powder diffusion in L-PBF. Such drawbacks are the low flowability, the surface oxide on the powder and the low absorptivity of the Al powder at the wavelength of the leading laser sources. As wrought alloys regard, there are difficulties in processing high-strength wrought Al-alloys by PBF because they suffer solidification cracking. Moreover, such alloys contain volatile elements such as Mg, Zn and Li that can evaporate during the L-PBF, affecting the final properties of the printed component.

Recently, the use of L-PBF instead of HPDC to produce automotive components was considered by [8], despite the comparison performed between an automotive HPDC component made by AlSi9Cu3(Fe) and a L-PBF part printed in AlSi10Mg.

In this work, the alloys studied come from the automotive scrap chain and are the AlSi7Cu0.5Mg and AlSi9Cu3(Fe) alloy.

Table 2 summarises the processes used in literature for the alloy compositions object of this work.

Table 2. Literature research. Use of alloys AlSi7Cu0.5Mg, AlSi9Cu3(Fe) and AlSi10Mg in ingot and scrap form in different production processes.

Alloy	Processes		
	GC	**HPDC**	**L-PBF**
AlSi7Cu0.5Mg (ingot)	✓ [9]	×	×
AlSi7Cu0.5Mg (scrap)	×	×	×
AlSi9Cu3(Fe) (ingot)	✓ [10]	✓ [11]	×
AlSi9Cu3(Fe) (scrap)	×	✓ [12]	×

1.2 Aluminium-Silicon alloys in the automotive industries. Design, properties and limits

In the automotive sector, Aluminium Silicon alloys are largely diffused: their unique blend of lightweight, strength, wear resistance, and thermal stability makes Al-Si alloys key materials in the automotive industry for achieving higher efficiency and better performance. Al-Si alloys have lower density than steel and iron-based alloys, making them ideal for reducing vehicle weight: this is critical for improving fuel efficiency and reducing CO_2 emissions in vehicles.

Aluminium alloys used in casting and additive manufacturing are designed to obtain specific properties as a function of the production process. The silicon content has a crucial role in alloy properties. Higher silicon content generally improves wear resistance and castability, while lower silicon content enhances

ductility and elongation. A section of the binary Al-Si phase diagram is shown in

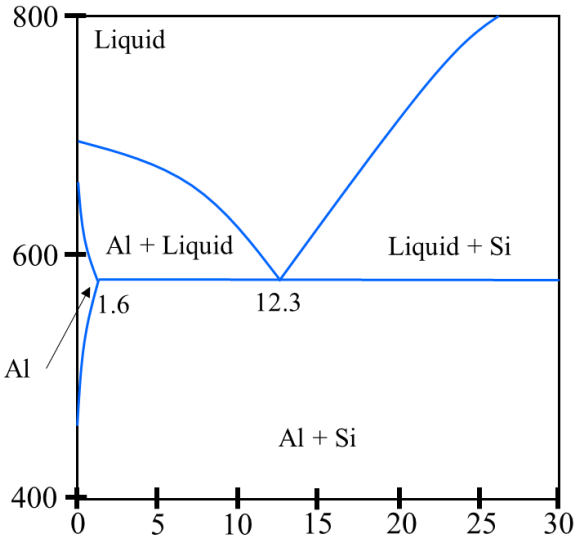

Figure 1.

The microstructure of the Al-Si alloys consists of a primary α-Al phase and eventually primary Si in hypereutectic alloys (if Si amount is up to 13 wt%), Al-Si eutectic phase, Cu-rich phases, Mg_2Si phases and Fe and Mn phases. Alloying elements can be divided into major, minor and impurity. Major alloying elements are Mg, Cu, and Zn, which are added to improve the mechanical and/ or physical properties. Even Ni can be added to increase the heat resistance and the mechanical properties by forming intermetallic compounds Al_3Ni, Al_3CuNi, and Al_7Cu_4Ni in gravity-casting compositions [13]. Such elements may form intermetallic phases during casting or after specific heat treatments. Minor alloying elements such as Sr and Ti are used to improve specific characteristics such as grain size reduction and Si shape modification. Finally, impurities, such as Fe, Pb, Sn, and Sb, are typical of recycled alloys and can affect the machinability of the alloys (Pb) or the grain size dimension (Fe).

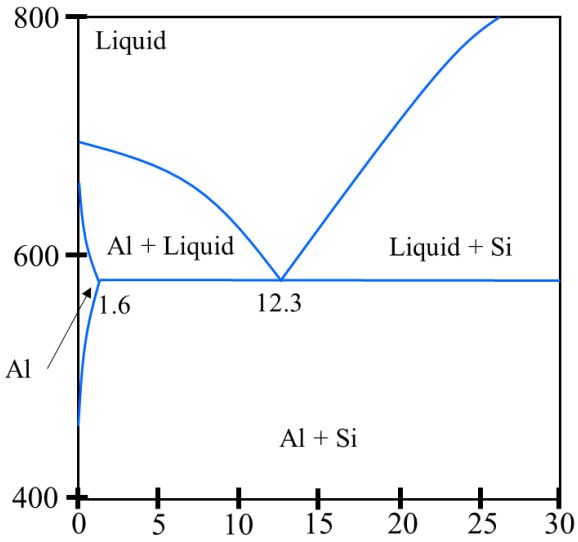

Figure 1. Al-Si phase diagram up to 30 wt% of Si adapted from [14].

Particularly, the eutectic silicon modification in casting alloys represents an essential step in producing high-quality casts. The eutectic silicon shape has a plate-like form that may affect mechanical properties; the modification treatment, on the other hand, leads to the silicon's dissolution and spheroidization. Such spheroidization can be achieved through elements acting as modifiers (Sr, Na) [15–18] or by heat treatment at high temperatures [19,20].

Hereinafter, the main effects of alloying elements in cast Al-Si alloys are reported.

- *Silicon* improves the metal castability and fluidity and reduces metal shrinkage during solidification. In the case of Al-Si hypereutectic alloys, and sometimes in eutectic and near eutectic alloys, the first phase to nucleate is the primary Si particles. Such particles are large polyhedral crystals that can then flow into the melted alloy because the silicon solubility in the aluminium matrix is negligible. Then, the Al-Si eutectic phase solidifies. Such a Si geometry is harmful and can act as a concentrator of efforts: its morphology is usually changed through chemical processes by adding modifier elements (Sr, Na, Ba) or through heat treatments. In Al-Si hypoeutectic and eutectic alloys, the first phase to solidify is the α-Al matrix. Then, the next phase to solidify is the Al-

Si eutectic, characterized by a fibrous Silicon shape. Even such Si shape must modify to avoid concentration of efforts.

- *Copper* improves the as-cast and high-temperature strength. Into the Al-Si alloy, it contributes to both matrix hardening and precipitation hardening. Copper may form intermetallic phases with Al, Al-Si and Al-Si-Mg, having blocking, eutectic or fine eutectic shapes. Moreover, Cu can form intermetallic phases with Ni, if present.
- *Nickel* is sometimes added to increase mechanical strenght, but usually, its additions is complementary to Cu. It has a straightening effect in Al-Si alloys and tends to form intermetallic phases with aluminium.
- *Magnesium* is a precipitation hardener, and the heat treatment of solubilization and artificial ageing (T6) promote the fine and homogeneous dispersion of Mg_2Si intermetallic phases, increasing the mechanical properties of the alloy.
- *Zinc* improves mechanical (mainly tensile) properties in Al-Si alloys after heat treatment, without penalising the alloy's ductility.
- *Iron* is considered an impurity in secondary Al-Si alloys, and usually, it comes from the recycling process. It forms brittle acicular shaped intermetallic phases with aluminium that acts as stress concentrators. If the iron amount is relevant, the intermetallic shape must be modified by a chemical route through Mn addition. Notably, the modification of iron compounds does not take place with heat treatments or cooling rate variations.
- *Manganese* is usually added to change the acicular Fe-Al intermetallics into Chinese-script intermetallics, which have blocky or dendritic shapes that are less harmful. Such intermetallics may increase the wear resistance of the alloy.

Mainly, aluminium alloys used in Additive Manufacturing AM are compositions already used in industrial applications. Such alloys were initially tailored to fulfil the requirements of other manufacturing routes, such as casting, and then adapted for AM. There are some indicators that must be taken into account when considering aluminium alloys in additive manufacturing. The alloys must show high castability and weldability; otherwise, it could be challenging to process them by L-PBF. This behaviour is mainly attributable to the fact that such powders are light and have high reflectivity, high thermal conductivity and low laser absorptivity of wavelength used in L-PBF [21,22]. Moreover, in alloys with Mg or Cu as the main alloying element, micro crackings may occur during the printing

process, making printing those Al alloys challenging. One of the main criteria for selecting alloys for L-PBF printing is to select alloys weldable by laser welding route because of the similarity between the two processes [23]. As previously described, the most printable AM alloys are the low-strength alloys AlSiMg near-eutectic compositions, such as AlSi10Mg. In Al-Si AM alloys, the printing parameters strongly affect the microstructures. In hypoeutectic alloys, as the alloys object of this thesis, the α-Al phase is the predominant one and solidified with epitaxial grains because of the thermal gradient due to the printing process. The Silicon is dispersed into the intergranular areas and, as the cooling rate is very fast, in such alloys metastable phases may be observed.

1.3 Recycling of Aluminium alloys: state of the art and future possibility

The recycling of aluminium alloys has become increasingly significant in the context of sustainable manufacturing and environmental issues. Aluminium recycling is a well-established process that continues to evolve thanks to the strong market demands.

According to the Aluminum Association, recycling aluminium saves up to 95% of the energy required for primary production [24]. This substantial energy saving translates into lower production costs, making recycled aluminium an economically attractive option for manufacturers.

According to the International Aluminium Institute, the global aluminium production in 2022 was approximately 65 million metric tons, with recycled aluminium accounting for around 30% of this total [25]. Collection rates for aluminium scrap are also improving, thanks to enhanced recycling programs and greater awareness. In Europe, for instance, the recycling rate for aluminium beverage cans exceeds 75%, indicating a robust infrastructure for aluminium recycling. This trend is mirrored in other regions, with North America achieving similar recycling rates [26].

One of the primary challenges in aluminium recycling is maintaining the quality of recycled material. Contaminants, such as other metals and non-metallic materials, can degrade the properties of recycled aluminium. Advancements in sorting and refining technologies are essential to address this issue, ensuring that

recycled aluminium meets the quality standards required for high-performance applications.

Modern sorting technologies, such as eddy current separators, X-ray fluorescence (XRF), and laser-induced breakdown spectroscopy (LIBS), allow for the precise separation of aluminium alloys from mixed scrap. These technologies ensure that recycled aluminium retains its desirable properties, making it suitable for high-quality applications. In the foundry industry, the use of advanced re-melting and refining processes, such as rotary furnaces and tilting rotary furnaces, has improved the yield and quality of recycled aluminium. These processes minimize metal losses and allow aluminium recovery from dross.

The first step in recycling an Al alloy is the collection of aluminium scrap. This can come from various sources, including manufacturing off-cuts, end-of-life products (such as automotive parts), and industrial waste. Such scraps are commonly referred to as new scrap or if they are production waste or 'old scrap' if they are end-of-life [27]. The scrap is typically collected through recycling programs, scrap yards, and manufacturing facilities.

Once collected, the scraps are sorted to separate aluminium alloys from other materials and contaminants. The sorted aluminium scrap is then shredded into smaller pieces to facilitate handling and processing. After shredding, the scrap undergoes a cleaning process to remove any remaining contaminants, such as oils, paints, and coatings. This is typically done through mechanical, chemical, and thermal treatments. The cleaned aluminium scrap is then fed into a furnace for re-melting. In the furnace, the aluminium scrap is melted at temperatures typically ranging from 660°C to 750°C. During the melting process, fluxes may be added to the molten metal to remove impurities and improve the quality of the final product. Fluxes are compounds that react with contaminants to form a separate slag layer that can be easily removed. Once melted, the aluminium undergoes refining to remove any remaining impurities; additional alloying elements (such as silicon, copper, magnesium or iron) may be added to adjust the molten aluminium composition to match the required specifications. Then, the casting process will take place.

As aluminium-silicon alloys regards, a strong limitation during scrap automotive alloy recycling is represented by iron. Fe is usually present in Al-Si alloys during recycling because the recycled engine blocks contain components made of cast iron. In fact, bimetallic powertrain components consisting in bot Al-

Si alloy and cast iron inserts are common, and are usually manufactured by gravity die casting [28]. On the other hand, in the end-of-life powertrain component, the cast iron must be removed before recycling; if part of it were not fully removed, becoming a contaminant in recycled alloys.

Companies that want to declare the main environmental claims of their products can do it by a self-declaration (environmental label type II), by a multicriteria system based on the assessment of the entire life-cycle of the product by an external independent organization (environmental label type I) or, finally, by LCA (Life Cycle Assessment) by an external independent organization (environmental label type III).

The legislations concerning the environment declarations of products are the 14020 series; in particular:

- UNI EN ISO 14021:2021 Environmental labels and declarations – Self-declared environmental claims (Type II environmental labelling);
- UNI EN ISO 14024:2018 Environmental labels and declarations - Type I environmental labelling - Principles and procedures;
- UNI EN ISO 14025:2010 Environmental labels and declarations - Type III environmental declarations - Principles and procedures.

The EPD (Environmental Product Declaration), in particular, assess the environmental impacts of a product, and it is used to assess the impact of recycling. At the same time, the typical Carbon Footprint value of 100% recycled aluminium ingot alloys is a value within a range of 1.45 to 2.18 kg CO_2 eq/kg Al. Declaration of the life-cycle environmental impact of products and services for ingot producers is annually reported in the International EPD® System [29].

The European Union's Circular Economy Action Plan, at present, aims to increase the recycling rates of crucial materials, including aluminium, by setting ambitious targets and providing incentives for recycling activities. In this perspective, some authors and companies started suggesting the production of cast not subjected to mechanical solicitation by directly using sorted scraps, avoiding the refining process of the alloy previously summarised [12]. From this perspective, the aluminium recycling market may experience strong growth. From dross to deburring, from scraps to turning waste, all products, from process waste to end-of-life parts, can be valorised with appropriate recycling techniques. The dross produced in the foundry facilities is an industial waste and is recycled for instance

by pyrometallurgy processes, to recovery allumina [30]. The deburring and off-cuts, on the other hand, can be re-melt as the rejected part, after thoroughly cleaning them of cutting fluids.

Conversely, additive manufacturing as a way to recycle scraps is already diffused to recycle plastics [31]. Since 2020, the idea of a circular economy of metals has started to be linked to the idea of additive manufacturing. Although recycling metal scrap into AM-grade powder is challenging, the environmental, economic and performance benefits are undeniable. An example could be the MolyWorks Materials Corporation, which opened in Singapore the first patented compact recycling foundry that upcycles waste metals as feedstock for atomised AM-grade powders [32]. F3nice is an example of an Italian company that provides metal powder made from recycled scrap for additive manufacturing [33].

1.4 Aim of the work

The previous paragraphs outlined the current trend in the use and recycling of Al alloys. It is clear that, on the one hand, there is a push for the use of recycled alloys due to the importance of environmental protection, while at the same time, markets are looking for high-performance alloys.

Considering both the sustainability and the microstructural and mechanical properties, this research aims to focus on recycling Al-Si alloys to produce high-performance components.

In this particular context, the potentiality of gravity casting and additive manufacturing as ways to recycle defective automotive parts that originated during the industrial processes represents the main focus of the research work.

In order to perform the recycling, the alloys must be evaluated from different points of view to understand their processability.

Table 3 summarizes the recycling routes performed in the present work, starting mainly from scrap components in alloy AlSi7Cu0.5Mg and AlSi9Cu3(Fe). Then, even the ingot compositions were considered as a benchmark.

From the AM point of view, mechanical results were compared with results obtained with AlSi10Mg through state-of-the-art results and specifically printed specimens.

Table 3. Recycling routes followed in the research

Recycling route	**Procedures**	
Gravity Casting	Re-melting tests	Microstructural properties
	Casting of mechanical specimens	Mechanical tests
Additive Manufacturing	Atomization from foundry feedstock (ingots and rejected cast)	Powder characterization
		L-PBF
		Mechanical tests

Chapter 2

2 AlSi9Cu3(Fe) and AlSi7Cu0.5Mg cast alloys properties

This chapter explores the main casting processes involved in the automotive sector to cast Al-Si powertrain components, while even the alloy properties were presented. Moreover, the microstructural defects related to the casting process were detailed.

Subsequently, the main strengthening intermetallic phases are shown with a focus on the typical intermetallic phases of the alloys covered by this thesis work.

In the final part of the chapter, the literature properties of the alloy object of the present work are shown and discussed.

2.1 Introduction

Traditionally, several casting methods have been employed for aluminium alloys, each tailored to specific production requirements, such as high or low production rate, alloy types and desired outcomes.

This chapter aims to describe the main casting methods used in foundries and focus on the main alloy subject of this study.

Some traditional casting methods include sand casting, permanent mould casting, high-pressure die casting and others [2]. Sand casting is one of the oldest and most widely used casting processes for aluminium alloys. In this process, a mould made of sand is formed around a pattern, and molten aluminium is poured into the cavity created by the pattern. Once cooled, the sand mould is broken away, leaving behind the aluminium casting [3].

Permanent Mould Casting, also known as Gravity die Casting (GC) or permanent mould casting, involves reusable metal mould typically made of steel or cast iron. Molten aluminium is poured into the mould cavity, where it solidifies to form the desired shape. This method offers higher dimensional accuracy, improved surface finishing, and higher mechanical properties than sand casting.

Die casting is a high-pressure casting process (HPDC) where molten aluminium is injected into steel dies under high pressure. The dies are designed to produce complex shapes with tight tolerances and excellent surface finish. Die casting is commonly used for high-volume production of automotive components.

Another casting process in investment casting, also known as lost wax casting, is a process where a wax pattern is coated with a ceramic shell and then melted out to leave a cavity for molten metal. Aluminium alloys may be used in investment casting to produce intricate, high-quality parts with excellent surface finish.

These traditional casting methods offer various advantages and limitations, depending on production volume, part complexity, dimensional accuracy, and surface finishing requirements. As automotive manufacturers strive for light-weighting, efficiency, and cost-effectiveness, advancements in casting technologies continue to evolve, complementing these traditional methods with innovative approaches like squeeze casting, semi-solid casting, and more.

Particularly, Gravity Casting GC and High-Pressure Die Casting HPDC are the most common processes because they permit obtaining both medium or high production volume and good mechanical properties, along with a strong knowledge of the production technology that, at the present day, has led to the minimization of the production defects.

Gravity casting is a standard method for casting aluminium alloys. In this process, a reusable metal mould, typically made of H11 or H13 steel [34], is used to create the desired shape of the final part or component. The permanent mould is prepared by lubricating its surfaces to facilitate easy release of the solidified aluminium casting and/or painted with release coatings. Then, the mould is preheated to improve the flow characteristics of the molten metal and reduce the risk of defects such as corrosion and soldering by the alloy on the mould surfaces [35]. Subsequently, the aluminium alloy is melted in a furnace up to the required temperature, and the alloy composition and temperature are checked to ensure proper fluidity and solidification characteristics.

Once the molten metal reaches the correct temperature, it is poured into the mould cavity. Gravity aids in filling the mould as the molten metal flows downward under its weight, filling the entire cavity to produce the desired shape. After pouring, the molten metal cools and solidifies inside the mould. The solidification process is carefully controlled to minimize defects and achieve the desired mechanical properties of the final casting.

Once the casting has sufficiently cooled and solidified, the mould is opened, and the casting is removed. Depending on the design of the mould and part geometry, ejector pins or other mechanisms may be used to facilitate the removal of the casting from the mould. After ejection, the casting may undergo additional finishing operations such as trimming excess material, machining, surface treatment, and inspection to ensure it meets the required specifications and quality standards.

Gravity casting offers several advantages, including good dimensional accuracy and surface finish, high production efficiency, the ability to produce complex shapes with relatively simple tooling, and cost-effectiveness compared to processes like sand casting. However, gravity casting may have limitations in producing extremely intricate or thin-walled parts compared to other methods like high-pressure die casting. Additionally, it may not be as suitable for very high-volume production as die casting due to longer cycle times.

High-pressure die casting (HPDC) is a casting process commonly used to produce aluminium alloy components with high precision and efficiency. In HPDC, molten aluminium is injected into a metal die cavity at high pressure to produce complex shapes with tight tolerances [36]. Two halves of a metal die, typically made of steel, are clamped together to form a cavity precisely machined to the shape of the desired part that may have intricate geometries. Then, the die is lubricated to facilitate the cast release and then closed, and molten aluminium is injected into the die cavity at high pressure (70 to 200 MPa).

The high pressure ensures that the molten metal fills the die cavity and solidifies rapidly to produce the desired shape. Once the die cavity is filled, the molten aluminium cools and solidifies under pressure. The cooling rate is controlled to achieve the desired mechanical properties and minimize defects such as porosities or shrinkage. After the casting has solidified, the die is opened, and the casting is ejected using ejector pins or other mechanisms. The casting may undergo additional cooling or quenching to enhance its mechanical properties further.

High-pressure die casting offers several advantages, including high production efficiency, with cycle times typically ranging from seconds to minutes; excellent dimensional accuracy and surface finishing; and the ability to produce complex shapes with thin walls and intricate details [37]. Moreover, even the unit cost is lower because the produced parts are of very high quality and near-net-shape, reducing the necessity of further machining operations [38]. High-pressure die casting is well-suited for high-volume production of small to medium-sized components in automotive, aerospace, electronics, and other industries.

2.2 Defects in Al-Si casting alloys

As Al-Si alloys limit regards, casting defects in these alloys can significantly affect the quality and performance of the final product. As defects regard, they may be due to different causes: gas porosities, micro-porosities, shrinkage and micro-shrinkage [39] and oxide layer entrainment (bifilm) [40]. Concerning solidification, the occurrence of porosity defects due to air entrapment and solidification shrinkage is unavoidable, and this impacts the variability in mechanical properties. On the other hand, porosities due to air entrapment result in very small sizes. Moreover, it is a well common practice to make an impregnation of casts to close small open porosities. A low-viscosity liquid sealant is designed to seal porosity using a

vacuum impregnation process that removes air from the pores and fills them with the liquid sealant, particularly methacrylate monomers [41].

Particular attention must be paid to the possible oxide inclusions due to the dross formation during the alloy maintenance in the holding furnace. Moreover, improper handling of the melt may be conducted to dross entrainment into the casting; in **Figure 2**, XRD analyses of a portion of dross coming from the holding furnace were shown.

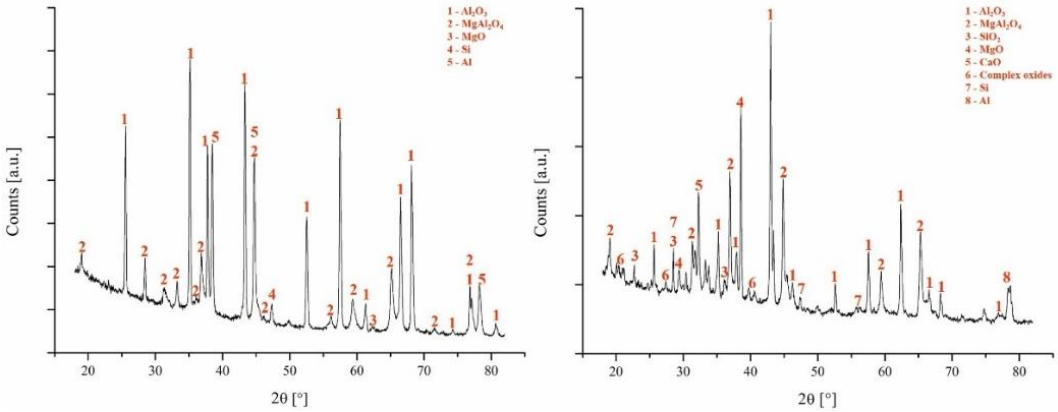

Figure 2. XRD analyses of dross collected from the holding furnace.

Proper mould design, controlled cooling rates, and the use of appropriate alloys and techniques are essential to minimize these defects and ensure high-quality aluminium castings. Other defects are related to the interaction between molten metal and die, such as the metal/die interaction. **Table 4** summarizes the main defects that could be found in Aluminium alloy casting.

Other defects less common are the hot tears, which occur when the alloy contracts and cracks during cooling due to thermal stresses and the cold shuts, which arise when two streams of molten metal fail to fuse properly, creating weak seams.

Table 4. Defects in cast Aluminium-Silicon alloys.

Microstructural defects in casting parts	
Gas/Air porosity [42] Gas porosities have a rounded or oval shape and are typically caused by the hydrogen release from the molten alloy or hydrogen entrapped into the die because of turbulence or mould/ die release agent during the casting. In the figure are noticeable three gas porosities (black).	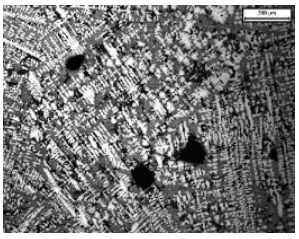
Shrinkage porosity [43] Shrinkage porosities are mainly due to contraction during the solidification not adequately balanced by the molten metal. In the figure is noticeable an extended shrinkage porosity.	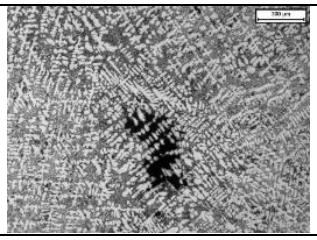
Oxide inclusions [44] Refractory particles can accidentally be introduced into castings, for instance, from the holding furnace, tools, or crucible. Even Mg and Al oxides may form, thanks to their high oxygen affinity. Such oxides can be entrapped during the pouring of the alloys because of turbulence processes. In the figure is noticeable a fine oxide skin inside the eutectic phase (grey).	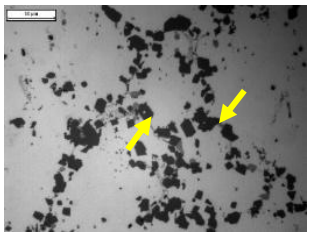
Filling-related defects [45] Filling it is a defect detectable through visual inspection. Particularly, some material is missing in some parts of the cast, caused by an incomplete filling of the die figure.	
Solidification Cracks [45] Hot tears in aluminium castings are a result of tensile stresses that develop during the solidification and cooling of the metal. These stresses can cause cracks if they exceed the material's strength at high temperatures.	
Metal/Die interaction [46] Soldering, erosion, thermal cracking and adhesion are the metal/die interactions that could take place during casting. Such defects arise from the complex interplay between the molten metal and the die material. Preventive measures to avoid or mitigate them are selecting (1) appropriate die materials, (2) applying protective coatings, (3) ensuring proper lubrication, and (4) optimizing die design.	

2.3 Intermetallic phases in cast Al-Si alloys

Microstructures of Al-Si alloys contain different intermetallic phases as a function of the alloying elements.

Intermetallic phases can be into the α-Al phase or the eutectic phase as a function of the alloy composition.

2.3.1 Iron Chinese script

The α-Fe intermetallic phases can be noticed in a large amount of Al-Si alloys because of a relevant amount of iron and manganese. Mainly, α-Fe has a polyhedral form if it solidifies as the primary phase before the eutectic.

In **Figure 3**, different α-Fe are shown.

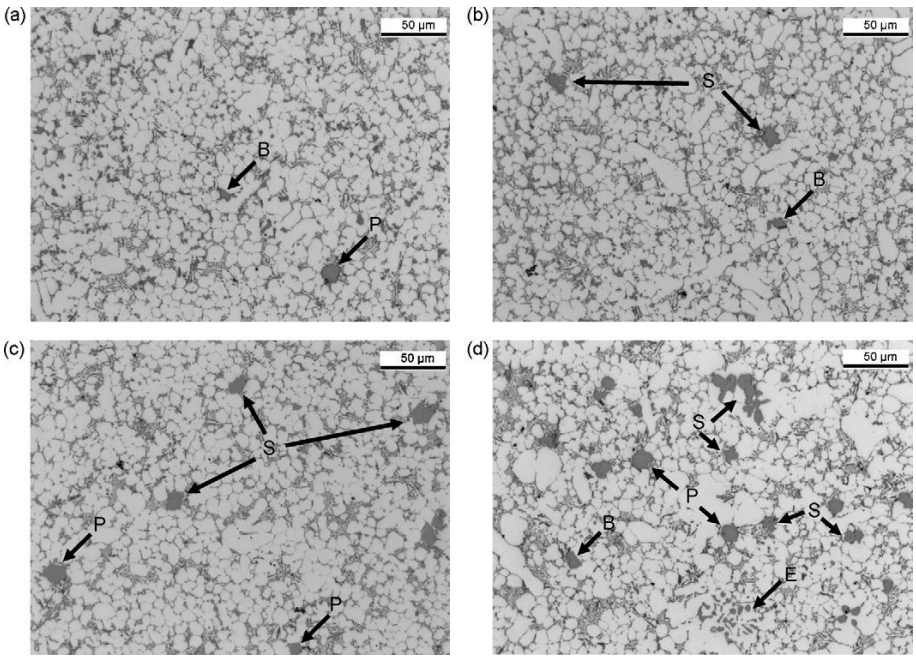

Figure 3. α-Fe shapes in T1- AlSi9Cu3(Fe) alloys having different amounts of Cr. B, Blocky; E, Exploded; P, Polyhedral; and S, Star-like. Image reproduced with permission of the publisher [10]

Different shapes involve different amounts of Fe and Cr. The Chinese script involves a low amount of Cr and a certain amount of Cu. The α-Fe is usually in Chinese script form and could be $Al_{15}Fe_3Si_2$, $Al_{15}(Fe, Mn)_3Si_2$ if Mn is present in the alloy or $Al_{15}(Fe, Mn, Cr)_3Si_2$ if Mn and Cr are added. In addition, when Mn or Cr are present, a large polyhedral shape can be noticed instead of the Chinese script [47]. Chromium can lead to the nucleation of star-like intermetallic phases Al_{13} (Fe, $Cr)_4Si_4$ or Al_2 (Fe, $Cr)_5Si_8$.

Notably, even a small amount of Cu can be noticed; the intermetallic composition can be summarized as follows [48]:

$\boldsymbol{Al_x(Fe,Mn,Cr,Cu)_ySi_z}$ Where x= 11.7 – 16.5; y= 2.3 – 3.3 and z= 2.

Sometimes, Mn can be partially substituted by Fe, while Cu can be partially substituted by Al as in $(Al, Cu)_{15}(Fe, Mn, Cr)_3Si_2$. Chinese script could be AlFeSi, with an amount of Fe of about 30 wt%.

2.3.2 β-Fe and δ-Fe phases

The needle-like iron-rich intermetallic phase β-Fe, namely β-Al_5FeSi phase, promotes the formation of shrinkage pores. Furthermore, since this phase has an acicular shape, it acts as a stress concentration site during uniaxial tensile testing, strongly reducing the mechanical strength. **Figure 4** shows the β-Fe phase [49].

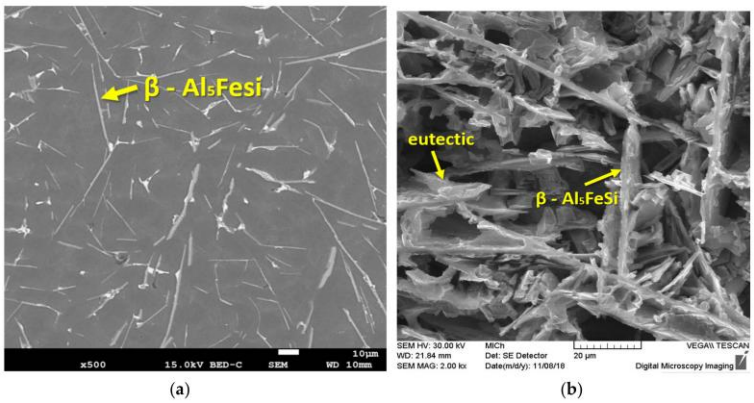

Figure 4. β-Fe observed in AlSi9Cu3 alloy. Image reproduced with permission of the publisher [50]

In Sr-modified alloys, the plate-like intermetallic AlFeSi phase is identified as δ-Al_3FeSi_2, characterized by a Fe-Si ratio of 1:2 [51].

2.3.3 π-Fe phases

The π-Fe phase (**Figure 5**) is characterized by a Chinese-script shape, while the intermetallic composition is π-$Al_8FeMg_3Si_6$. If the iron amount is minor than Mg amount, the π-Fe phase compositions could be $Al_{10}FeMg_4Si_4$ or $Al_5FeMg_8Si_6$. Other Fe intermetallic phases can nucleate by adding Ni, such as Al_9FeNi, or by adding Cu, obtaining Al_7FeCu_2; these phases typically have acicular or plate-like shapes.

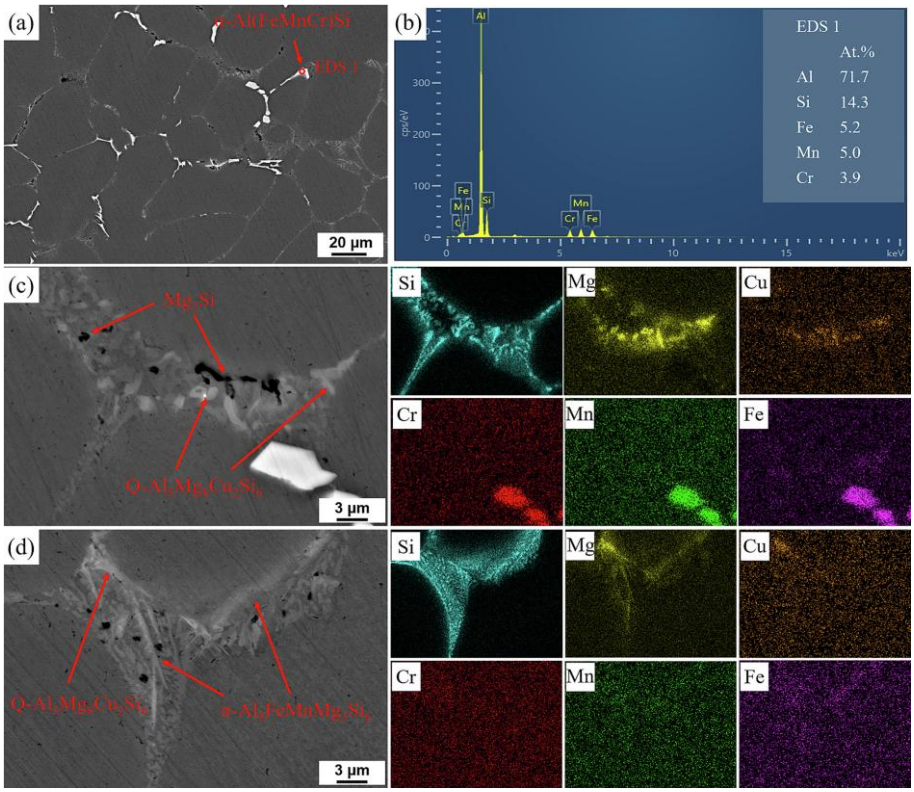

Figure 5. π-Fe, Q-phase and Mg_2Si phase observed in AlSiMgCu alloy. Image reproduced with permission of the publisher [52]

2.3.4 θ-Al_2Cu and Q-phase

The θ-Al_2Cu phase is shown in **Figure 6**. Notably, in this phase, even Ni can be present if it is added to the alloy.

Nickel addition can be considered beneficial or detrimental depending on the alloy's composition and the solidification behaviour. In [53], the authors highlight that Ni negatively affects strength in both as-cast and T6 heat treatment in A356 alloy (AlSi7Mg). Conversely, Ni increases the mechanical strength and wear resistance in other alloy compositions after heat treatment T6 [54].

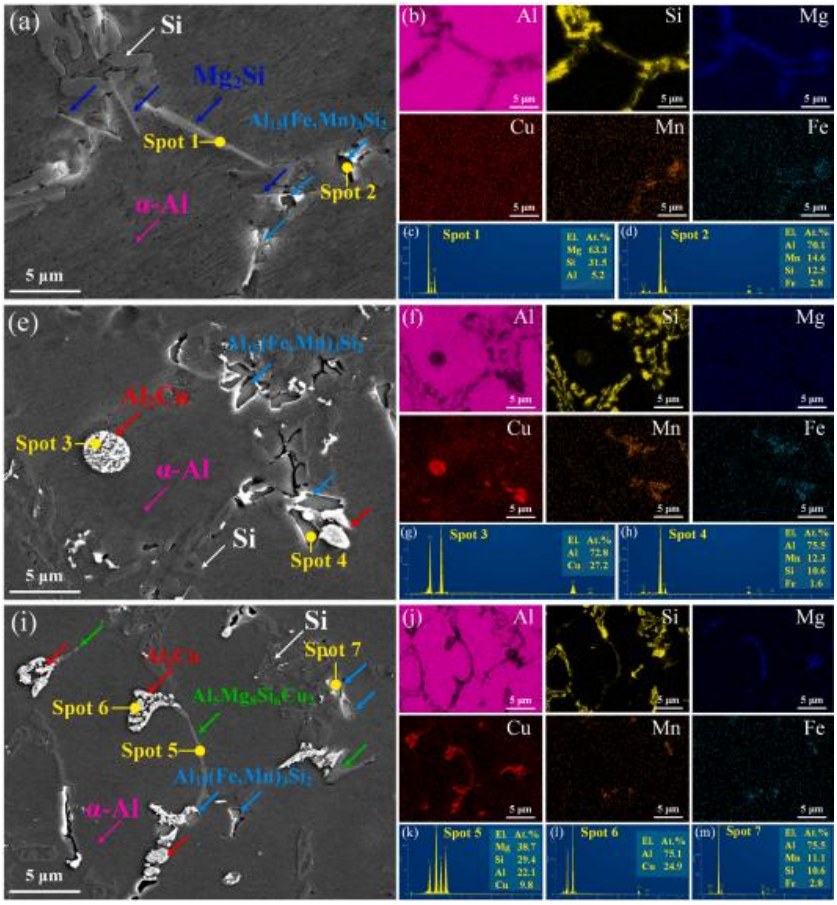

Figure 6. Intermetallic phases θ-Al_2Cu, Q, Mg_2Si and α-Fe in alloy AlSiCuMg alloys. Image reproduced with permission of the publisher [55].

Q-phase composition varies in several stoichiometries: $Al_3Mg_9Si_7Cu_2$, $Al_4Mg_8Si_7Cu_2$ and $Al_5Mg_8Si_6Cu_2$ are reported in the literature [56].

Al_2Cu and Q-phase act as barriers against dislocation movements, increasing the strength of the alloy up to 300 °C. At high temperatures, such phases dissolve into the α-Al matrix [57,58].

2.4 Effect of Fe on the castability of Al-Si alloys

Central to the recycling development by cast route is evaluating the castability by gravity casting. The final product is evaluated by analyzing the re-melt samples' microstructures and porosities.

Castability, as aforementioned, depends on the alloy composition. Furthermore, scraps were previously cast by industrial cast methods and may present particular characteristics intrinsic to the process: Gravity-cast components are mainly affected by oxide skins, while micro-porosities can characterize HPDC parts.

Moreover, iron represents the main undesirable alloying element in secondary Al-Si alloys. Notably, the detrimental effect caused by the increase in Fe content inside the secondary and scraps alloys is well known. Iron promotes the formation of coarse intermetallic phases, as the needle-like or platelet β-Al_5FeSi, which has a shape that promotes cracks during mechanical services. In addition, this intermetallic seems responsible for the degradation of castability and, last but not least, the increase in porosity content [59].

The effect of the iron contents on the increase of porosities into the bulk alloy was even studied in [60]: authors arguing that amounts up to 0.4 wt% of iron into Al-Si-Cu alloys affect the porosities content: pores change from discrete and isolate to interdendritic pores. In addition, a poor cooling rate, as in the gravity casting process, leads to obtaining large spongy regions.

Depending on the alloy composition, various Fe intermetallic phases can be present. Such phases have been largely studied. Mainly, in addition to β-Fe, can be noticed α-Fe, whose chemical composition varies according to the alloying elements present in the alloy, and π-Fe.

Further alloy characterizations depend on the alloy composition. Notably, the Sludge Factor (1), the critical iron content (2) and critical temperature (3) are used to assess the melt quality in order to highlight the alloy's tendency to form sludge and large Fe-based harmful intermetallics [61], which affect castability.

$$\text{Sludge Factor (SF)} = (1\times wt\%Fe)+(2\times wt\%Mn)+(3\times wt\%Cr) \quad (1)$$

$$Fe_{cr} = 0.075 \times (wt\%\ Si) - 0.05 \quad (2)$$

$$Temperature\ (°C) = 645.7 + 34.2 \times (wt\%\ Fe)^2 \quad (3)$$

Mn and Cr, together with Si and Fe, can cause the nucleation of large polygonal phases called sludge, $Al_x(Fe,Mn,Cr)_ySi_z$. Such phases tend to nucleate at the bottom of the casted part, causing an inhomogeneous microstructure and a depletion of such chemical elements in the alloy. Furthermore, sludge nucleates prior to the dendrite formation, negatively affecting the fluidity of the alloy [62]. The (1) formula is generally recognised as correct for a large variety of Al-Si alloys despite other authors suggesting different multipliers [63]. A common procedure is maintaining the sludge factor lower than 1.8 [64].

The critical iron content (Fe_{cr} formula, (2)) is related to the fact that both the size and number of iron-containing phases, especially β-Fe, increase with the Fe content increase. As the Si amount in the alloy increases, the Fe amount that can be tolerated prior to the nucleation of the β-Fe increases, too. However, β-Fe nucleation is prior to the Al-Si eutectic, worsening the flowability and increasing the porosity amount [59]. Notably, in [65] Taylor shows that limits are as follows: at 7 wt% of silicon, the Fe_{cr} rises to 0.5 wt%, while at 9 wt% of Si, the Fe_{cr} is almost 0.6 wt%.

Moreover, the Fe amounts affect both the critical temperature at which the β-Fe starts nucleate (3) and the time required for the nucleation. When the Fe amount increases, the temperatures and time required for the β-Fe nucleation decrease: long dwell times of the molten alloy in the holding furnace can lead to very large and deleterious intermetallics.

2.4.1 Why remelting? Literature results

The recycling process through remelting is a very important aspect of the lifetime of aluminium. Mainly, the metallurgy of recycled aluminium alloys permits both material and energy savings.

As aluminium is the major recycled material used to produce lightweight vehicles, recycling is taking very high attention. Notably, this 'push' comes from both cast and wrought alloy users. The recycling of end-of-life vehicle components is required nowadays in wrought industries [66] and casting industries [67].

From this point of view, the quality of the alloy is a key parameter that must be taken into account. Good mechanical and microstructural properties depend, in turn, on the alloy composition. Notably, with the increase in scrap Al alloys, even the iron content has increased, as previously discussed.

In [50] authors studied the effect of multiple remelting of the alloy AlSi9Cu3(Fe) with the increased amount of Fe. The remelted alloy was not modified nor refined, and before casting, only the oxide films were mechanically removed. Such investigation highlights that the process becomes critical after the fourth remelt, given the important degradation in the microstructure as eutectic silicon and Fe intermetallic enlargements, decreasing the alloy's ductility.

Another research focused on the impact of primary and secondary AlSi9Cu3 alloy ratio in a batch, highlighting that overall mechanical properties decrease with the increase of scrap amount in the as-cast condition. Conversely, after heat treatment, mechanical properties appear to increase [68].

On the other hand, there is evidence of mechanical properties enhancement with remelting in alloys rich in Si and a minor amount of other alloying elements [69].

In [70], authors studied the mechanical properties and microstructural behaviour of alloy AlSi5Cu3 after multiple remelting. They highlight a grain size enlargement with multiple remelting because of a higher amount of porosity; furthermore, mechanical properties slightly decrease with multiple melting. Particularly, the authors measured the grain numbers by ASTM E 112 standard and noticed that in the same area size of 1.26 mm^2, the number of grains was 3973 in as-cast and 3921 after the third remelt.

Additionally, authors in [71] highlight that even an overheating of the melt at high temperatures can cause the generation of oxides and increase grain size in casted parts. Also, not only does the overheating affect the grain size. **Figure 7** shows the cooling rate for the alloy AlSi9Cu3 through different production processes. Such experimental results evidenced a large SDAS up to 55 µm in GDC specimens and lower SDAS if small specimens are produced by HPDC. Cooling rates resulted in very low GDC values of less than 10 K/s. On the other hand, according to the authors, the gravity cast performed in open atmospheric conditions may have affected the porosity amount.

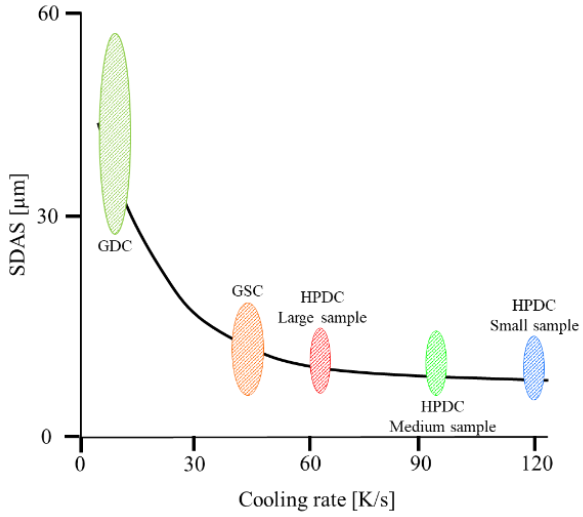

Figure 7. Cooling rate vs Secondary Dendrite Arm Spacing (SDAS) with different casting processes for AlSi9Cu3 alloy. GDC, Gravity Die Casting; GSC, Gravity Sand Casting; HPDC, High-Pressure Die Casting; S, M, and L refer to different HPDC sample sizes. Image adapted from [72].

Finally, authors in [73] demonstrated that it is possible to obtain high-quality cast using scrap alloy by suppressing the β-Fe phase nucleation, thanks to adding some chemical elements. In particular, the authors referred to Hume-Rothery's criteria for stabilizing the Al_8Fe_2Si phase with V, Mo or Cr addition. Such stabilization prevents the transformation of Al_8Fe_2Si in β-Fe.

2.4.2 AlSi7Cu0.5Mg for casting purposes: state-of-the-art

The alloy AlSi7MgCu0.5, even known as EN AC 45500, is a versatile alloy known for its excellent balance of mechanical properties and castability. This alloy is widely utilized in automotive due to its mechanical strength, good corrosion resistance, and excellent castability [74].

The compositional range of such alloys is reported in the table below (**Table 5**). In particular, the composition can change slightly as a function of the alloy type: the amount of the alloying elements could change slightly if the alloy is in ingot form (EN AB) or cast form (EN AC).

Table 5. AlSi7Cu0.5Mg composition limits - standard BS EN 1706:202 + A1:2021

AlSi7MgCu0.5 composition limits								
	Si	*Fe*	*Cu*	*Mn*	*Mg*	*Zn*	*Ti*	*Al*
wt%	6.5-7.5	<0.25	0.2-0.7	<0.15	0.2-0.45 0.25-0.45[1]	<0.07	<0.2	Bal.

[1] Ingot compositions EN AB

The composition of AlSi7Cu0.5Mg is carefully balanced to achieve its desirable properties. The primary elements in this alloy are:

- Silicon (Si): Approximately 7% by weight. Silicon improves the alloy's fluidity during casting and contributes to its strength and hardness.
- Magnesium (Mg): Around 0.2-0.45% by weight. Magnesium enhances the alloy's strength and hardness through precipitation hardening.
- Copper (Cu): About 0.5% by weight. Copper increases strength and hardness, particularly at elevated temperatures, and improves machinability.
- Iron (Fe), Manganese (Mn), Zinc (Zn): Present in trace amounts to enhance specific properties such as strength, corrosion resistance, and castability. Fe is always present in recycled Al-alloys, while Mn is added to avoid the nucleation of harmful Fe-acicular compounds.

The aluminium matrix forms a natural oxide layer when exposed to air. This thin, protective oxide layer acts as a barrier, preventing further oxidation and corrosion. This intrinsic property of aluminium alloys provides a significant advantage in maintaining structural integrity over time.

On the other hand, elements like Si and Cu can influence the alloy's susceptibility to pitting corrosion. Despite that, in this specific composition, the Cu amount is low, and it can only slightly reduce the corrosion resistance compared to pure aluminium. For this reason, the overall resistance remains good.

Even intergranular corrosion could occur; this phenomenon can be mitigated by controlling the heat treatment process and ensuring a uniform distribution of alloying elements. Proper heat treatment, such as T6 temper, can significantly reduce the risk of intergranular corrosion by precipitating alloying elements uniformly within the matrix.

The standard EN 1706 [3] indicates, for T6 heat treatment conditions, the mechanical properties as a function of the casting procedure, along with other casting characteristics. Such properties are only provided in heat-treated T6 conditions (**Table 6**).

Table 6. Properties of Alloy AlSi7Cu0.5Mg - standard BS EN 1706:202 + A1:2021.

Properties of Alloy AlSi7Cu0.5Mg			
Sand casting (T6) Rm 250 MPa min $R_{p0,2}$ 190 MPa min A% 1% HBW 85		*Gravity casting /* *Low Pressure Die Casting (T6)* Rm 320 MPa min. $R_{p0,2}$ 240 MPa min A% 4% HBW 100	
Fluidity	*Machinability*	*Corrosion resistance*	*Weldability*
Good	Good	Good/Fair	Good

Gravity casting is the most common method for producing components from AlSi7Cu0.5Mg. In fact, AlSi7Cu0.5Mg is particularly well-suited for gravity casting due to its good fluidity and favourable mechanical properties in such casting conditions. The alloy is melted in a furnace at temperatures around 650-700 °C since its melting range between solidus and liquidus is 550-625°C.

Up to today, research on the AlSi7Cu0.5Mg aluminium alloy has focused on its mechanical properties, microstructure and optimization of heat treatments.

Studies have shown that heat treatment and equal channel angular pressing (ECAP) significantly improve the mechanical properties and homogenize the microstructure of AlSi7Cu0.5Mg.

Heat treatment commonly involves solution annealing at temperatures higher than 500 °C, followed by water quenching and artificial ageing, usually up to 200°C. Such treatment results in partial spheroidization and coarsening of eutectic Si-particles. This process enhances the distribution of precipitated phases, such as β(Mg_2Si) and Q-$Al_4Mg_8Si_7Cu_2$, contributing to improved mechanical strength and ductility [75,76].

In [77], the authors studied the influence of heat treatment on the intermetallic precipitation sequence. They highlight that the solidified microstructure of AlSi7Cu0.5Mg consists of intermetallic phases iron-based π-$Al_8Mg_3FeSi_6$ and α-Al(Fe, Mn)Si, eutectic Si and Q $Al_5Cu_2Mg_8Si_6$. The T6 heat treatment consists of two steps: the first one involves solubilization, which affects the Si shape by spheroidizing it and dissolving the Q metastable phase, while the artificial ageing mainly affects the formation of the β-Mg_2Si. Optimizing the T6 heat treatment for gravity-cast AlSi7Cu0.5Mg has shown significant improvements in mechanical properties, particularly for applications such as V8 cylinder heads.

In [78] authors highlighted that by performing a T6 heat treatment with solution at 545°C for 1 hour followed by ageing at 180°C for 3 hours, achieved markedly superior mechanical properties: R_m 344 MPa, $R_{p0,2}$ 281 MPa, A% of 5% and HB hardness of 106. Following the authors' suggestions, this optimized process not only enhanced the mechanical properties but also reduced the total heat treatment duration by 2.5 hours, increasing the production capacity by 61%.

2.4.3 AlSi9Cu3(Fe) for casting purposes: state-of-the-art

AlSi9Cu3(Fe) is a versatile hypoeutectic aluminium alloy widely used in various sectors thanks to its good mechanical properties, castability, and resistance to wear and corrosion. This alloy, also known as EN AB/ AC 46000, is particularly favoured in the automotive and aerospace sectors for components that require high strength. The compositional range of the alloy is reported in **Table 7**. AlSi9Cu3(Fe) alloy composition typically includes the following alloying elements:

- Silicon (Si): Approximately 9% by weight. Silicon improves the castability and fluidity of the alloy.
- Copper (Cu): Around 3% by weight. Copper enhances the strength and hardness of the alloy through precipitation hardening.
- Iron (Fe): Typically, up to 1.3% by weight. Iron helps control the sticking between Al and the die walls but can also cause the nucleation of harmful intermetallic compounds.
- Manganese (Mn): Often included in small amounts to counteract the negative effects of iron.
- Zinc (Zn): Generally, present up to 1.2 wt%. Zinc can improve the mechanical strength of the alloy by contributing to the strengthening of the solid solution. It improves castability.
- Magnesium (Mg): Usually present in trace amounts (~0.1-0.3%) to improve strength and hardness.

Table 7. AlSi9Cu3(Fe) composition limits - standard BS EN 1706:202 + A1:2021

AlSi9Cu3(Fe) composition limits						
	Si	*Fe*	*Cu*	*Mn*	*Mg*	*Cr*
wt%	8-11	1.3 (0.6-1.1)[1]	2-4	< 0.55	0.05-0.55 (0.15-0.55)	< 0.15
	Ni	*Zn*	*Pb*	*Sn*	*Ti*	*Al*
wt%	< 0.55	< 1.2	< 0.29	< 0.15	< 0.25 (0.2)	Bal.

[1] Numbers in brackets are ingot compositions EN AB

The corrosion resistance of AlSi9Cu3(Fe) is generally influenced by its microstructure, the presence of alloying elements, and the casting process. The corrosion resistance of AlSi9Cu3(Fe) has been studied under different environmental conditions. It was found that high-pressure die-cast samples exhibit a primary α-Al phase with dendritic morphology and an Al-Si eutectic structure. These microstructural characteristics, resulting from intense shear and rapid cooling rates, contribute to the alloy's good corrosion resistance.

The alloy's microstructure, which includes the distribution of Si particles and intermetallic phases like Al_2Cu and $Al_{15}(Fe, Mn)_3Si_2$, plays a crucial role in its corrosion behaviour. A fine and uniform microstructure, achieved through processes like high-pressure die casting (HPDC), typically enhances corrosion resistance.

The alloy's performance in various corrosive environments, such as saline atmospheres or acidic conditions, has been studied extensively. It has been found that AlSi9Cu3(Fe) exhibits good resistance to atmospheric corrosion and is suitable for components exposed to mild corrosive conditions typical in automotive applications [11].

Generally speaking, AlSi9Cu3(Fe) is known for its good mechanical properties, including high strength and moderate ductility. The alloy's mechanical properties can be significantly influenced by the casting process and post-treatment methods (see **Table 8**).

Table 8. Properties of Alloy AlSi9Cu3(Fe) - standard BS EN 1706:202 + A1:2021.

Properties of Alloy AlSi9Cu3(Fe)			
High Pressure Die Casting (F) Rm 240 MPa min. $R_{p0,2}$ 140 MPa min A% < 1 HBW 80		*High Pressure Die Casting (T5)* Rm 240 MPa min. $R_{p0,2}$ 165 MPa min A% < 1% HBW 85	
Fluidity	*Machinability*	*Corrosion resistance*	*Weldability*
Good	Good (F)	Poor	Unsuitable

High-pressure die casting (HPDC) is a widely used manufacturing process for producing high-quality aluminium alloy components in AlSi9Cu3(Fe). Moreover, such alloy is normally not recommended for other production processes.

High-pressure die casting (HPDC) of AlSi9Cu3(Fe) involves several critical parameters that need to be carefully controlled. Typically, injection pressure ranges from 100 to 200 MPa. High injection pressure ensures complete mould filling and helps achieve fine details and smooth surfaces, while typical speeds range from 0.5 to 2 m/s, depending on the complexity of the mould and the size of the part. The molten AlSi9Cu3(Fe) alloy is usually maintained at a temperature between 680°C and 730°C to ensure good fluidity and prevent premature solidification into the die.

The die is preheated to a temperature range of 150°C to 250°C; inside the die, proper cooling channels are present to ensure a correct cooling rate: cooling rates

(approximately from 60 °C/s to 125 °C/s) are beneficial for refining the microstructure and improve mechanical properties in the casting [79].

The study [11] investigated the microstructural changes in AlSi9Cu3(Fe) when high-melting-point elements like Cr, Mo, V, and W are added. The addition of transition elements resulted in the formation of complex intermetallic phases, particularly the $Al_{15}(Fe, Mn, X)_3Si_2$ phase (X = metal). This phase's area fraction increased with the content of high-melting-point elements, which enhanced the alloy's strength and thermal stability. The study found significant differences in microstructure between shell moulding and high-pressure die casting (HPDC) techniques, with HPDC providing finer microstructural details. The effects of casting defects on the fatigue behaviour of AlSi9Cu3(Fe) were explored, highlighting the role of microstructural integrity in determining the alloy's mechanical performance.

High-pressure die casting (HPDC) has been particularly effective in minimizing defects and enhancing the fatigue resistance of this alloy. This process leads to a fine dendritic α-Al phase and a well-distributed Al-Si eutectic component, contributing to better mechanical properties and reduced porosity [79]. Research has also shown that the cooling rate significantly impacts the mechanical properties of AlSi9Cu3(Fe). Increasing the cooling rate from 60 °C/s to 125 °C /s improved the strength at 5% deformation from 261 MPa to 335 MPa. This demonstrates that faster cooling rates during casting enhance the alloy's mechanical properties by refining the alloy's microstructure.

2.4.4 Heat treatments and intermetallic phases

Mainly, only a few heat treatment HTs appear useful for Al-Si alloys: T5, T6, T64, T7, and annealing O treatments. The T5 treatment consists of a controlled cooling from casting followed by an artificial ageing or over ageing. However, T6 heat treatment consists of a solution treatment followed by quench and artificial ageing. Similar to T6, the T64 heat treatment consists of a solution treatment plus quench followed by an under-aging treatment. T7 heat treatment is similar to the previous but the artificial ageing is an overageing treatment. Alloy AlSi7Cu0.5Mg (EN AC 45500) is usually treated by T6 [3,77]. It is, on the other hand, important to consider the possibility of blistering if the heat treatment is performed on HPDC specimens due to the high amount of microporosities inside the cast [80].

The fluctuations in alloy composition permitted by international standards can strongly affect the solidification behaviour of the alloy, the intermetallic phases and the fluidity of the alloy. For instance, in AlSi9Cu3(Fe), an amount of Si near the upper limit of 11 wt% guarantees higher fluidity than an amount of 8 wt% (**Table 7**). In fact, a Si amount of 11 wt% makes the alloy very near to the eutectic composition; in this case, the intermetallic compounds will nucleate during the eutectic nucleation and do not affect the fluidity. On the other hand, in AlSi7Cu0.5Mg alloy, the upper limit of Si is 7.5 wt% (**Table 5**): intermetallic phases start nucleated into the interdendritic liquid, causing a worsening in fluidity, especially if Fe or Mn amount increases. This is because Fe tends to form long acicular intermetallic phases or plate-like intermetallic with Mn, which slows down the melt flow.

From the solidification point of view, the Scheil-Gulliver model is expected to be used to calculate the non-equilibrium cooling curves and the nucleation of the intermetallic phases. Recently, Wang et al. studied the intermetallic phases that occur during the solidification and the precipitation sequence during the heating up to 500 °C for the alloy AlSi7Cu0.5Mg [81].

Interestingly, authors for this composition found seven events: four exothermic peaks and endothermic peaks. Particularly, the continuous heating model evidenced various events confirmed by the DSC analysis: three endothermic peaks are always related to dissolution events and four exothermic peaks that regard the precipitation of phases.

After the solidification, in AlSi7Cu0.5Mg microstructure can be noticed: π-$Al_8Mg_3FeSi_6$ phase, α-AlFeMnSi, Q-$Al_5Cu_2Mg_8Si_6$, α-Al and Si_{eu}. The solution treatment refines the eutectic silicon Si_{eu} and dissolves the metastable Q phase. Finally, the precipitation hardening up to 200 °C acts only on β' ($Mg_{1.8}Si$) and β'' (Mg_5Si_6), while at 230 °C the predominant phase is Q and Q', and the alloy's hardness decreases.

The solidification for AlSi9Cu3(Fe) alloy leads to the nucleation of sludge phase α, which depends on the sludge factor that, in turn, depends on the amount of Fe, Mn and Cr present in the alloy, as in (1).

After the sludge phase, the β-Al_5FeSi phase solidification takes place, followed by other complex intermetallic phases, α-Al and Si_{eu}.

At the final stage of the solidification, below 530°C, the nucleation of the Q phase and θ-Al_2Cu phase takes place. Particularly, other complex intermetallic phases containing iron, nickel or chromium can be found, while it seems Zn does not form any intermetallic phase.

Conventionally, AlSi9Cu3(Fe) alloy is an HPDC alloy: the suggested heat treatment is the T5 heat treatment (standard BS EN 1706:2020 + A1:2021) that consists of a controlled cooling after casting, followed by an artificial ageing. In fact, a T6 heat treatment that involves the solution stage at a high temperature (470 – 520°C) is usually avoided because it can cause blistering [82].

In [83], Hurtalová et al. remelt the alloy AlSi9Cu3(Fe) coming from scraps and cast samples by gravity casting in order to study different heat treatments. The research has shown that during heat treatment, a spheroidization of the eutectic silicon occurs, as attended; the optimum temperature for the Si spheroidization seems to be 515 °C. Moreover, at 515 °C as solubilization temperature and natural ageing of 24 hours were noticed the higher tensile properties (273 MPa @515 °C 4 hours) and the higher hardness values (124 HB @ 515 °C 2 hours).

Even the remelting effect on the mechanical properties was studied. Kasińska et al. [50] evaluated the mechanical properties with and without heat treatment in alloy AlSi9Cu3(Fe) as a function of the remelting steps. The research mainly focused on the effect of natural ageing after casting (160 hours at 20 °C) and on the effect of the heat treatment T5, with artificial ageing at 200 °C for 4 hours. Authors found that the tensile properties degradation takes place after the fourth melt (Rm 197 MPa at the third remelt, 174 MPa at the fifth remelt, and 165 MPa at the seventh remelt), while the hardness after artificial ageing is up to 109 HBW at seventh remelt. The hardness increases mainly with the increase of the remelt steps, thanks to the formation of sludge particles.

A list of the possible intermetallic phases is shown in **Table 9**.

Table 9. Intermetallic phases in Cast Al-Si alloys

Alloy	Phases	Ref.
AlSi7Cu0.5Mg GC	α-$Al_{15}(Fe,Mn)_2Si$; α-$Al_{12}(FeMn)_3(SiCuMg)_2$; α-$Al_{15}(FeMn)_3(SiCu)_2$ β-Mg_2Si; β'-$Mg_{1.8}Si$; β''-Mg_5Si_6 Q-$Al_5Cu_2Mg_8Si_6$; Q'- $Al_{3.8}Mg_{8.6}Si_6Cu$ π-$Al_8Mg_3FeSi_6$ Al matrix ; Eutectic Si	[77,84]
AlSi9Cu3(Fe) HPDC	α-$Al_{15}Fe_2Si$; α-$Al_{15}(Fe,Mn)_2Si$; α-$Al_{15}(Fe,Mn,Cr)_2Si$ θ-Al_2Cu; Al-Al_2Cu-Si Al matrix; Eutectic Si Q-$Al_5Cu_2Mg_8Si_6$; Q'- $Al_{3.8}Mg_{8.6}Si_6Cu$ β-Mg_2Si	[85]

2.5 Recyclability Protocol: Gravity Casting

In this work, the direct recycling of scraps was selected to perform laboratory-scale gravity casting. An investigation protocol has been designed and optimized to better characterize the scrap's recyclability by gravity casting, as in **Figure 8**. In particular, such protocol can be divided into three main sub-tasks that aim to assess alloy recyclability.

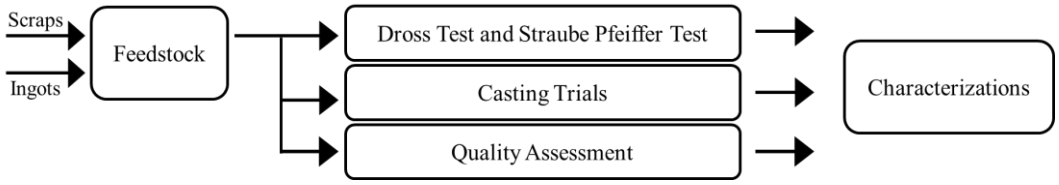

Figure 8. Block-diagram. Investigation protocol

The first sub-task involves performing the Dross and Straube Pfeiffer tests [86]. The dross test allows a fast and economic qualitative evaluation of the amount of non-metallic inclusions in the alloy. At the end of both tests, the duration of which depends on the type of alloy and, in particular, the silicon content, the metal is cut in the middle, and the size and number of pores are evaluated (Straube Pfeiffer test)

and the dross on the alloy surface analysed (Dross test). **Figure 9** depicts the Dross and Straube Pfeiffer tests apparatus and an example of obtained sample.

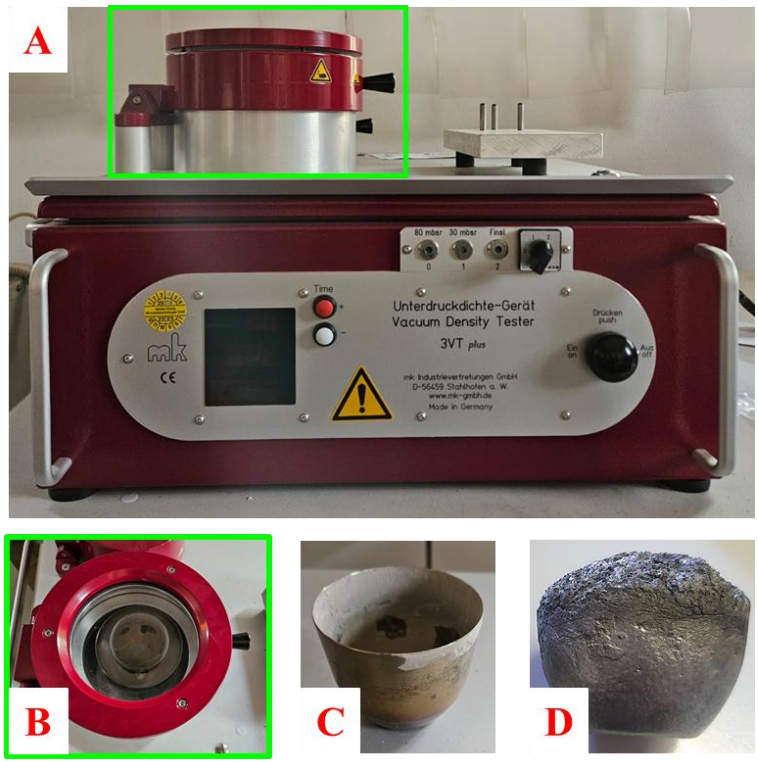

Figure 9. Dross and Straube Pfeiffer tests apparatus. A: Instrument; B: chamber to perform tests; C: crucible for Dross test and Straube Pfeiffer test; D: obtained sample.

The second sub-task consists of the first casting trials by gravity casting. Gravity casting was performed in two steps. The first one involves the melting of the alloy in an electric furnace using a graphite crucible while the second part involves the pouring of the melted alloy into the mould. **Figure 10** shows the manual-casting procedure and an example of obtained samples.

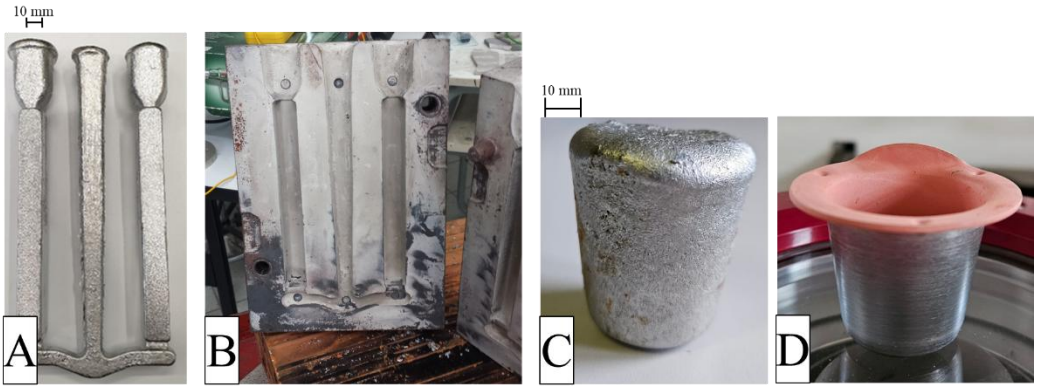

Figure 10. Cast and mould. A: cast for mechanical samples; B: mould to cast mechanical samples; C: cast for microstructure characterizations; D: crucible used to cast samples for microstructural characterizations.

The following Ishikawa diagram [87] was prepared and considered to keep the GC process under control, **Figure 11**.

The third sub-task consists of the alloy quality assessment (feasibility evaluation) through the cast-part examination. The amount of porosity was evaluated with the aim of understanding the castability through visual inspection. In particular, the higher the porosities after casting, the lower the mechanical results will be. From this perspective, small specimens are cast and milled to remove the surface oxide, and then samples are checked for bulk integrity.

The full recycling steps can be summarized as shown in **Figure 12**.

Further evaluations will be made if the feasibility evaluation gives positive results, as shown in **Figure 13**. Particularly, the eventual positive results were evaluated as detailed in the investigation protocol: cast samples obtained through cast variable amount of scrap and ingot alloy must present a low amount of porosities, must show high castability through GC and must present good microstructural features. Specimens for mechanical tests are melted using ingot and scrap alloys in variable amounts as further exposed in 4.1.

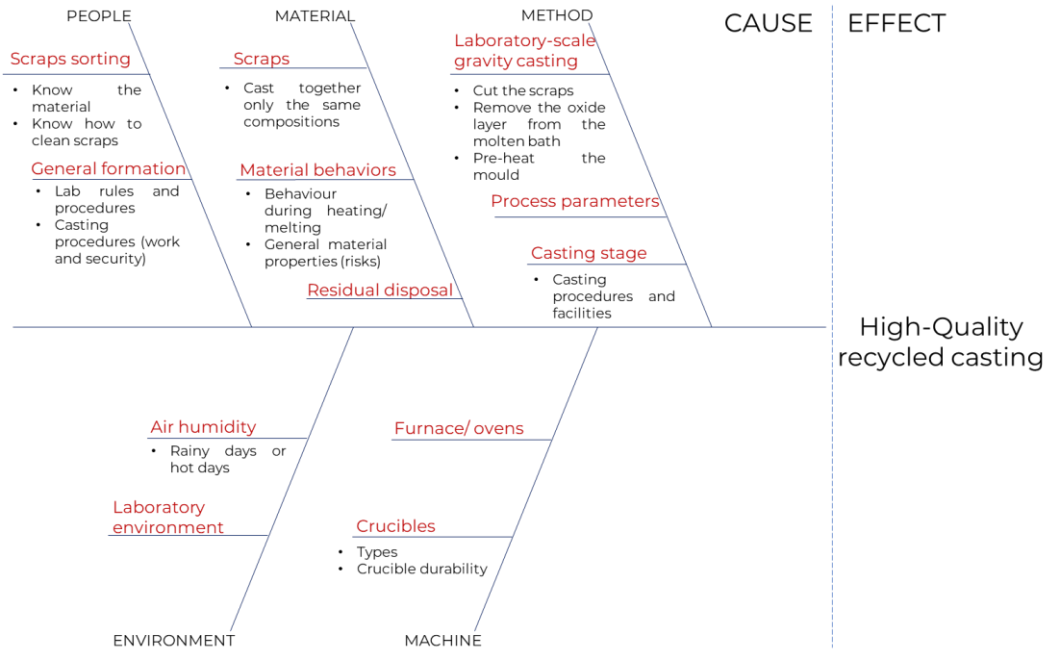

Figure 11. Ishikawa diagram cause-effect considered during the GC.

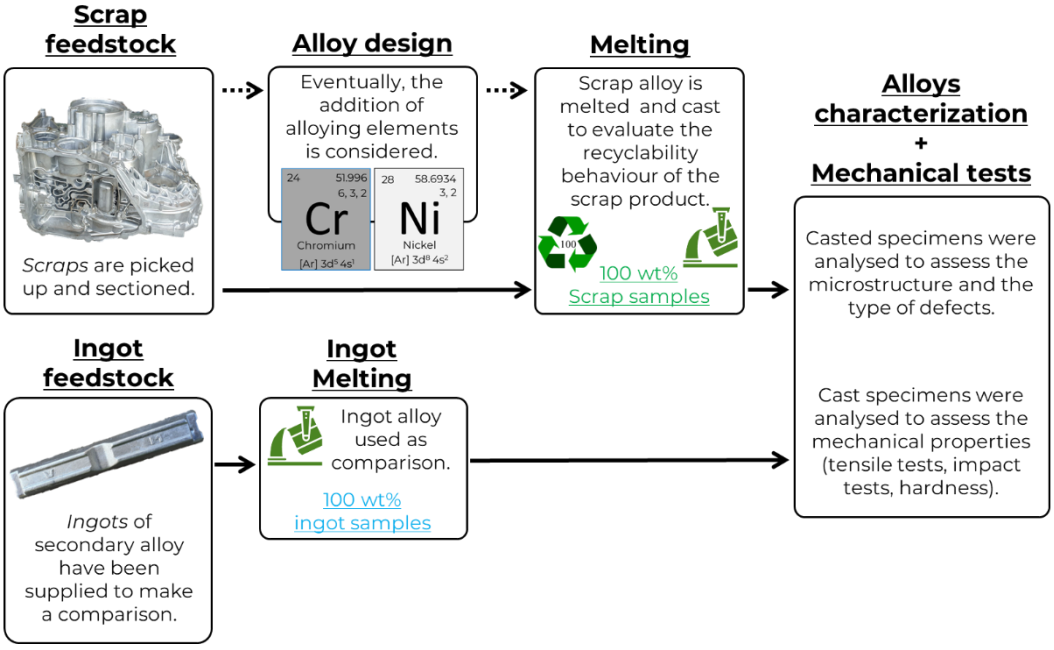

Figure 12. First set-up in recycling alloys by gravity casting.

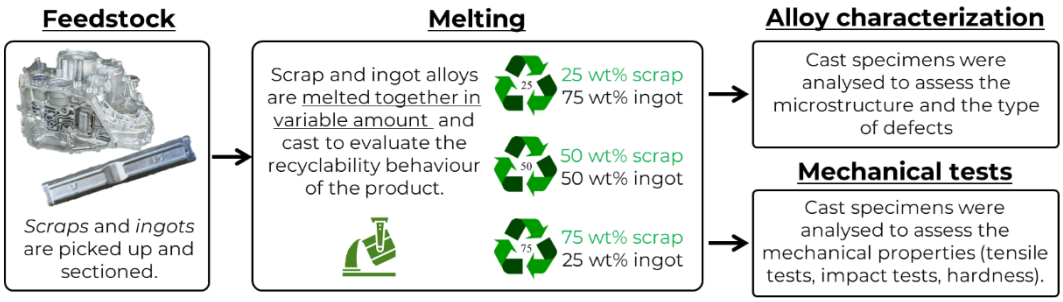

Figure 13. Second set-up in recycling alloys by gravity casting.

Chapter 3

3 Additive manufacturing: AlSi9Cu3(Fe) and AlSi10Mg alloys

This chapter delves into the main steps in Atomization and L-PBF processes. Defects in additive Manufacturing components are exposed along with the main properties of the alloys used in AM.

Subsequently, the main strengthening intermetallic phases are shown focusing on the typical intermetallic phases of the alloys covered by this thesis work.

The final part of the chapter detailed the recyclability protocol through AM.

3.1 Introduction

Currently, additive manufacturing is largely used in aeronautic applications [88] and in automotive, while defects, such as pores and cracks, cause low mechanical properties in as-built components and limit the application of such alloys in the aerospace sector [89].

The forecast for the global high-performance aluminium alloys market, intended as the production of alloys through forging, extrusion and powders, estimates an Additive Manufacturing market growth by 2031. High-performance alloys means alloys engineered to meet specific performances to meet the requirements of aerospace, automotive, defence, marine, and electronics markets [90]. On the other hand, the new release of Formula 1 technical regulations, in particular, will introduce from 2026 significant updates concerning aluminium additive manufacturing. The regulations explain the areas where additive manufacturing can be used and the materials involved [91]. Particularly, the main aluminium alloys involved are AlSi10Mg and AlSi7Mg alloys.

The choice of atomization method depends on the desired properties of the metal powder, such as particle size, shape, purity, and application requirements. For instance, gas atomization is preferred for obtaining high-quality spherical powders, while water atomization is more cost-effective for large-scale production of irregular powders. Gas atomization is a process used in the production of metal powders, including aluminium powders, which is widely used in various industries, including automotive and aerospace, and powders for L-PBF are produced through this method.

Gas atomization involves the conversion of molten metal into small, spherical particles by using high-pressure gas jets. It is a scalable process that can be easily adjusted to produce metal powders in various batch sizes, ranging from small laboratory-scale batches to large industrial-scale production runs. The process begins with the melting of the metal feedstock, typically in an induction furnace or an electric arc furnace. The metal is heated to its melting point, ensuring it is fully liquefied and free of any impurities. The molten metal is then transferred to an atomization chamber, which is typically a tall, cylindrical chamber equipped with a nozzle at the top. The chamber is evacuated or filled with an inert gas atmosphere, such as argon, to prevent oxidation of the molten metal. At the top of the atomization chamber, there is a specially designed nozzle through which the molten metal is forced. The nozzle is equipped with a series of small orifices or jets through

which high-pressure gas, typically inert gas such as nitrogen or argon, is introduced. As the molten metal is forced through the nozzle, it encounters the high-pressure gas jets. These gas jets break up the molten metal stream into small droplets or particles. The gas jets also help to control the size and shape of the resulting metal particles. As the metal droplets are atomized, they rapidly cool and solidify as they fall through the atomization chamber. The inert gas atmosphere helps to prevent oxidation of the metal particles during cooling. The solidified metal particles are collected at the bottom of the atomization chamber.

In **Figure 14**, the scheme of the Gas Atomizer is shown [92]. Depending on the specific application, the metal powder may undergo further processing steps, such as sieving to remove oversized particles or annealing to improve particle morphology and properties.

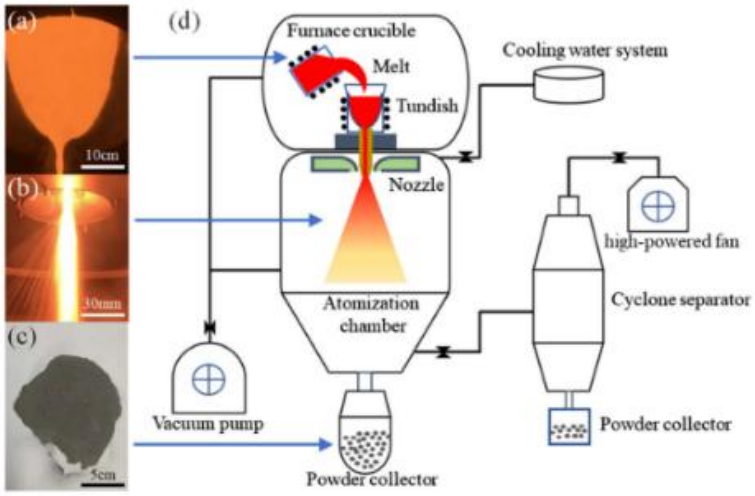

Figure 14. Melting process (a), atomization (b), final powder (c) and scheme of gas atomization apparatus (d). Image reproduced with permission of the publisher [92].

Gas atomization produces metal powders with a relatively uniform particle size distribution, which is crucial for many applications, including additive manufacturing and powder metallurgy. The high-pressure gas jets in gas atomization tend to produce metal particles with a spherical shape, which enhances the flowability, packing density, and sinterability of the powder. Gas atomization

can produce metal powders with high purity and low levels of contamination, as the process is conducted in an inert gas atmosphere that prevents oxidation and contamination of the metal particles. The atomized powders are subsequently processed typically by Powder Bed Fusion, namely a layer-by-layer process that alloys the creation of an object following a 3D design [93].

Overall, gas atomization is used in industries requiring high-purity powders, such as additive manufacturing, metal injection moulding, and high-performance alloy production.

The main pros and cons are:

- Produces high-quality, spherical powders with controlled size distribution;
- Suitable for a wide range of metals and alloys;
- Relatively high cost due to the use of inert gases (argon, nitrogen or helium) and complex equipment.

Laser Powder Bed Fusion (L-PBF) is an advanced additive manufacturing technique used to produce high-precision metal parts. In this process, a high-powered laser selectively melts and fuses metal powder, layer by layer, to build up the desired object. The build chamber is typically filled with an inert gas (argon or nitrogen) to prevent powder oxidation.

L-PBF allows for the creation of complex geometries and detailed features that are difficult or impossible to achieve with traditional manufacturing methods. A blade, also called recoater, spreads the powder on a building platform, and the laser melts the particles following a certain scanning strategy, layer by layer. When a layer is completed, the molten areas are solidified, the building platform is moved down to a certain distance defined by the operator (i.e. the layer thickness), and a new layer is deposited. The pre-deposited layer of metal powder is melted through the laser beam. Many melting and solidification sequences form layers, and the layers form the final 3-D object.

In order to increase the adhesion between the platform and the powder and reduce the residual stresses, the platform can be pre-heated at a temperature dependent on both the machine's capability and the material powders. Additionally, the platform material should be similar to the powder material in terms of chemical

composition and weldability behaviour. This compatibility is crucial to prevent (1) the formation of brittle intermetallic compounds (as sticking between melted powder and base plate, similar to what was discussed in HPDC die/melt interactions) and (2) avoid the opposite issues of insolubility between the two metal, that will lead to the detachment of the part from the substrate during printing.

3.2 Defects in AM components

With the diffusion of additive manufacturing, as emerged technology for manufacturing automotive aluminium components, the L-PBF process parameters must be carefully studied and adjusted to obtain an enhanced alloy's microstructure.

Laser Powder Bed Fusion (L-PBF) defects in aluminium alloys can impact the mechanical properties and overall quality of the final components. Common defects include porosities, cracks and residual stresses. Balling, surface roughness and layer delamination are other issues that can arise from sub-optimal process conditions. Ensuring optimal laser settings, powder quality, and process control are essential to mitigate these defects and achieve reliable, high-performance aluminium parts in L-PBF manufacturing.

Table 10 summarizes the main defects that could be found in aluminium L-PBF.

Table 10. Defects in L-PBF

Microstructural defects in L-PBF printed parts	
Lack-of-fusion porosity [94] Lack-of-fusion porosity in Laser Powder Bed Fusion (L-PBF) is a defect that occurs when the laser fails to fully melt and fuse the metal powder particles. This results in voids or pores within the printed material.	
Keyhole porosity [95] Keyhole porosity in Laser Powder Bed Fusion (L-PBF) is a defect that occurs when the laser energy input is too high, causing excessive melting and vaporization of the metal powder. This leads to the formation of keyhole-shaped voids.	
Balling [94] Balling porosity in Laser Powder Bed Fusion (L-PBF) is a defect that occurs when molten metal forms into spherical balls rather than spreading uniformly to create smooth layers. This can lead to the creation of pores and irregularities in the final part.	
Gas porosity [94] Common defects are characterized by the presence of gas-filled voids or pores within the solidified material. Gas can be entrapped within the powder particles during their production or handling, and molten metal can absorb gases from the surrounding environment, especially if there is contamination or insufficient shielding gas.	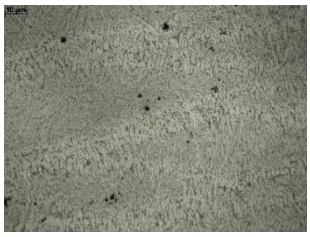
Distortion and residual stresses [94] Distortion and residual stresses are common issues in Laser Powder Bed Fusion (L-PBF). Rapid heating and cooling cycles during the L-PBF process create steep thermal gradients, leading to uneven expansion and contraction. As the material solidifies and cools, it shrinks. If the shrinkage is not uniform, it can cause the part to warp or distort. In the figure, cubes after L-PBF show distortions.	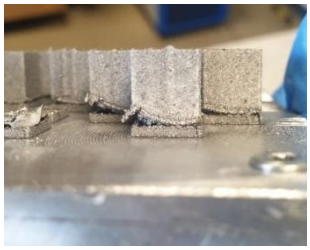

3.3 Strengthening intermetallic phases in AM Al-Si alloys

After L-PBF, the microstructure of Al-Si hypoeutectic alloys is composed of primary Al grains (Super Saturated Solid Solution) and the eutectic Si phase [7]. In fact, the rapid cooling rate during L-PBF leads to a higher supersaturation than the equilibrium-attended supersaturation. This behaviour can permit the direct artificial ageing of the alloys without the solubilization phase. On the other hand, from the literature, it was argued that the direct precipitation strengthening on the as-built specimens could not be optimal because of the higher hardness obtained.

In as-built L-PBF specimens with a certain amount of alloying elements, such as in AlSi9Cu3 alloy, the as-built microstructure consists of overlapping melt pools surrounded by fusion boundaries, while at higher magnification intermetallic phases can be noticed along with Si [96].

The intermetallic phases that act to strengthen Al-Si additively manufactured alloys are the same as those involved in cast alloys. In the as-built L-PBF specimens, can be noticed θ, θ' and θ" [97] (a metastable form of θ) and Mg-based intermetallics such as β-Mg_2Si and Q-$Al_5Cu_2Mg_8Si_6$. On the other hand, the possible depletion of Mg during printing can hinder the nucleation of Mg compounds [98].

3.4 AlSi10Mg: the state-of-the-art in Aluminium AM

In terms of alloys for additive manufacturing, AlSi10Mg represents the most widely diffused aluminium-silicon composition, known for its good combination of mechanical properties and castability. This alloy is particularly favoured in the aerospace, automotive, and additive manufacturing industries due to its lightweight nature and good mechanical properties. Notably, in the foundry sector, the variant AlSi10MnMg, which contains a certain amount of Mn, is most diffused, aiming to form intermetallic phases with iron. The alloy AlSi10Mg includes:

- Silicon (Si): Approximately 9.0-11.0% by weight. Si improves the castability and fluidity and reduces shrinkage during solidification.
- Magnesium (Mg): Up to 0.4 wt%. Mg contributes to the strength and hardness of the alloy through precipitation hardening and improves corrosion resistance.

- Iron (Fe): Typically, up to 0.55% by weight, helps to control the sticking between Al and the die walls but can also cause nucleation of harmful intermetallic compounds.
- Titanium (Ti): Could be present up to 0.15 wt% to refine the grain structure, improving mechanical properties.

In the last years, advancements in processing techniques, particularly in additive manufacturing, have further enhanced the applicability of AlSi10Mg. Innovations in 3D printing have allowed for the production of intricate parts with optimized microstructures, improving overall performance and expanding the potential applications of this versatile alloy [79]. Typical L-PBF printing parameters are shown in **Table 11**.

Table 11. Literature L-PBF printing parameters AlSi10Mg

Parameters	Values	References
Scanning strategy	Chess boards/ stripes 45°/ stripes 67°/ continuous	[99]
	Stripes 67°	[100]
Hatch spacing [µm]	130	[101,102]
Layer thickness [µm]	30	[100,103]
	50	[101,102]
	15/ 20	[99]
Laser power [W]	350	[101]
	95	[99]
	180	[102]
	400	[100]
Laser Spot Size [µm]	100	[100]
Speed [mm s^{-1}]	1650	[101]
	650/ 480	[99]
	600	[102]
Atmosphere	Argon	[101]
Powders diameter [µm]	20-63	[102]
	15-45	[100]
Platform Temperature [°C]	150	[101]
	165	[100]

As regards additive manufacturing powder, the use of this composition is well consolidated. For this reason, the alloy is readily available, while different suppliers showed very slight differences in alloy compositions, as shown in **Table 12**.

Table 12. AlSi10Mg composition designed for additive manufacturing

AM – AlSi10Mg composition limits [104]								
Element	*Si*	*Fe*	*Cu*	*Mn*	*Mg*	*Zn*	*Ti*	*Al*
Min wt%	9-11	<0.55	<0.05	<0.45	0.25-0.45	< 0.1	<0.15	Bal.
PSD [µm]	25-70							
AM – AlSi10Mg composition limits [105]								
Element	*Si*	*Fe*	*Cu*	*Mn*	*Mg*	*Zn*	*Ti*	*Al*
Max wt%	9-11	0.55	0.05	0.45	0.20-0.45	0.1	0.05	Bal.
PSD [µm]	20-63							
AM – AlSi10Mg composition limits [106]								
Element	*Si*	*Fe*	*Cu*	*Mn*	*Mg*	*Zn*	*Ti*	*Al*
Max wt%	9-11	<0.55	< 0.05	< 0.45	0.2-0.45	<0.1	< 0.15	Bal.
PSD [µm]	20-63							

3.5 AlSi9Cu3(Fe) for AM purposes

Recently, some researchers [96,107–109] started studying AlSi9Cu3 for additive manufacturing due to its widespread use in the automotive sector.

Atomized powders in size 20-63 µm are printed through L-PBF to produce components; **Table 13** reported the printing parameters from the literature. Nevertheless, the powder composition for additive manufacturing differs from the composition intended for casting. In

Table 14, the composition of alloy AlSi9Cu3 intended for L-PBF and utilized in literature's works was shown, while in **Figure 15**, the microstructures of

AlSi9Cu3(Fe) alloy obtained through different production process (HPDC delivery state and powder printed in this work through L-PBF) are shown.

Table 13. Literature L-PBF printing parameters AlSi9Cu3

Parameters	Values	References
Scanning strategy	Chess board	[107,108,110]
Hatch spacing [µm]	150	[107,108,110]
	120	[96]
	90	[97,109]
Layers thickness [µm]	50	[96,107,108,110]
	30	[97,109]
Laser power [W]	400	[107,108,110]
	350	[96]
	275	[97,109]
Laser Spot Size [µm]	82	[96,107,108,110]
	65	[97,109]
Speed [mm s−1]	1300	[107,108,110]
	1200	[96]
Atmosphere	Argon	[97,107–110]
	Nitrogen	[96]
Powders diameter [µm]	avg. 40	[107,108,110]
	avg. 42.6	[96]
	20-63	[97,109]
Platform Temperature [°C]	30	[97,109]

Table 14. AlSi9Cu3(Fe) composition designed for additive manufacturing.

AM – AlSi9Cu3 composition limits [111]						
Element	*Si*		*Cu*	*Mg*		*Al*
wt%	8-11		2-3.5	0.1-0.5		Bal.
PSD [µm]				Laser PBF		
AM – AlSi9Cu3 composition limits [97]						
Element	*Si*	*Fe*	*Cu*	*Mg*	*Ti*	*Al*
ICP wt%	8.92	0.339	2.367	0.028	0.007	Bal.
PSD [µm]				20-63		
AM – AlSi9Cu3 composition limits [108]						
Element	*Si*	*Cu*	*Fe*	*Mg*	*Zn*	*Al*
wt%	8.9	3.1	1.2	0.3	0.01	Bal.
PSD [µm]				40		

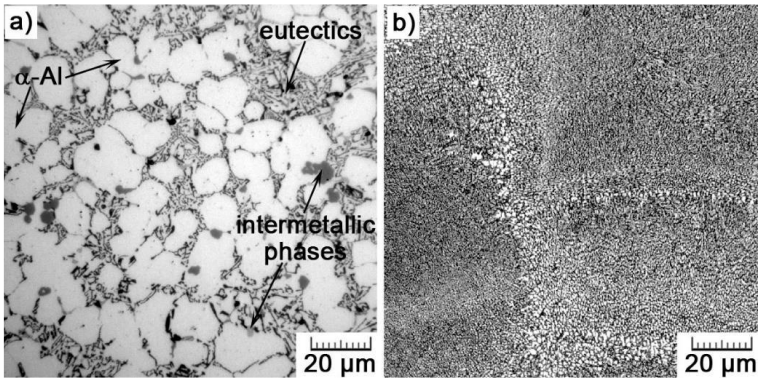

Figure 15. OM (a) Microstructures of HPDC alloy AlSi9Cu3(Fe) and (b) L-PBF AlSi9Cu3(Fe). Image reproduced from [110].

3.6 Heat treatment in AM Al-Si alloys

Annealing and solubilization followed by artificial ageing (T6) are two of the most diffused heat treatments considered for L-PBF AlSi alloys.

Mainly, in T6 treatment, the solution treatment exposes the alloy to high temperatures (up to 540 °C and below the eutectic temperature): the super-saturated solid solution α-Al after L-PBF has a ultrafine cellular structure and networks are rich of intercellular eutectic silicon and intermetallic phases. Literature research reports that the cooling rates in L-PBF process is in the range 10^6-10^8, leading to supersaturated structure where Si solubility in the Al matrix is extended up to 8 wt%, instead of 1.65 wt% of the equilibrium condition [112].

The obtained microstructures are inhomogeneus doing to the different thermal history of the main regions and are characterized by coarse grain in the melt pool boundaries and fine grains in the melt pool core regions. **Figure 16** shows OM and SEM microstructures of a L-PBF AlSi9Cu3 alloy printed through meander strategy.

Heat treatment cycles in additive manufacturing specimens are similar to the type used in cast aluminium alloys. Mainly, the rapid cooling leads to an α-Al phase oversaturated: in this sense, some Authors suggested the suppression of the solution temper step, preferring a T5 heat treatment to stimulate the precipitation hardening, as previously discussed [7]. Heat treatments stimulate the precipitation strengthening by precipitation from the SSSS of clusters of Mg, Si and Cu. Then, GP zones and β phases nucleate (needle-like β'', road-like β' and finally plate-like

β). **Table 15** shows the main intermetallic phases that characterize the AlSi10Mg state of the art alloy and the AlSi9Cu3 alloy.

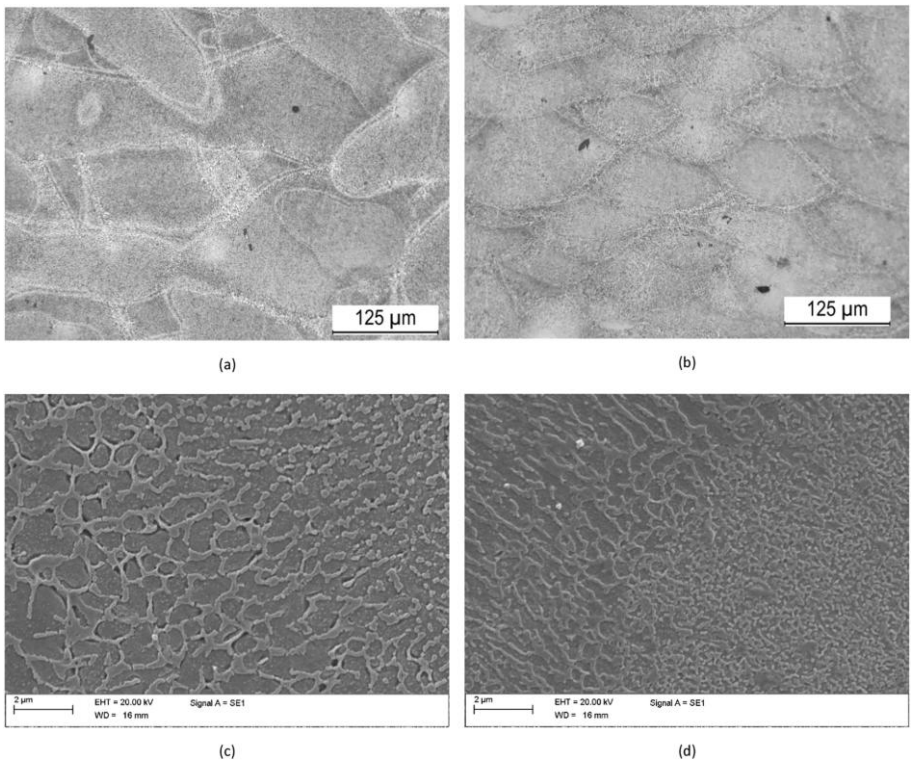

Figure 16. OM and SEM images of L-PBF AlSi9Cu3 alloy. Image reproduced with permission of the publisher [97].

Table 15. Intermetallic phases in AM Al-Si alloys

Alloy	Phases	Ref.
AlSi9Cu3 L-PBF	β-Al_5FeSi; Al_8Fe_5 θ-Al_2Cu; Al_7Cu_2Fe Al matrix ; Eutectic Si	[107,113]
AlSi10Mg L-PBF	β-Mg_2Si Al matrix ; Eutectic Si	[101]

3.7 Recyclability protocol by atomization

Atomization represents a semi-direct recycling technique. The recycling of aluminium scrap consists of creating metal powders and then printing samples by L-PBF. This approach permits lower energy usage and can reduce waste. Similarly to what was performed for recycling through the casting route, a protocol for the evaluation of the powders was considered. This protocol consists of four main subtasks, as in the block scheme in **Figure 17**.

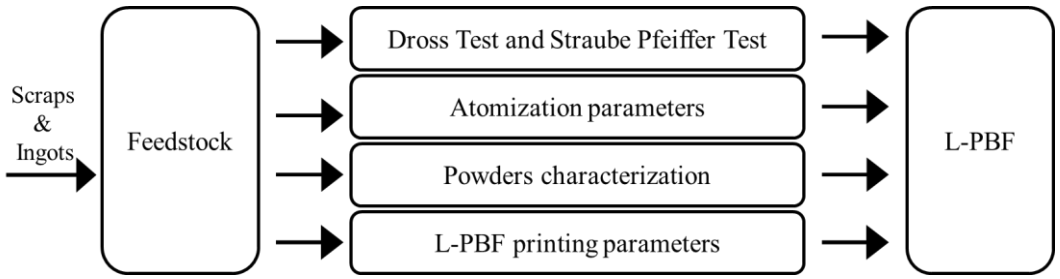

Figure 17. Block-diagram. Investigation protocol

The first subtask is the same as the one already conducted in the casting recyclability protocol and consists of feedstock analysis employing the dross test and Straube Pfeiffer test.

The second task involves selecting the atomization parameters, such as inlet pressure and melting temperature. Gas atomization was performed on the melted alloy using parameters as reported in paragraph 6.2.1. Atomization parameters were selected considering previous work on Al alloys using the same apparatus, [114].

Then, the third sub-task consists of analysing the powders in terms of composition, particle size, density and rheology measures, as the metodology methods suggested by Authors in [115]. If the powder results in good powder quality in terms of particle size and rheology measurements (such as compressibility and flowability, [116], the fourth step is printing specimens through L-PBF by selecting the printing parameters.

The powder acceptability criteria delves into obtaining rheology results similar to the state-of-the-art values, considering as references the most common powders of AlSi10Mg present in the market [117].

The following Ishikawa diagram [118] was prepared and considered to keep the AM process under control (**Figure 18**), while all recycling steps are summarized in **Figure 19**.

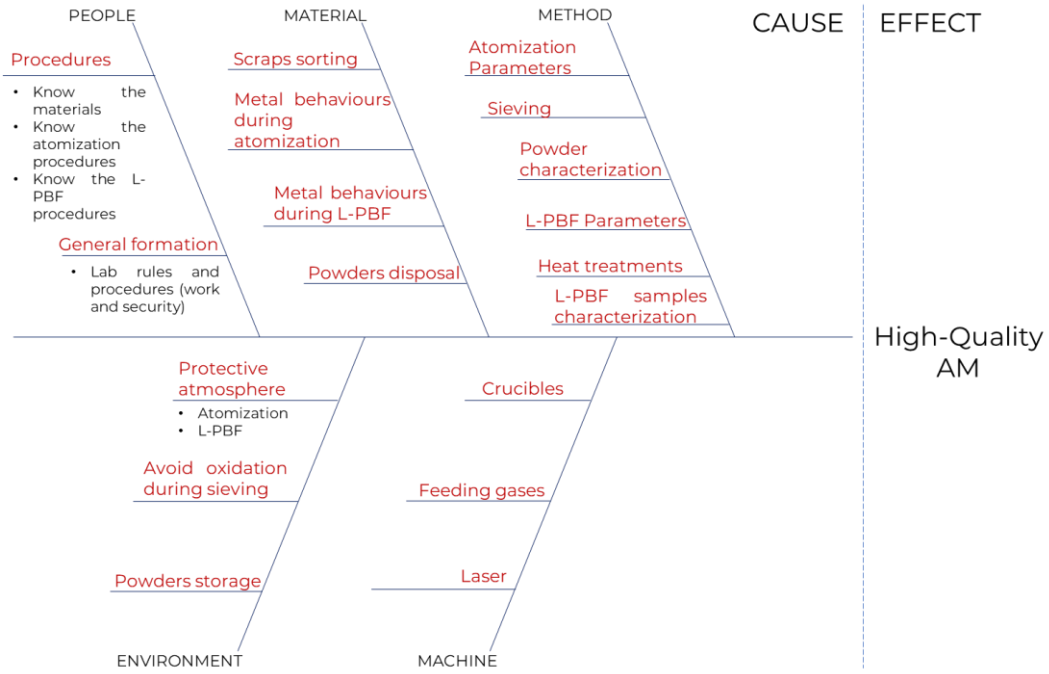

Figure 18. Ishikawa diagram cause-effect considered during the AM.

After the atomization and the powder characterization, the printing parameters must be selected, starting from the state of the art parameters for AlSi9Cu3(Fe) alloy. Firstly, the chamber atmosphere and the scanning strategy must be selected, then the selected process parameters must be evaluated through samples characterization. Different specimens were printed: cubes, dogbones, and bars.

Cubes aim to characterize the printing parameters and to evaluate the effect of the heat treatment. In fact, heat treatment such as T6 are normally performed in L-PBF specimens.

Mechanical samples aim to characterize the mechanical response of the L-PBF samples obtained from scrap powders and from secondary ingot aluminium alloys, in as-built conditions or after heat treatment.

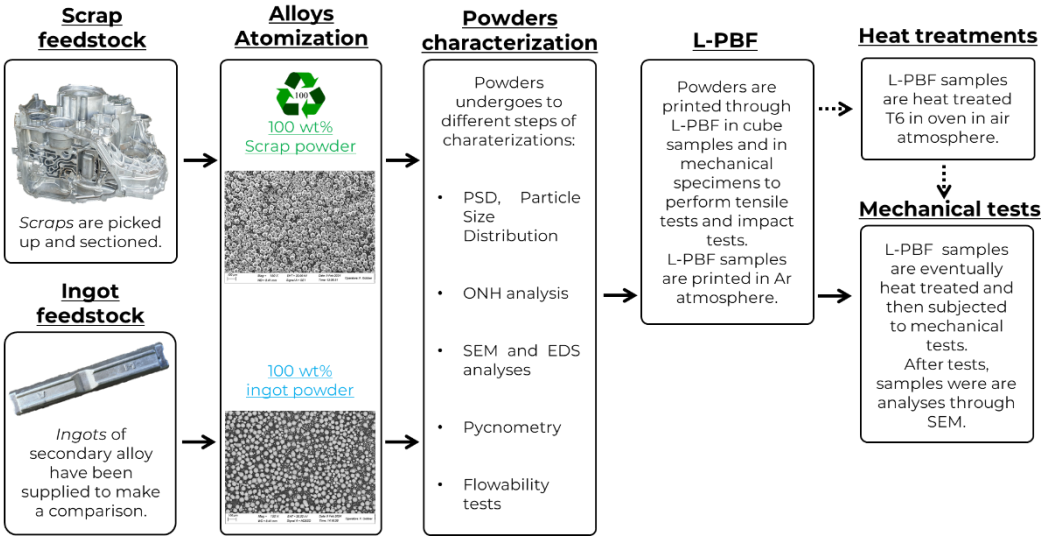

Figure 19. Steps in recycling alloys through atomization and printing route.

Chapter 4

4 Recycling AlSi7Cu0.5Mg by GC

The recyclability protocol detailed in section 2.5 was applied to scrap alloy AlSi7Cu0.5Mg. Tests gave positive results regarding castability and internal porosities of the scrap. In particular, section 1.4 and ***Table 3*** *depict the recycling route selected.*

From this perspective, multiple re-meltings of the same alloy were performed after the first re-melt of scrap alloy to evaluate the feasibility of the recyclability protocol. Those tests were conducted using only scrap alloy; concurrently, identical tests were performed on scrap alloy alloyed with 1 wt% Cr and scrap alloy addition with 2 wt% Cr. The choice of Cr has been discussed previously in 2.3.1. Such tests want to point out the maintenance of microstructural properties with the re-melting steps.

In industrial practice, scrap alloy is added in controlled amounts to ingot alloy. From this point of view, castings with different ratios of scrap/ ingot were performed: 100 % ingot, 25/75, 50/50, 75/25 and 100 % scrap. Such tests want to point out the maintenance of the mechanical properties of the alloy despite the addition of scrap, evidencing the possibility of casting components only using new scraps.

The final part of the chapter delves into the obtained results.

This chapter is based on:

Fracchia, Elisa. "Effect of Chromium Content and re-melt Process on the Properties of AlSi7MgCu0,5 Alloy". Daccò Prize-winning manuscript (Associazione Italiana di Metallurgia).

And

Fracchia, Elisa; Rosso, Mario; ACTIS GRANDE, Marco. "Effetto del tenore di lega rifusa sulle proprietà meccaniche di getti AlSi7MgCu0.5". In Proceedings 39° Convegno Nazionale AIM.

4.1 Materials and Methods

In the following sub-paragraphs, all the alloys characterization and the sample production are detailed.

4.1.1 Alloy feedstock and casting process

The feedstock materials, in the form of scrap and ingot, were sectioned, and samples for metallographic analyses were prepared to check the microstructures, the hardness and the chemical composition.

Scrap and ingot of alloy AlSi7Cu0.5Mg were delivered already cut and were eventually sectioned in smaller pieces. Details on feedstock are shown in **Figure 20**, while alloys composition is reported in **Table 16**.

Figure 20. AlSi7Cu0.5Mg feedstock. A: scraps; B: ingot.

Dross test and Straube Pffeifer test were performed and the cross section of the obtained samples is show in **Figure 21**. To perform such tests, the alloys are melted in an electrical furnace using a graphite crucible, and then a certain amount of alloy is poured into a specific crucible in the dross-test machine apparatus. Into the apparatus, the crucble filled with the molten alloy is placed into a specific chamber and the alloy solidification is done under a vacuum at 2-3 mbar; during the solidification the inclusions present into the melt flow to the alloy bath surface.

The Straube Pfeifer test permits the evaluation of gas inclusions into the metal; the alloy is melted into a furnace, and the melted alloy is placed into the Dross test/ Straube Pfeiffer test apparatus, where it solidifies under vacuum at about 30 mbar.

Table 16. AlSi7Cu0.5Mg compositions measured through SEM-EDS

AlSi7MgCu0.5 - ingot								
Elements	*Si*	*Fe*	*Cu*	*Mn*	*Mg*	*Zn*	*Ti*	*Al*
wt%	7.3	0.1	0.7	-	0.4	-	-	Bal.
AlSi7MgCu0.5 - scrap								
Elements	*Si*	*Fe*	*Cu*	*Mn*	*Mg*	*Zn*	*Ti*	*Al*
wt%	7.6	0.1	0.6	-	0.4	-	-	Bal.

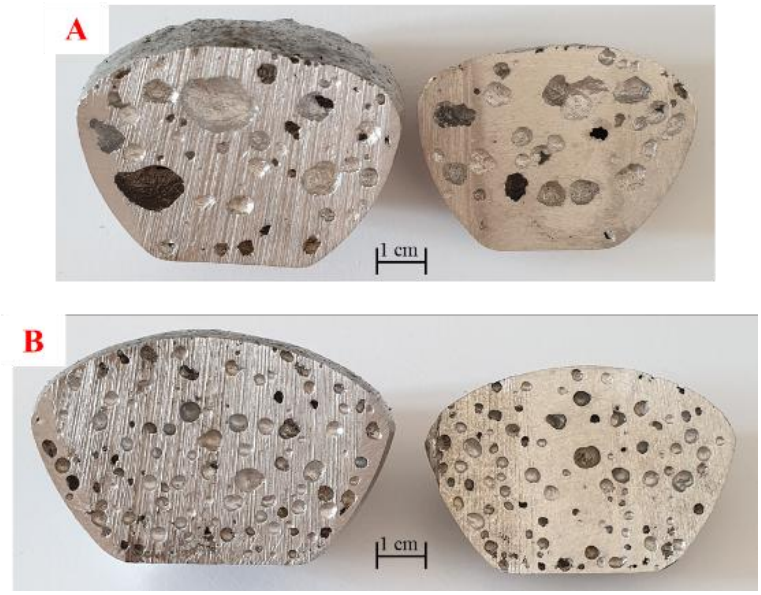

Figure 21. Ingot (left side) and Scraps (right side) alloys AlSi7Cu0.5Mg. A. Dross test sample; B: Straube Pffeifer sample.

After the composition assessment, the alloys were melted using an electric furnace and were cast into a steel mould to obtain samples for metallographic analyses and mechanical tests. Details about moulds and casted samples are shown in **Figure 22**. Particularly, cast in **Figure 22**-A is characterized by the spruer and

the risers, while the two obtained specimens has rectangular shape and dimensions 125 x 25 x 15 mm. Samples casted for microstructural analyses have a tendentially cylindrical shape, from which the surface layer will be removed to make the samples.

Cr alloying was performed by adding it in the molten alloy: Cr is added in powder form to facilitate its melt and diffusion into the aluminium bath (Metalpolveri S.r.l., 400 mesh). Chemical composition and powder size of Cr are shown in **Table 17**.

Figure 22. Casted samples and mould. A: samples for mechanical tests; B: mould for casting samples for mechanical tests; C: sample for microstructural analyses; D: crucible used for casting samples for microstructural analyses.

Table 17. Metallic Cr powder. Physical and chemical properties (producer data).

Granulometric size [%]				
0–38 µm	*38-45 µm*	*45-63 µm*	*53-63 µm*	*63-106 µm*
50 min.	30 min.	15 max.	0.5 max	-

Chemical composition [wt %]						
Al	*Fe*	*Si*	*C*	*N2*	*S*	*Cr*
0.01 max	0.2 max	0.1 max.	0.05 max.	0.1 max.	0.01 max	bal.

Gravity casting involves melting the alloy in an electric furnace using a graphite crucible with a capacity of 1 kg. The scrap and ingot parts must be further cut to facilitate the melting into the crucible, and then the electric furnace is set to reach 800 °C, to ensure all the alloy is melted. Subsequently, after the melting, the alloy is poured into the mould. The mould, previously pre-heated in a separate furnace at 250 °C, is ready to be filled by the molten alloy. After casting, two minutes are attended before removing the cast from the mould. The cooling will be finalized by quenching the cast into water at room temperature. During the casting, additives (refiners, modifiers) were not inserted.

As regards re-melting tests, **Table 18** summarid the samples cast. Type ‘a’ sample does not contain Cr, while types ‘b’ and ‘c’ contain 1 wt% and 2 wt% of Cr.

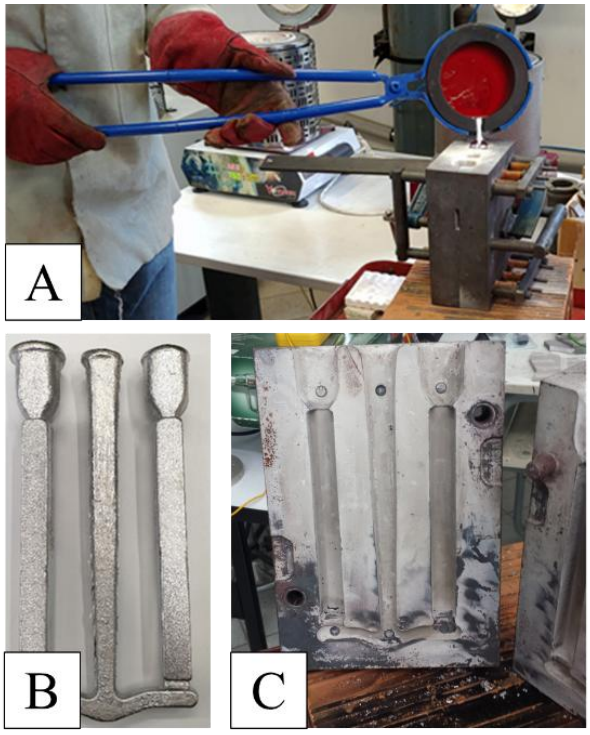

Figure 23. Manual gravity casting. A: casting procedure; B: cast for mechanical samples; C: mould for mechanical samples.

Table 18. AlSi7Cu0.5Mg remelting tests. Roman numerals indicate the number of re-melting. (Type 1 samples).

Sample's name	Samples type	Description
I-a	AlSi7Cu0.5Mg_I	Scrap alloy melt and cast in 5 brick-shaped samples (5 per type)
I-b	AlSi7Cu0.5Mg_1%Cr_I	
I-c	AlSi7Cu0.5Mg_2%Cr_I	
II-a	AlSi7Cu0.5Mg_II	4 brick samples melt and cast in 3 brick-shaped samples (3 per type)
II-b	AlSi7Cu0.5Mg_1%Cr_II	
II-c	AlSi7Cu0.5Mg_2%Cr_II	
III-a	AlSi7Cu0.5Mg_III	2 brick samples melt and cast in 1 brick shaped samples (1 per type)
III-b	AlSi7Cu0.5Mg_1%Cr_III	
III-c	AlSi7Cu0.5Mg_2%Cr_III	

The electric furnace consumption was measured during the alloy melt; the results are shown in **Figure 24**. Results refer to three subsequent cast steps of a certain amount of alloy progressively decreasing after each casting.

In the first melt, the alloy required 54 minutes to melt, and the absorbed energy was 0.91 kWh. The second melt step with a hot crucible was 37 minutes, and the absorbed energy reached 1.3 kWh (0.39 kWh for the melt). In the third melting step, the absorbed energy reached 1.6 kWh (0.3 kWh for the melt), and the remaining alloy required about 20 minutes to melt.

The decrease in time in the different remelting is due to the decrease of the alloy amount in the crucible, while the furnace consumption has a linear increase with respect to the time. For each melt step, the alloy was cast to obtain small bricks; one brick was used to study the alloy at the specific melting step, while the other samples were re-melted to cast other bricks. **Table 20** summarizes the sample types.

Castings with different ratios of scrap/ ingot were melted in the same condition previously explained and then cast in the form of bars (two bars for each casting) and were performed three casting for each condition.

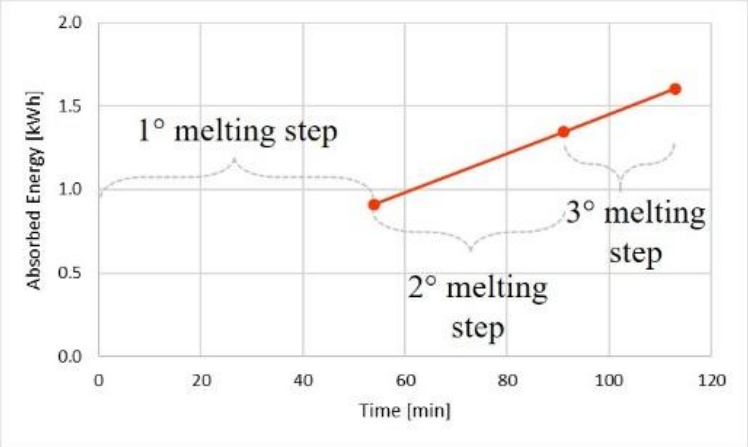

Figure 24. Subsequent melting steps in cast AlSi7Cu0.5Mg alloy.

In this second characterization, five types of samples are cast using variable amounts of scrap, as summarized in **Table 19**.

Table 19. AlSi7Cu0.5Mg cast with variables charge. (Type 2 samples).

Sample's name	Samples type	Description
A	AlSi7Cu0.5Mg_i	100 w.t.% ingot alloy
B	AlSi7Cu0.5Mg_75_25	75 w.t.% ingot alloy + 25 w.t.% scrap
C	AlSi7Cu0.5Mg_50_50	50 w.t.% ingot alloy + 50 w.t.% scrap
D	AlSi7Cu0.5Mg_25_75	25 w.t.% ingot alloy + 75 w.t.% scrap
E	AlSi7Cu0.5Mg_s	100 w.t.% scrap alloy

4.1.2 Microstructural characterizations

The extended recyclability protocol is shown in **Table 20**. Microstructures were characterized in all specimens.

The microstructural characterization procedure is conducted using both the Optical Microscope (OM - Leica Microsystems MEF4M) and Scanning Electron

Microscope equipped with an EDS probe (SEM Zeiss EVO 15 and Oxfor Ultim Max 40 probe) to analyse semi-quantitatively the intermetallic phases.

Along with OM observation, image analysis instruments were adopted to characterize microstructural features as eutectic silicon shape, intermetallic shape and Secondary Arms Spacing SDAS of the Al-matrix. SEM-EDS analyses were used to characterize the intermetallic phases in the specimens.

Moreover, the fracture surfaces can be observed after mechanical tests (post-mortem characterization) to get further information about the fracture behaviour.

The specimens for fracture surfaces were cut to reduce their height in order to put them into the SEM chamber, cleaned in a sonic bath with acetone and then coated with a nanometric layer of gold by sputtering to increase their conductivity (Agar Scientific Auto Sputter Coater AGB7341). After the sputtering, samples are observed at the SEM to assess the fracture mode.

Specimens for OM and SEM-EDS are grinded using silica paper from 200 to 2400 grit; then specimens were polished through colloidal silica (0.04 μm) up to obtain a mirror-like surface and eventually etched through Keller reagent (E407-23 Standard Practice for Microetching Metals and Alloys).

Differential scanning calorimetry analyses DSC (Setaram DSC-TGA 92 16.18) were performed to assess the main transformation (eutectic, melting) up to 600 °C at 10°C/min as heating and cooling ramps, using a small piece of the alloy of few grams.

Table 20. Recyclability Protocol and tests on AlSi7Cu0.5Mg alloy

Recyclability Protocol		
Characterization	*Details*	*Instruments*
Feedstock characterization	Dross test Straube Pfeiffer test Microstructural analyses	SEM-EDS Optical Microscope DSC
First casting test	Type 1 samples Evaluation of re-melting effects	SEM-EDS Optical Microscope DSC
Characterization	*Details*	*Instruments*
Gravity Casting and cast characterization	Type 1 samples Cast of samples with and without element additions (Cr) and evaluation of re-melting effects	SEM-EDS Optical Microscope DSC
	Type 2 samples Cast of samples (with different amounts of scrap alloy inside) for microstructural and mechanical analyses: impact and tensile tests.	SEM-EDS Optical Microscope Charpy machine Tensile test machine
Post-mortem characterization	Fracture analyses of tensile and impact samples	SEM

4.1.3 Mechanical tests

Microhardness was characterized on a Vickers and Knoop micro-durometer Leica Type VMHT through microvickers indenter by applying 50 g of load for 15 seconds.

Type 2 specimens (**Table 20**) were machined to obtain mechanical samples to perform tensile tests (5 specimens) and impact tests (4 specimens) as in [119]. Impact test samples are 55 x 10 x 10 [mm] while tensile samples were realized in rectangular shape having 6.35 mm as width, gage length of 25.4 mm, thickness of 2 mm and and overall leghth of 101.6 mm, as suggested in ASTM ASTM B557-15(2023), subsize specimen.

Room temperature uniaxial tensile tests were performed on a 100 kN Zwick-Roell GmbH &Co machine (SMT1-FR100TL.A80). Impact tests were performed on a 50 J Zwick-Roell GmbH &Co. machine (TG5113E) using samples without the notch.

4.2 Results

4.2.1 Microstructural characterizations: scrap AlSi7Cu0.5Mg

The noticed intermetallic phases are shown in **Figure 25**. AlSi7Cu0.5Mg is mainly characterized by the α-Al matrix and the eutectic silicon. The copper addition permits the nucleation of the θ-Al_2Cu intermetallic phase and the Q-phase Q-$Al_5Cu_2Mg_8Si_6$, while the Fe leads to the nucleation of π-$Al_8Mg_3FeSi_6$.

The critical amount of Fe (formula (2) in paragraph 2.4) indicates the maximum amount of iron that can be accepted in order to avoid the nucleation and enlargement of a high amount of Fe-based intermetallic phases. Particularly, the critical Fe is strictly related to the maintenance temperature. The alloy must remain as short as possible at the critical temperature (see formula (3) in paragraph 2.4) to decrease the possibility of nucleation of harmful iron intermetallics.

Sludge Factor (SF) = 0.1 in both alloys

Fe_{cr} = 0.50 wt% in ingot and 0.52 wt% in scrap

Temperature (°C) = 646 in both alloys

In **Figure 26**, DSC thermograms are shown during the heating ramp (heating rate of 10 °C/min) for both ingot alloy (**Figure 26**-A) and scrap alloy (**Figure 26**-B) in the as-delivered state; numbers indicate the main transformations occurring during the melting, while

Table 21 summarizes the transformations.

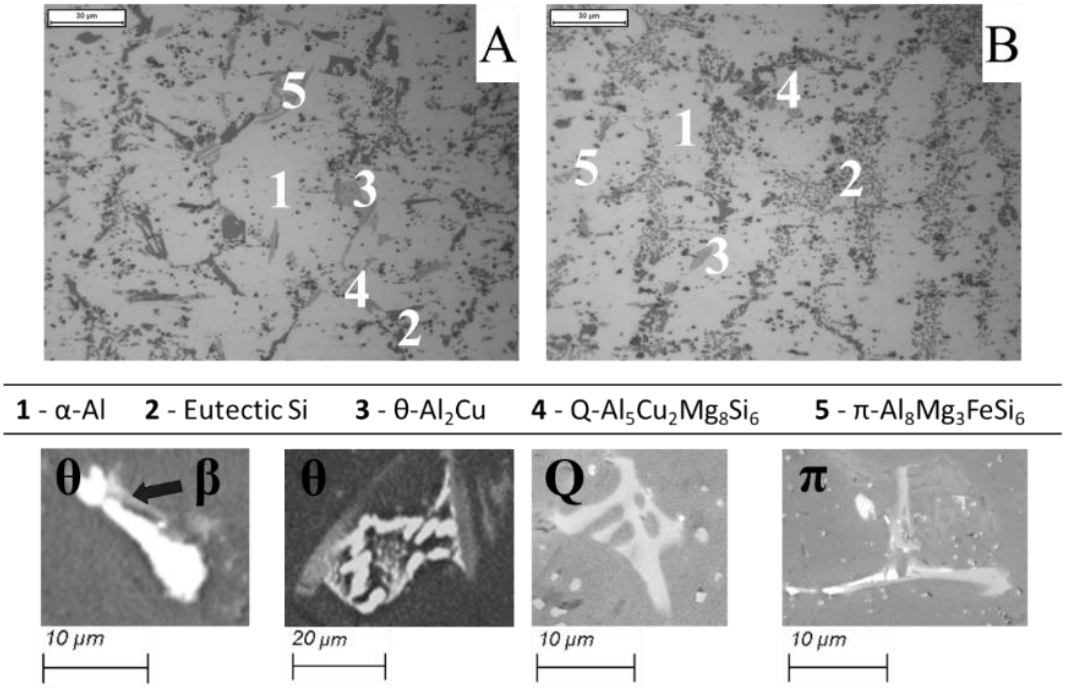

Figure 25. Optical microscope images, magnification 500 X (marker 30 μm). Intermetallic phases in AlSi7Cu0.5Mg. A: ingot alloy; B: scrap alloy. On the bottom side, details of intermetallic phases observed by SEM.

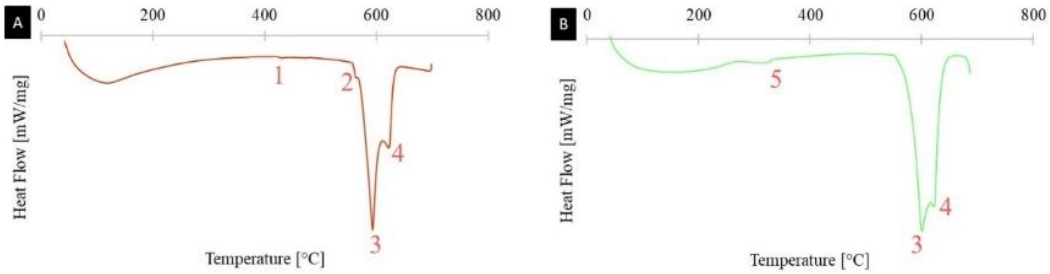

Figure 26. DSC thermograms. A: ingot alloy AlSi7Cu0.5Mg. B: scrap alloy AlSi7Cu0.5Mg.

Table 21. Peaks observed in DSC analyses of alloys AlSi7Cu0.5Mg.

DSC Peaks	Phase	Reference
1	θ-Al_2Cu dissolution	[120]
2	Q-$Al_5Cu_2Mg_8Si_6$ or β dissolution	[121]
3	Main eutectic reaction	[122]
4	Melt of the dendritic network	
5	Semi-coherent phases nucleation of θ′ and Q′ and dissolution	[120,122,123]

4.2.2 Re-melting tests

As shown in **Table 18**, a certain amount of alloy is lost during the melting process. This behaviour is due to the nucleation of scores, sludge and formation of alumina on the melt surface.

Moreover, a certain amount of sludge nucleated because of the high furnace temperature (800 °C) and the high Cr content that promoted its nucleation, as introduced in 2.3.1. In this context, the sludge formation depends on the amount of Fe, Mn and Cr, as reported in 2.4 and 4.2.1. The heating curves of DSC thermograms are shown in

Figure 27.

Mainly, literature researches evidenced that the exothermic peak *1* can be associated with the precipitation of coherent β″, θ″ or Q″ phases. Exothermic peak *2* shows matches to the precipitation of semi-coherent phases β′, θ′ or Q′ [122,123].

The endothermic peak is probably the Q phase (Q-AlSiCuMg) [9], and it was detected in samples III-a, III-b, and III-c. Peak *4* indicates the eutectic reaction, and peak *5* refers to the melt of the dendritic network.

In particular, the temperature of the melt of the dendritic network (peak *5*) increases with the increase in the number of re-melting.

Furthermore, with equal numbers of re-melting, the temperature increases with increasing in Cr amount. Conversely, the temperature of the main eutectic phase (peak *4*) decreases with the increase in the numbers of re-melting.

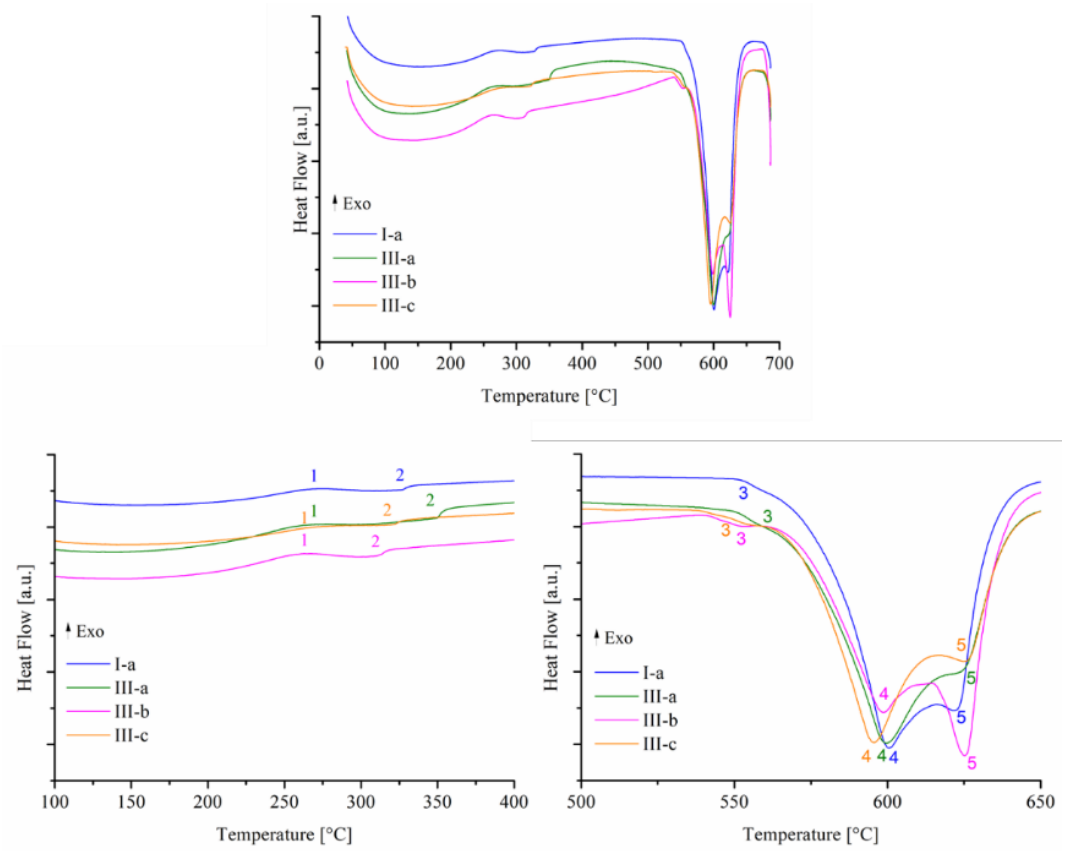

Figure 27. DSC. Heating curves in re-melted samples.

With equal numbers of re-melting, the peak temperature decreases with increasing in Cr amount.

Overall, the temperature range between the primary eutectic reaction and the melt of the dendritic network increases with increasing the number of re-melting and with the increase in the Cr amount.

Table 22 shows the microstructures of samples summarized in **Table 18**, after the re-meltings.

Microstructural observation evidenced the presence of the intermetallic phases detected by DSC. Notably, the shape and size of such phases undergo variation and enlargement with increased re-melting numbers.

Further re-meltings of the alloy cause an enlargement of the sludge particles, that will affect the microstructure and the mechanical behaviour of the alloy [124].

Table 22. Microstructures in re-melted specimens AlSi7Cu0.5Mg

Re-melting of scrap AlSi7Cu0.5Mg – Samples 'a'		
1° re-melting	2° re-melting	3° re-melting
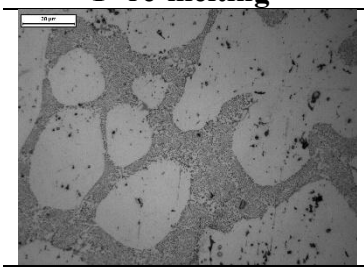	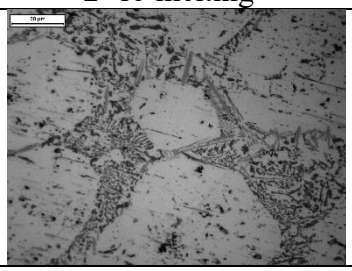	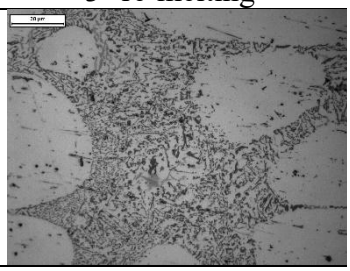
Re-melting of scrap AlSi7Cu0.5Mg – Samples 'b'		
1° re-melting	2° re-melting	3° re-melting
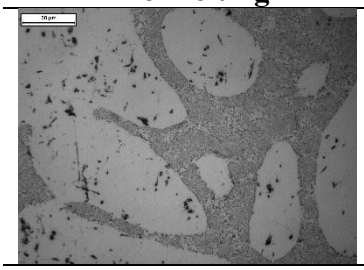	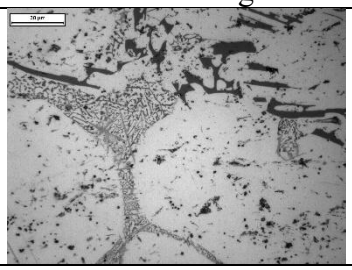	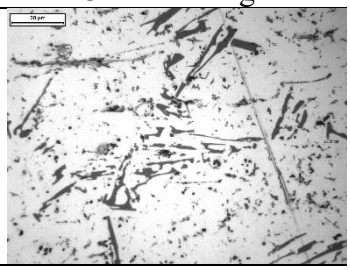
Re-melting of scrap AlSi7Cu0.5Mg – Samples 'c'		
1° re-melting	2° re-melting	3° re-melting
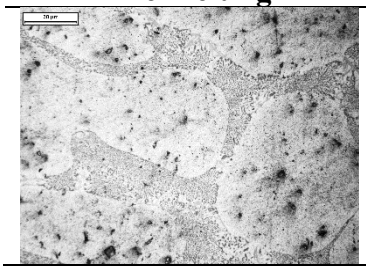	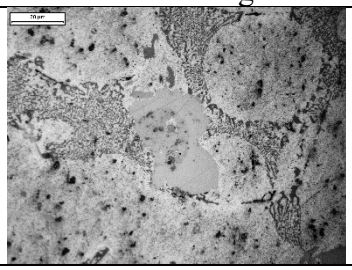	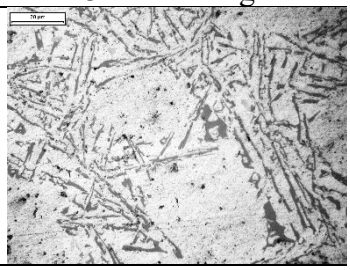

In the alloy type-a, similar microstructures were detected after re-melting. A slight change in eutectic silicon shape and size can be noticed already in specimen II-a. Moreover, in the type ‘a’ specimen, small rod-shaped Q-AlSiCuMg intermetallic phases were noticed by the microstructures and the EDS analyses, as shown in **Figure 28**.

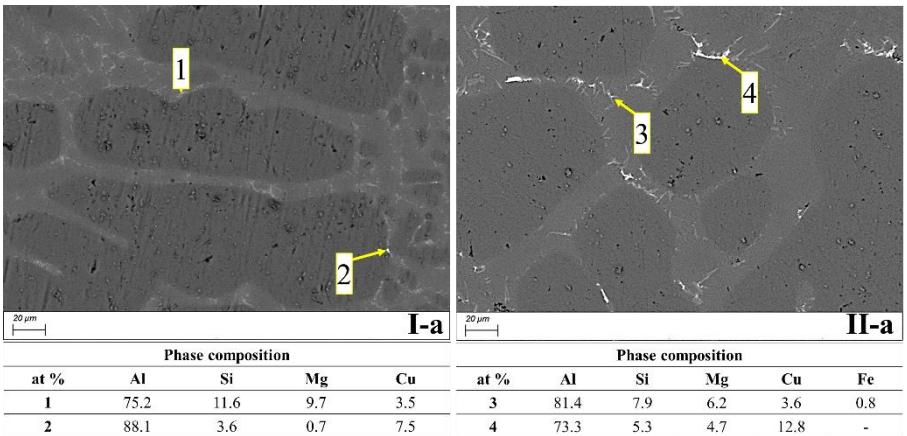

Phase composition				
at %	Al	Si	Mg	Cu
1	75.2	11.6	9.7	3.5
2	88.1	3.6	0.7	7.5

Phase composition					
at %	Al	Si	Mg	Cu	Fe
3	81.4	7.9	6.2	3.6	0.8
4	73.3	5.3	4.7	12.8	-

Phase composition				
at %	Al	Si	Mg	Cu
5	84.9	8.6	3.4	3.1
6	77.4	5.2	6.1	11.3

Figure 28. SEM-EDS analyses in re-melted specimens type ‘a’

After the first re-melt (sample II-a), the Mg_2Si Chinese script (black intermetallic phase) was noticed, along with the π-AlFeMgSi.

Large Cr-based intermetallic phases were observed after the second re-melting of alloy containing 2 wt% Cr. such intermetallic may be due to sludge and contain Al-Si-Cr-Fe. Particularly, the nucleation of Cr-Si intermetallic phases and Al-Cr-Si

is attended and described from some authors[125]. The nucleation of Al-Si-Cr intermetallic phases can be

The alloys' microstructure appears globular up to the second re-melt, while after the third re-melt the eutectic silicon change its shape resulting in a very coarse shape (**Figure 29** and **Figure 30**).

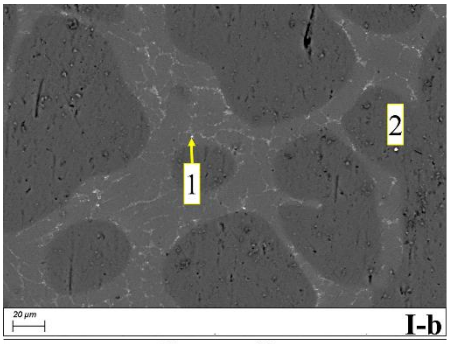

Phase composition							
at %	Al	Si	Mg	Cu	Fe	Cr	Mn
1	79.7	10.7	2.7	2.1	1.8	2.8	-
2	66.9	1	-	-	31.8	-	0.3

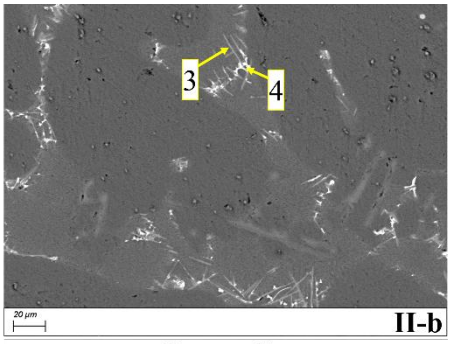

Phase composition						
at %	Al	Si	Mg	Cu	Fe	Cr
3	72.1	12.5	3.4	2.9	2.6	6.6
4	71	17.7	2.1	9.2	-	-

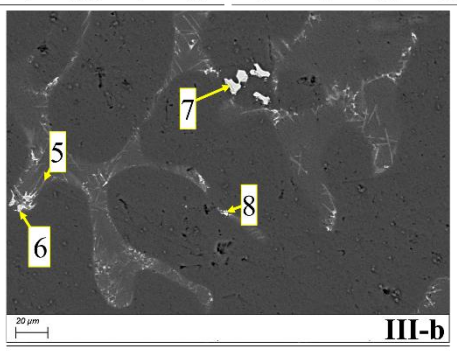

Phase composition							
at %	Al	Si	Mg	Cu	Fe	Cr	Ti
5	71.1	26.1	2	0.5	0.3	-	-
6	68.5	7.9	6	16.5	0.5	0.6	-
7	12.8	54.5	-	-	3	28.7	0.9
8	80.1	10.3	1.5	6.5	0.6	0.9	-

Figure 29 SEM-EDS analyses in re-melted specimens type 'b'

The secondary harm spacings SDAS change with the re-melting step and with the Cr addition. Nevertheless, the effect of the manual casting and elapsed time between the cast and the quench in water may affect the final measured SDAS.

The results of maeasured SDAS are shown in

Figure 31.

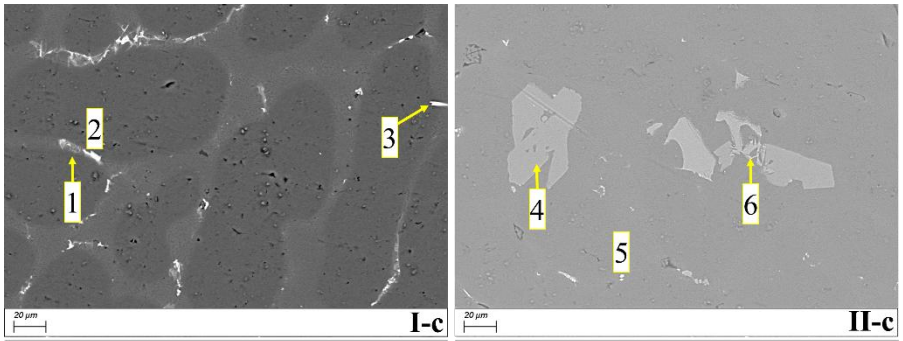

Phase composition

at %	Al	Si	Mg	Cu	Fe	Cr	Ti
1	72.5	12.4	11.8	3.4	-	-	-
2	76.3	11	-	1.1	5.6	6	-
3	23.5	49.8	-	-	1.2	24.1	1.4

Phase composition

at %	Al	Si	Mg	Cu	Fe	Cr	Ti
4	83.4	3.6	-	-	-	11.6	1.5
5	73.6	4.5	5	16.9	-	-	-
6	86.8	6.5	-	-	0.2	6.6	-

Phase composition

at %	Al	Si	Mg	Cu	Fe	Cr
7	60.1	21.6	-	-	0.6	17.7
8	74.1	2.6	1.9	21.5	-	-
9	79.4	9.8	3.9	0.5	3.1	3.4

Figure 30. SEM-EDS analyses in re-melted specimens type ‘c’.

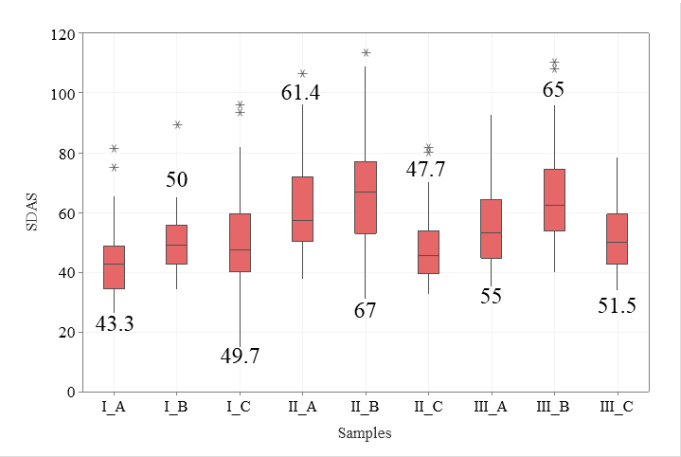

Figure 31. SDAS results in box plot for AlSi7Cu0.5Mg alloy with and without Cr additions after different re-melting steps.

Figure 32 shows the microhardness of the samples; mainly, after the first re-melt, the microstructures are characterized by α-Al and fine eutectic silicon.

After the second re-melting, all the alloys are characterized by an enlargement of eutectic silicon that appears in fine shape and acicular form; moreover, alloys with 2 wt% Cr show a certain amount of Cr-based intermetallic phase.

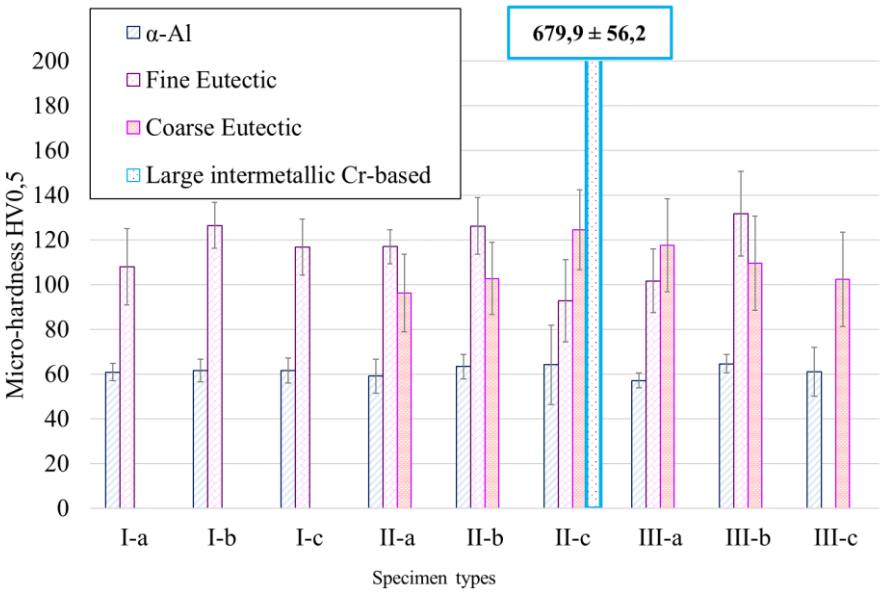

Figure 32. Microhardness values in re-melted specimens.

After the third re-melt, the microhardness of coarse eutectic increases and the microhardness of the refined eutectic decreases, while the large Cr-based intermetallics are less extended in sample 2 wt% Cr.

Results were also shown in box plot form in **Figure 33** in terms of eutectic and α-Al variations; from the box plots, it is possible to observe the presence of a few outline values depicted by asterisks. Moreover, values are less dispersed in α-Al measures at the first and third re-melt, while in coarse and refined eutectic micro-hardness results have large standard deviations.

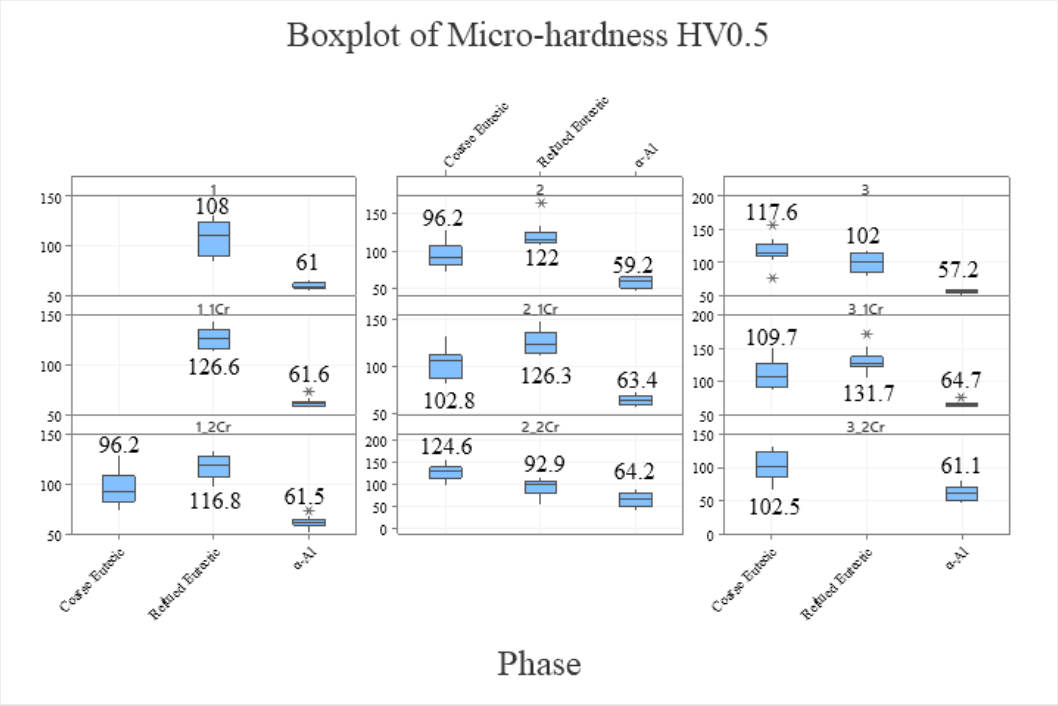

Figure 33. Box plots micro-hardness for each sample. 1, 2 and 3 indicate the re-melting steps.

4.2.3 Casting with variable amounts of scrap

Alloy microstructures are shown in **Figure 34**. The following phases were mainly noticed: π, Q, Al-θAl_2Cu, Fe-based intermetallics and eutectic Si.

After casting, θ-Al_2Cu precipitates can be very small, often in the range of nanometers [125]. In order to notice it through an optical microscope, some particular microstructures can be observed, as in **Figure 35** sample A, where θ phase is in the form Al-θAl_2Cu [126]. Even the metastable phases θ' and θ" phases can be observed in this alloy.

The Q phase typically forms during the solidification of the alloy, between 540 °C and 500 °C [127]; Q-$Al_5Cu_2Mg_8Si_6$ tends to nucleate at grain boundaries and interdendritic regions.

The π phase has a script-like form and nucleates when Mg is present. This phase was noticed in all samples (**Figure 35**). Eutectic silicon appears refined.

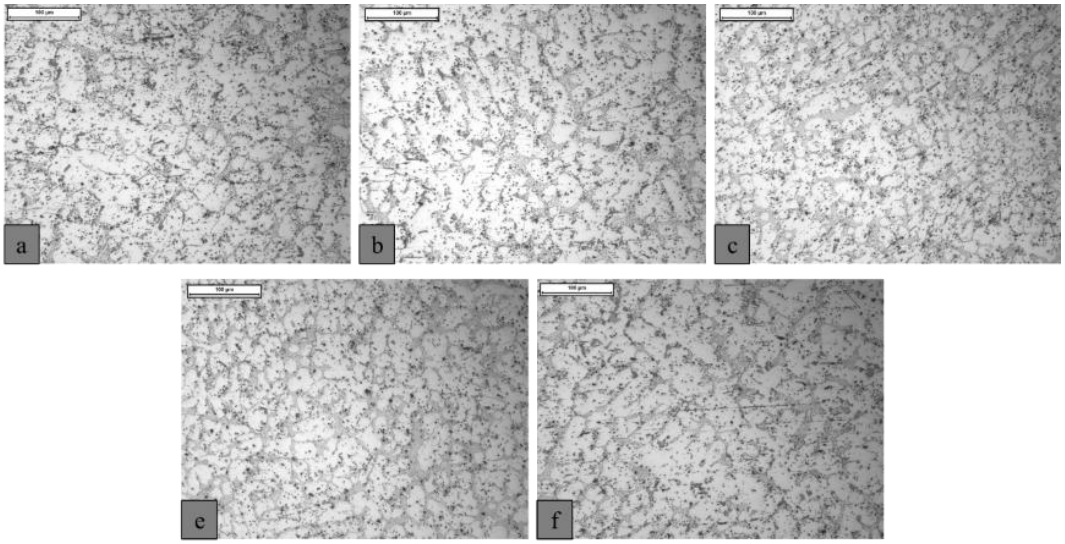

Figure 34. Microstructures of samples. a: 100 % ingot alloy; b: 25 % scrap; c: 50% scrap; d: 75 % scrap and e:100 % scrap.

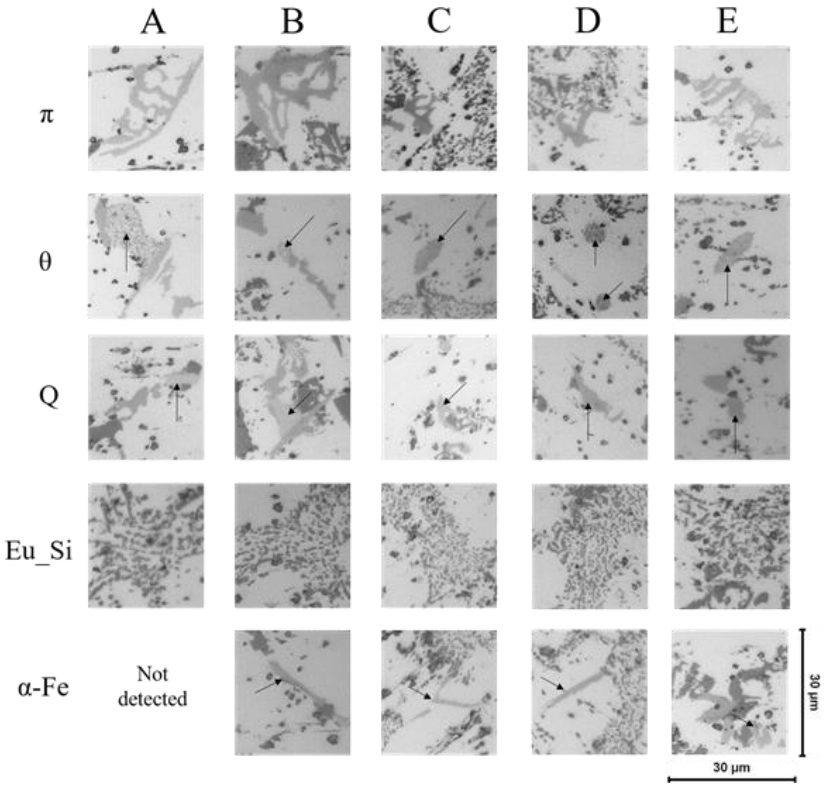

Figure 35. Details on intermetallic phases in alloys AlSi7Cu0.5Mg (OM images).

4.2.3.1 Microhardness results and statistic

Microhardness statistical values (average, standard deviations, quartiles, etc.) were calculated using the MiniTab software, and the results are graphically shown in **Figure 36**.

Samples type A are characterized by a higher microhardness than sample type E. Conversely, the dot plot graph clearly highlights a higher distribution of the data in alloy type A while alloy type E is the least dispersed data.

The increase in scrap amount leads to a decrease in microhardness: the microhardness decreases by 7% after 25 wt% of scrap addition and decreases by 11% if the amount of scrap is 50 wt%. Then, the microhardness values appear almost stationary.

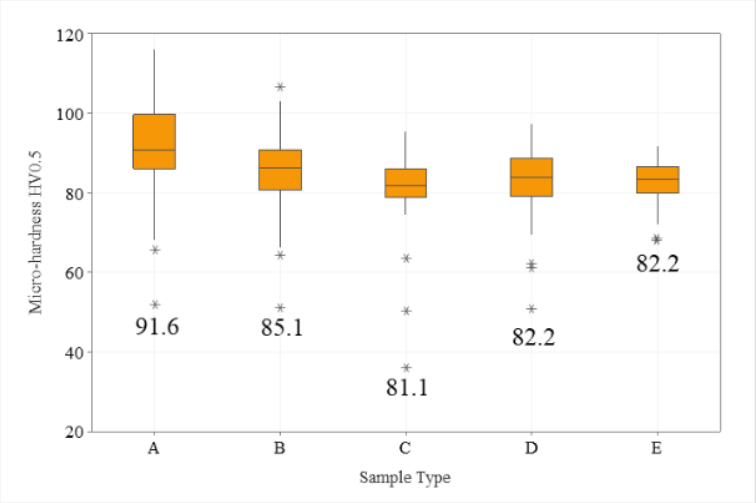

Figure 36. Box plot of micro-hardness measures

Figure 37 depicts statistical results for tensile tests in terms of R_m, $R_{p0.2}$ and elongation at rupture A%.

The box plots highlight a high standard deviation for all the specimens for all the measured properties, as clearly noticeable even from the dot plot.

Mainly, alloys that showed lower microhardness resulted in slightly higher average elongation at rupture. Alloy C shows the higher ultimate tensile stress of 171.3 MPa as the average value, while A specimens result in an average value of 169.6 MPa.

Alloys containing more than 50 wt % of scrap alloy are characterized by lower microhardness (**Figure 36**) and higher or slightly higher elongation at rupture A%.

The high standard deviation was due to the internal defects noticed inside casting; such defects were observed through SEM fracture analysis of the fracture surfaces. Fracture surfaces are shown in **Figure 38**.

From the fracture surfaces analysis was noticed a certain amount of oxide skins, mainly in specimens A and D. The micrograph of sample B shows the presence of dendrites. All the micrographs appear characterized by fragile fractures and cleavage.

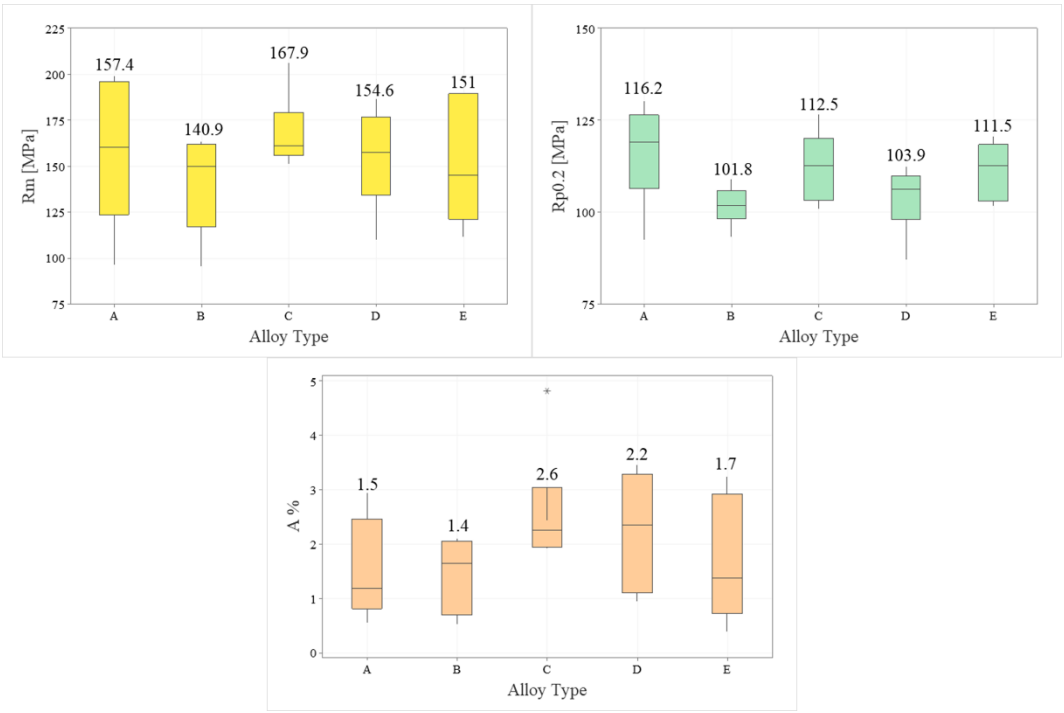

Figure 37. Box plots for tensile test results.

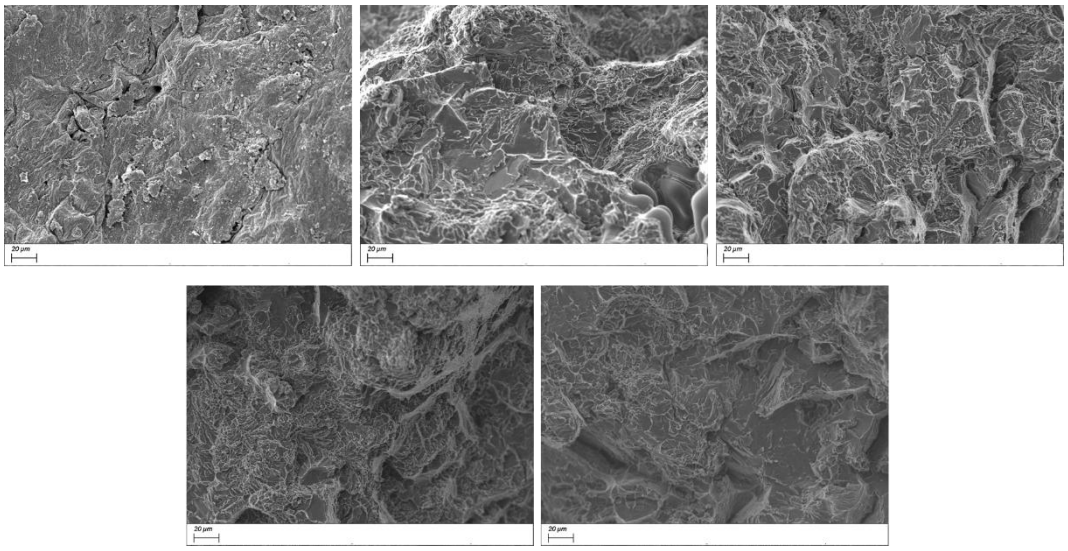

Figure 38. Fracture surfaces in tensile specimens.

4.2.3.2 Impact test results and statistic

In **Figure 39**, the box plot for impact test results is shown. Mainly, it can be clearly noticed a high standard deviation in absorbed energy for specimen type B, while sample type C showed a minor dispersion.

Particularly, such a difference in terms of absorbed energy was due to a certain amount of retained defects. Fracture analyses were performed on specimens that had the best results in terms of absorbed energies and micrographs, as shown in **Figure 40**.

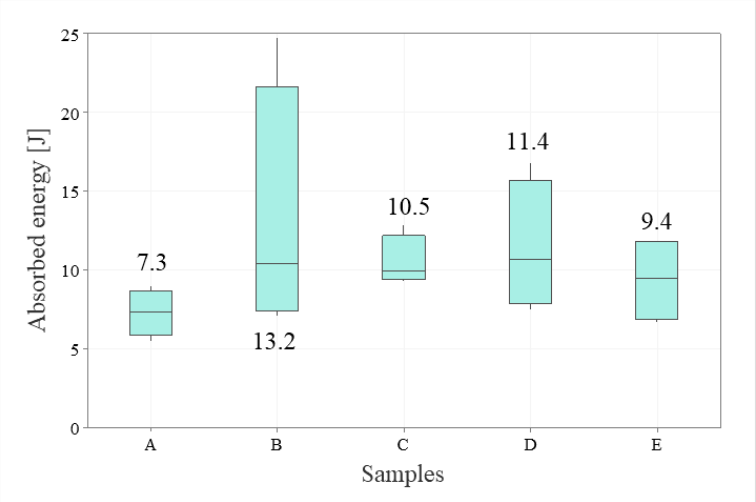

Figure 39. Box plot for impact test results.

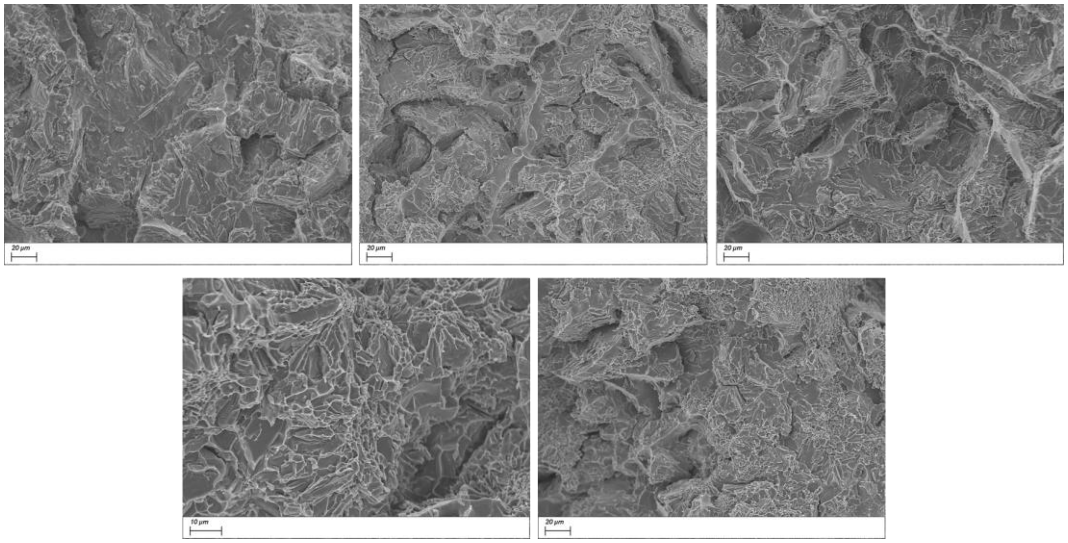

Figure 40. Fracture surfaces in impact test samples

4.3 Discussion

The characterization of alloy AlSi7Cu0.5Mg started from the castability tests on scraps. Tests performed highlight a good castability of the scrap alloy with a moderate increase in secondary harm spacings SDAS and an increase in the re-melting numbers (

Figure 31). Re-meltings cause a gradual change in eutectic silicon shape that changes from small and refined to a coarse microstructure, as shown in **Figure 41**.

The progressive evolution in eutectic shape was even assessed by micro-hardness measures that emphasize a gradual increase in coarse eutectic micro-hardness and, at the same time, a decrease in fine eutectic micro-hardness. Such a behaviour can be explained considering the intermetallic phases that nucleate into the eutectic phase. The increase in micro-hardness can be attributed to a progressively higher probability of indenting coarse intermetallic phases.

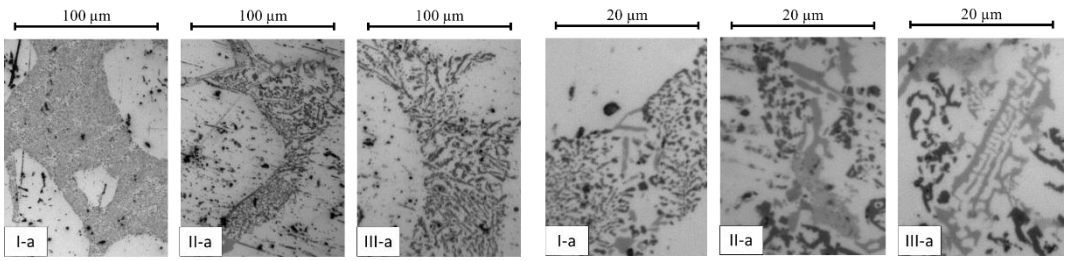

Figure 41. Upper images: details of eutectic silicon change during re-melting of AlSi7Cu0.5Mg. Lower images: details of intermetallic phase change during progressive re-melting of AlSi7Cu0.5Mg

Alloy AlSi7Cu0.5Mg continue to show good microstructural features even after the third re-melt, confirming the possibility of casting components through scrap alloy at least reused up to 3 times. Intermetallic phases were analysed through SEM-EDS analysis, and the results are shown in **Figure 28**. Intermetallic phases detected are mainly the Q phase and π-Fe phase.

The addition of 1 wt% Cr leads to a slight change in microstructures, mainly due to Cr-based intermetallic phases. A severe and inhomogeneous change in eutectic microstructure can be observed already after the second re-melt (**Figure 42**). Furthermore, the average eutectic micro-hardness increases with the Cr addition **Figure 33**. The increase in micro-hardness can be attributed to the intermetallic Cr-based phases present in the eutectic phase, which were detected by SEM-EDS analyses (**Figure 29**).

The addition of 2 wt% Cr leads to an increase in sludge particles inside the casting that can be embedded inside the melt during the casting, as in sample II-c (**Figure 30**). Even a coarsening of the eutectic phase can be noticed. Microstructure datails can be observed in **Figure 43**.

Statistic analyses about the main effects highlight that for SDAS results, the Cr increase and the re-melting increase have an effect (see **Figure 44**).

Notably, from the literature, the increase in Cr amount led to a decrease in SDAS value [128]. This behaviour was here partially demonstrated despite the counteracting effect of the re-melting act increasing the SDAS size [129].

The same considerations can be drawn about the micro-hardness measures, as in **Figure 45**.

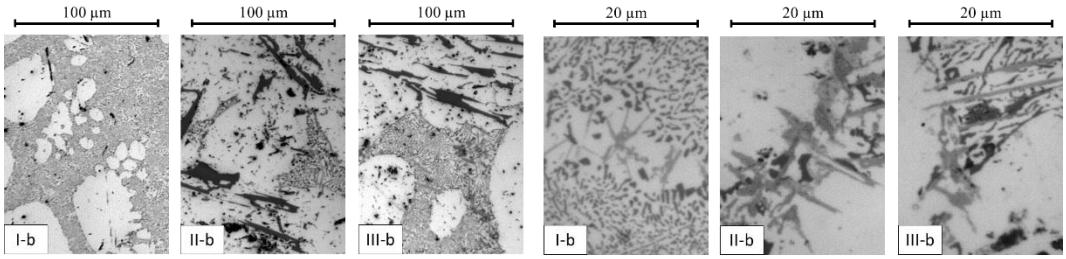

Figure 42. Upper images: details of eutectic silicon change during re-melting of AlSi7Cu0.5Mg plus 1 wt% Cr. Lower images: details of intermetallic phase change during progressive re-melting of AlSi7Cu0.5Mg plus 1 wt% Cr

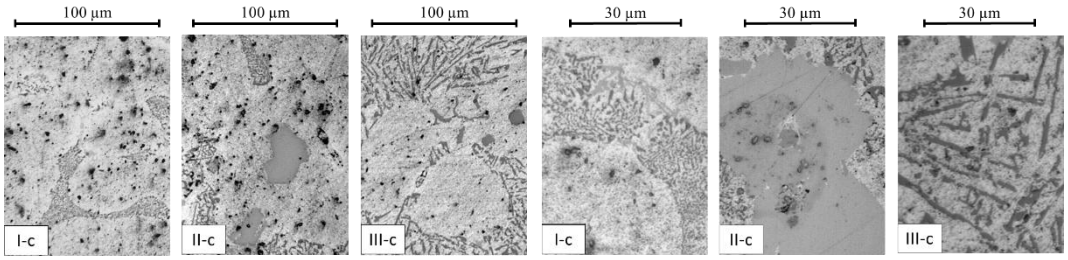

Figure 43. Upper images: details of eutectic silicon change during re-melting of AlSi7Cu0.5Mg plus 1 wt% Cr. Lower images: details of intermetallic phase change during progressive re-melting of AlSi7Cu0.5Mg plus 1 wt% Cr

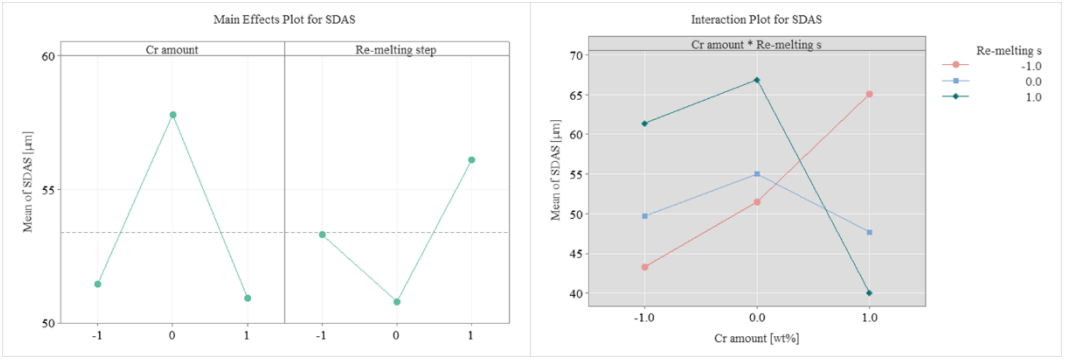

Figure 44. Main effect calculated by Minitab. Effect of Cr amount and Re-melting on SDAS. Cr: -1 indicates no Cr, 0 indicates 1 wt% Cr, 1 indicates 2 wt%

Cr. Re-melt: -1 indicates first re-melt, 0 indicates the second re-melt and 1 indicates the third re-melt.

Results highlight that casting can be successfully performed through scrap alloy AlSi7Cu0.5Mg with 1 wt% of Cr or without Cr, retaining the microstructure of α-Al and refined eutectic, while the addition of 2 wt% Cr leads to obtaining both refined and coarse eutectic microstructures.

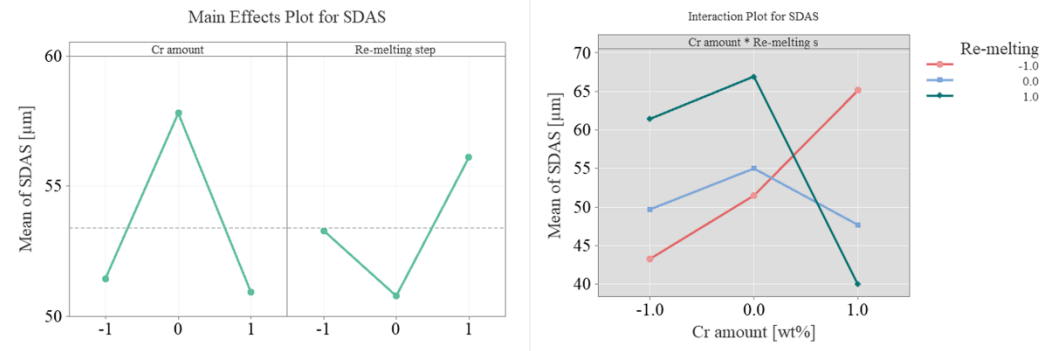

Figure 45. Main effect calculated by Minitab. Effect of Cr amount and Re-melting on Eutectic micro-hardness. Cr: -1 indicates no Cr, 0 indicates 1 wt% Cr, 1 indicates 2 wt% Cr. Re-melt: -1 indicates first re-melt, 0 indicates the second re-melt and 1 indicates the third re-melt.

These results stimulated further work focusing on the effect of scrap material content on the mechanical results achievable (4.2.3). In previous chapters, the mechanical properties of samples with variable amounts of scrap alloy were shown. In this perspective, to understand the main effect of the scrap alloy on main mechanical properties appears crucial the statistic evaluation of results. The microstructural features of such specimens are already shown in **Figure 34** and **Figure 35**. In statistical evaluation, in this specific case, the main factor is only one, the scrap amount. In this sense, a probability plot can be drawn to highlight the data dispersal. Starting from the probability plot for micro-hardness (**Figure 46**), a higher data dispersion can be noticed in samples type A and B since the slope of the line in the graph corresponds to the dispersion of the data. Such behaviour was further highlighted in the box plot and dot plot of **Figure 36**.

Figure 47 shows the probability plots for elongation at rupture A%, ultimate tensile strength Rm and yield strength Rp0.2. From the probability plot, it appears that there is no sample type with low data deviation in all measured mechanical properties. Results in terms of Rm and Rp0.2 are slightly higher in A-type than in E-type, while A% resulted higher in samples type C, where the composition is half ingot alloy and half scrap alloy. In **Figure 48**, the probability plot for impact test results is shown. As a lower slope means less data dispersion, samples A, C, and E showed a lower slope and low standard deviation. Conversely, B specimens resulted in worst results and high data dispersion, as already highlighted by the dot plot and box plot in **Figure 39**.

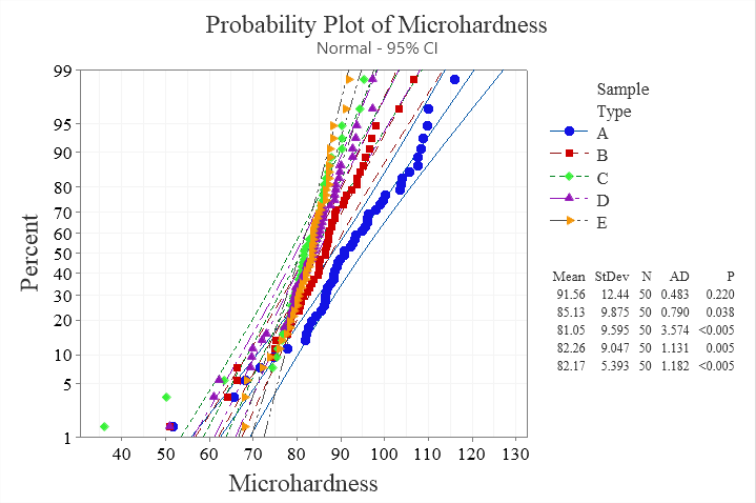

Figure 46. Probability plot for micro-hardness

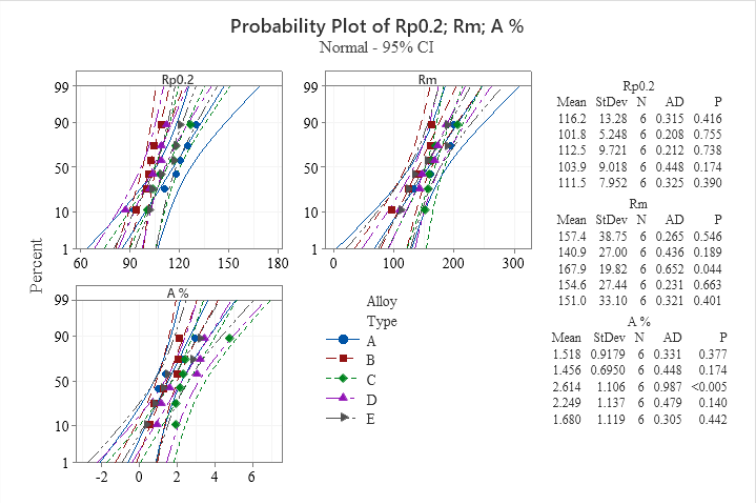

Figure 47. Probability plots for tensile properties

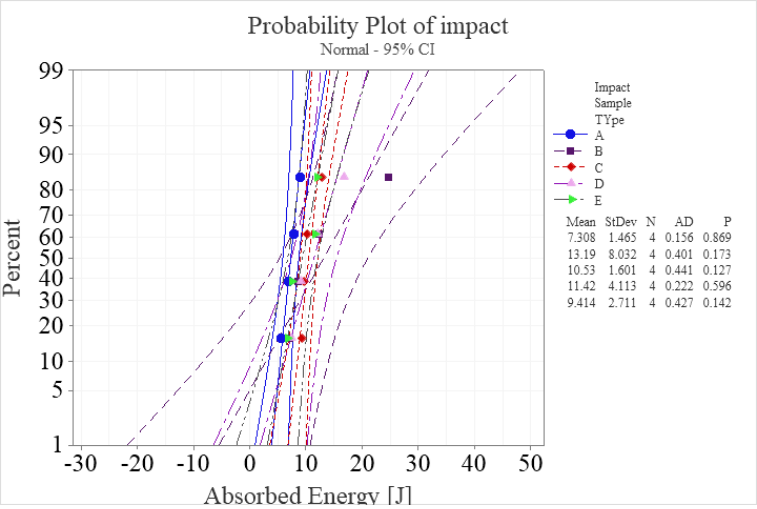

Figure 48. Probability plots for absorbed energy (impact tests)

Mainly, uniaxial tensile test results appear similar in samples A (100% ingot alloy) and sample E (100% scrap alloy). This behaviour can be associated with remelting test results: alloy AlSi7Cu0.5Mg continue to show good microstructural features after the re-melt, confirming the possibility of casting components through scrap alloy.

Chapter 5

5 Recycling AlSi9Cu3(Fe) by GC

In this chapter, the feedstock properties of the ingot and scrap alloys AlSi9Cu3(Fe) have been shown, along with the recycling routes selected and the results obtained.

The recyclability protocol detailed in section 2.5 was applied to scrap alloy AlSi9Cu3(Fe). Tests gave positive results in terms of castability, while a large amount of internal porosities were detected. Re-melting and gravity casting of the alloy were performed to evaluate the feasibility through the recyclability protocol. Those tests were conducted using only scrap alloy. Unlike what happens with alloy AlSi7Cu0.5Mg, alloy AlSi9Cu3(Fe), at the present time, is studied in terms of re-melt with the aim to cast components starting from a scrap-based feedstock, thus reducing the carbon footprint of the casting process.

In this context, the cast samples are brick-shaped, and the aim was to check the microstructure and a few mechanical properties after the addition of Ni and/or Cr. The choice of Cr and Ni has been discussed previously in 2.3.1 and 2.3.4: Cr tend to form intermetallic phases with Fe and Mn, while Ni tend to form intermetallic phases Al-Cu-Ni. Compared to the mechanical characterisations carried out on the AlSi7Cu0.5Mg alloy, wear tests were performed. This was essentially due to the fact that the AlSi9Cu3(Fe) specimens exhibit greater porosity defects, which would have excessively influenced the mechanical characterisations by uniaxial tension.

Such tests aim to evidence the possibility of casting components only using new scraps.

This chapter is based on:

Elisa Fracchia; Marco Actis Grande. "Effetto dell'aggiunta di Cr e Ni sulla microstruttura e la resistenza a usura della lega riciclata AlSi9Cu3(Fe)". In Raccolta degli atti del 40° Convegno Nazionale AIM, ISBN 978-88-898990-39.

5.1 Materials and Methods

5.1.1 Alloy feedstock and casting process

In **Table 23**, ingot and scrap AlSi9Cu3(Fe) alloy compositions were reported.

The feedstock materials (**Figure 49**), in the form of scraps and ingot, were sectioned, and samples for metallographic analyses were prepared to check the microstructures, the hardness and the chemical composition. After the composition assessment, the alloys were melted using an electric furnace and were cast into a steel mould to obtain samples for metallographic analyses and mechanical tests.

Metallic Cr and metallic Ni were added in powder form, to facilitate their melt and diffusion into the aluminium bath (Metalpolveri S.r.l., Cr 400 mesh and Ni 100-325 mesh). Metallic Cr details are shown in **Table 17**, while the chemical composition and particle size of Ni metallic powder are reported in **Table 24.**

Table 23. AlSi9Cu3(Fe) compositions provided by Teksid S.p.A.

AlSi9Cu3(Fe) INGOT								
	Si	*Fe*	*Cu*	*Mn*	*Mg*	*Zn*	*Ti*	*Al*
wt%	10.27	1.07	2.91	0.23	0.25	1.49	0.04	Bal.
AlSi9Cu3(Fe) SCRAP								
	Si	*Fe*	*Cu*	*Mn*	*Mg*	*Zn*	*Ti*	*Al*
wt%	10.10	1.10	3.21	0.27	0.33	1.15	0.04	Bal.

Gravity casting involves the melting of the scrap alloy in an electric furnace using a graphite crucible with a capacity of 1 kg, as previously detalied in 4.1.1. During the casting, additives (refiners, modifiers) were not inserted.

Table 25. Summarizes the type of castings performed and the Ni and Cr amount contained in each type.

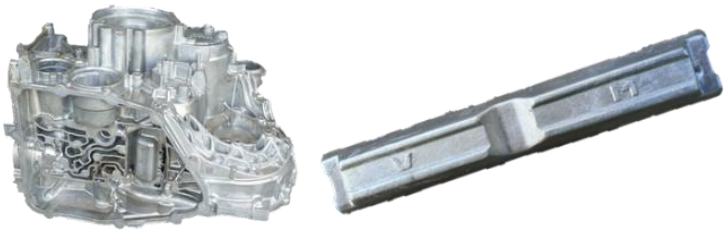

Figure 49. AlSi9Cu3(Fe) feedstock. Left side: scrap; right side: ingot

Table 24. Metallic Ni powder. Physical and chemical properties provided by the producer.

Granulometric size wt%					
< 250 µm	*< 180 µm*	*< 150 µm*	*< 106 µm*	*< 75 µm*	*< 45 µm*
100	98-100	95-99	73-89	22-43	1-11

Chemical composition wt%							
Co	*C*	*Fe*	*S*	*Cu*	*Zn*	*Pb*	*Ni*
0.08-0.03	0.01-0.001	0.02-0.01	0.03-0.01	0.01-0.001	0.01-0.001	0.01-0.001	99.90-99.99

Table 25. Castings compositions

Sample's name	**Samples type**	**Description**
1	AlSi0Cu3(Fe)_0.5Cr_0.5Ni	0.5 wt% Cr and 0.5 wt% Ni
2	AlSi0Cu3(Fe)_1Cr_1Ni	1 wt% Cr and 1 wt% Ni
3	AlSi0Cu3(Fe)_1Cr	1 wt% Cr
4	AlSi0Cu3(Fe)_0.5Cr	0.5 wt% Cr
5	AlSi0Cu3(Fe)_0.5Ni	0.5 wt% Ni
6	AlSi0Cu3(Fe)_1Ni	1 wt% Ni

5.1.2 Microstructural characterizations

Microstructures were characterized in all cast specimens. The microstructural characterization procedure is conducted using both Optical Microscope (OM - Leica Microsystems MEF4M) and Scanning Electron Microscope equipped with an EDS probe (SEM Zeiss EVO 15 and Oxfor Ultim Max 40 probe) to analyse semi-quantitatively the intermetallic phases. SEM-EDS analyses were used to characterize the intermetallic phases in the specimens. Moreover, wear surfaces can be observed after pin-on-disk tests (post-mortem characterization) to get further information about the mechanical properties. Specimens for OM and SEM-EDS must be polished as previously explained in 4.1.2. **Table 26** detailed the recyclability procedures through Gravity Casting.

Table 26. Recyclability Protocol and tests on AlSi9Cu3(Fe) alloy

Recyclability Protocol		
Characterization	*Details*	*Instruments*
Feedstock characterization	Dross test Straube Pfeiffer test Microstructural analyses	SEM-EDS Optical Microscope DSC
Characterization	*Details*	*Instruments*
Gravity Casting and cast characterization	Type 1 samples Cast of samples with and without element additions (Cr, Ni)	SEM-EDS Optical Microscope Wear test Micro-hardness
Post-mortem characterization	Analyses of wear samples	SEM

5.1.3 Mechanical tests

Microhardness was characterized on a Vickers and Knoop microdurometer Leica Type VMHT through microvickers indenter by applying 50 g of load for 15 seconds.

Further specimens were machined to obtain mechanical samples to perform pin-on-disk tests (2 samples for each condition), similarly to [130]. Samples were machined at 25 mm in diameter and 10 mm in thickness, while test conditions were 60 rpm, load 5 N, total distance 100 m, working diameter 16 mm, using a WC pin of 3 mm as tip diameter.

After the wear tests, the wear rate can be obtained from the wear coefficient f, the sample's density and the sample's weight, using (4):

$$\text{Wear Rate } \left(\frac{\text{mm}^3}{\text{m}\cdot\text{N}}\right) = \frac{\text{Weight lost (g)}}{\text{Density } \left(\frac{\text{g}}{\text{cm}^3}\right)\cdot\text{Load (N)}\cdot\text{Distance (m)}} \quad (4)$$

5.2 Results

5.2.1 Microstructural characterizations: scrap AlSi9Cu3(Fe)

AlSi9Cu3(Fe) is mainly characterized by α-Al matrix, the eutectic silicon and intermetallic phases. Copper addition permits the nucleation of θ-Al_2Cu intermetallic and the Q-phase Q-$Al_5Cu_2Mg_8Si_6$, while the Fe and Mn leads to the nucleation of π-Al8Mg3FeSi6, α-Al(Fe, Mn)Si and β-AlFeSi phases. The noticed intermetallic phases are shown in **Figure 50**.

The critical amount of Fe, critical temperature and sludge factor were evaluated through formulae of paragraph 2.4:

Sludge Factor (SF)= 1.53 (ingot) / 1.64 (scrap)

Fe_{cr} = 0.72 (ingot) / 0.705 (scrap)

Temperature (°C) = 684.56 °C (ingot) / 687.08 °C (scrap)

These results mean that for ingot alloy, the critical iron content is about 0.72 wt% (the ingot alloy contains 1.07 wt% Fe) and at temperatures higher than 685 °C,

the possibility of nucleation of harmful Fe-intermetallic rapidly increases. The Silicon amount affects the time and temperature of the nucleation of the β-Fe phase. The higher the Silicon content, the lower the temperature and times required to form the β-Fe phase, and the higher the acceptable iron content. Considering the amount of iron and silicon calculated, the critical iron content resulted in 0,71 wt%. As in this alloy, the iron amount is higher than 1 wt%, a large amount of detrimental β-Al_5FeSi phases is expected.

Similarly, for scrap alloy, the critical iron content is about 0.705 wt%, while the alloy contains 1.1 wt% Fe. This means that at temperatures greater than 687 °C, the nucleation of harmful Fe intermetallic phases strongly increases.

Regarding sludge factors, the alloys present sludge factors of about 1.5 and 1.6, respectively. The sludge factor must be minor than 1.4 to avoid sludge in the holding furnace at about 620 °C and minor than 2 to avoid sludge at 660°C, as in **Figure 51**.

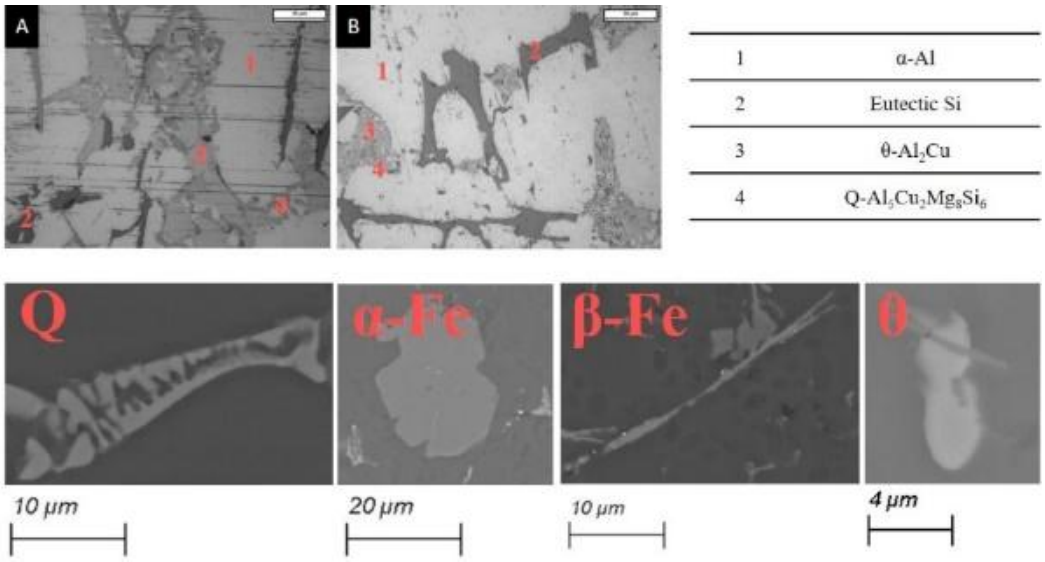

Figure 50. Optical microscope images, magnification 500 X (marker 30 µm). A: ingot AlSi9Cu3(Fe); B: scrap AlSi9Cu3(Fe). On the bottom side, details of intermetallic phases observed by SEM

Intermetallic phases shown in **Figure 50** were partially observed even through DSC analyses.

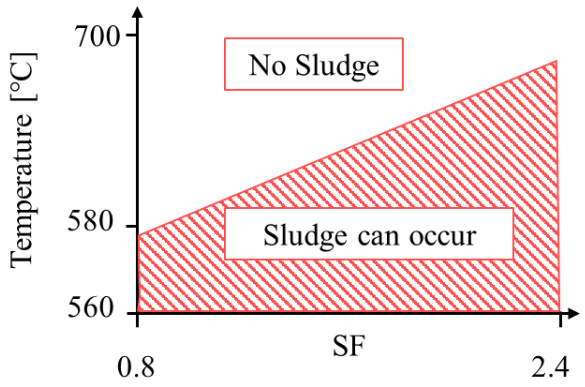

Figure 51. Qualitative scheme of Sludge Factor SF versus melt temperature. Adapted from [134].

Figure 52 shows micrographs about dross test samples. Mainly, sludge particles appears larger in scrap alloy, as attended from the sluge factor previously measured.

Thermograms of scrap and ingot alloys are shown in **Figure 53**, while the detected phases are as follows: point 1 corresponds to the melting of the complex phase θ-Al_2Cu + β-$Al_5Cu_2Si_6$ [131] or, more probably, to the dissolution of Mg_2Si and θ -Al_2Cu [132].

Point 2 from the literature corresponds to the α-β Eutectic melting: α-Al–Si–βAl9Fe2Si [131] while point 3 characterizes the precipitation of θ phase [133].

Castings performed (**Table 25**) were polished, and microstructures obtained by optical microscope are shown in **Figure 54**.

Large pores were mainly noticed after casting. Phase θ-Al_2Cu was noticed in all the specimens, along with Q-phase. The π-Fe phase was even observed.

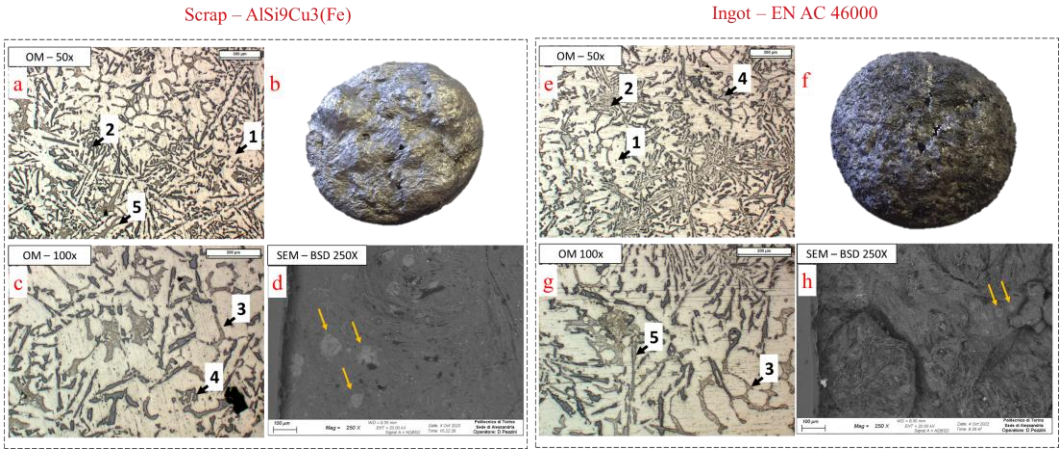

Figure 52. Dross test results – Scrap (left side) and ingot (right side) AlSi9Cu3(Fe) alloy. Numbers indicate different intermetallic phases. 1: α-Al; 2: Sieu; 3: Cu-containing phases; 4: Fe-containing phases; 5: β-Fe. Yellow arrows indicates sludge particles noticed on the dross test surfaces.

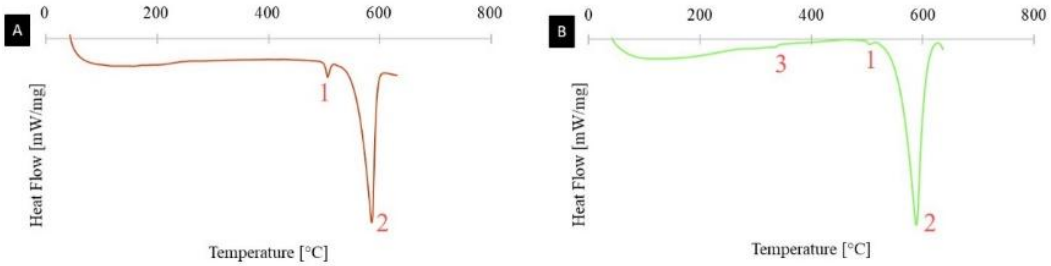

Figure 53. DSC. Heating curves in: A, ingot alloy AlSi9Cu3(Fe). B, scrap alloy AlSi9Cu3(Fe).

The α-Al dendritic matrix differs in the different samples, as the eutectic silicon (Si_{eu}) can appear inhomogeneous into the same cast from the point of view of the shape: it could be coarse-acicular, fine-acicular, or partially spheroidized.

SEM-EDS area analyses were performed to highlight the intermetallic phases.

In **Figure 55**, the SEM-EDS analyses of alloy containing 0.5 wt% of Cr and 0.5 wt% of Ni are shown. It is possible to recognize two types of phases: the Ni-containing and the Cr-containing phases. Ni tends to form intermetallic phases with

Cu, while Cr tends to form large fishbone-type intermetallic phases with Fe and Mn.

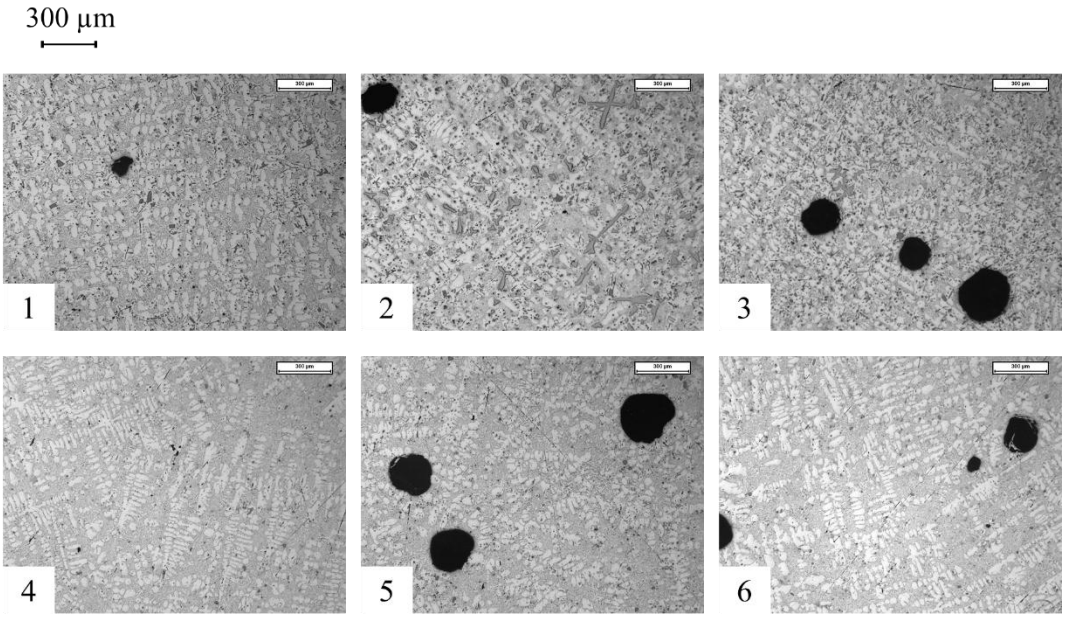

Figure 54. Microstructures (OM) of specimens based on AlSi9Cu3(Fe)

The addition of 0.5 wt% Cr leads to intermetallic phases type $Al_x(Fe, Mn, Cr, Cu)_ySi_z$, as discussed in 2.3.1. In analyzed points 8, 9 and 10 of **Figure 55**, x=13.04÷12.99, y= 3.39÷3.36 and z=2.

Moreover, 0.5 wt% Ni addition permits the nucleation of intermetallic compounds [135] AlCuNi, probably Al_3CuNi.

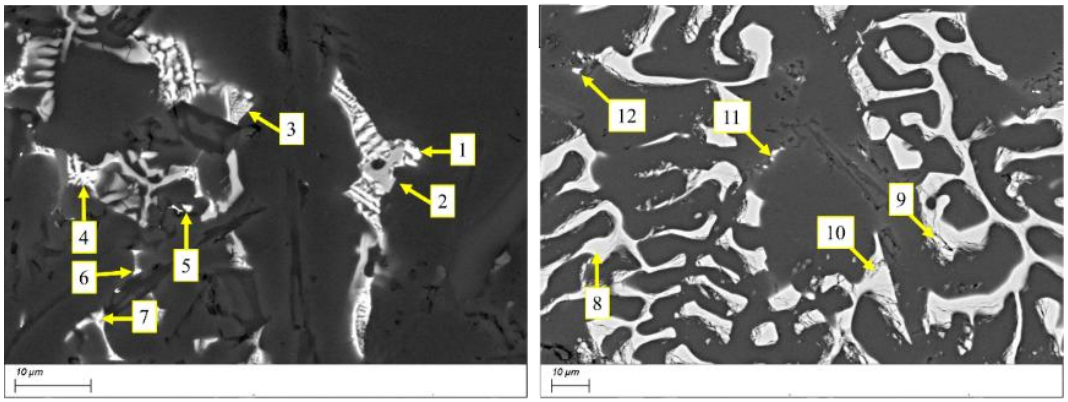

Points	Amount (wt%)											
	Al	Si	Cu	Fe	Mn	Cr	Mg	Zn	Ni	O	Sn	Pb
1	58.6	3.9	31.2	1			2.2	1.9	1.3			
2	62.2	7.4	9	15.3	3.4	0.3		1.3	1			
3	59.5	4.1	29.4	0.5			3.1	2.3	1.2			
4	57.4	2.2	28.5	0.4			1.5	2.6	1.1		1.2	5
5	42.7	25.6	1.5					0.9		5.2	0.8	23.2
6	39.2	27.2	9.4				1.1	1.2		1.8	1.3	18.8
7	66.4	8.9	20.8				0.8	1.9	1.1			
8	58.9	9.4	1.7	20.5	8.1	1.4						
9	58.7	9.8	1.9	20.4	8.1	1.2						
10	58.4	9.8	1.7	20.0	8.7	1.4						
11	89.4	4.5	4.0				0.6	1.4				
12	94.9	2.1	1.6				1.3					

Figure 55. Intermetallic phases in alloy AlSi9Cu3(Fe) type 1 - 0.5 wt% Cr and 0.5 wt% Ni

The addition of higher amounts of Cr and Ni lead to a drastic change in alloy microstructure (**Figure 56**).

Large star-like intermetallic phases were noticed: such phases can be characterized by very long branches up to hundreds of microns, as in specimen 2 in **Figure 54**. These phases $Al_x(Fe, Mn, Cr, Cu)_ySi_z$ are mainly characterized by x=11.9÷12.36, y=2.8÷3.03 and z=2. Intermetallic phases Pb/Sn-containing were also noticed [136]; these elements can be present in trace into the alloy composition since it is a secondary alloy. Pb and Sn can eventually, if present, be noticed in Q and Mg2Si phase since they have the capability to partially substitute the Si in such phases [137].

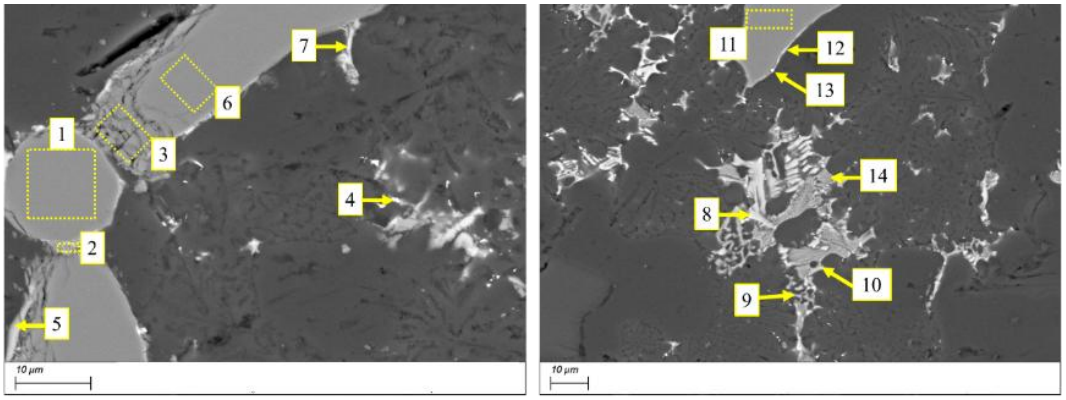

Points	Al	Si	Cu	Fe	Mn	Cr	Mg	Zn	Ni	Pb
1	60.6	10.6		15.4	5.7	7.7				
2	66.0	5.3	18.5	3.1	1.1	1.2	2	1.8	1.1	
3	60.1	10.5	1.3	15.6	5.3	7.1				
4	53.4	12.7	4.7	0.6			0.8	1.4		26.3
5	80.8	1.6	15.3	0.4				1.2	0.6	
6	60.0	10.1	0.6	15.5	5.9	7.9				
7	66.3	3.7	24.9	0.5			1.8	1.1	1.8	
8	55.2	1.6	39.2	0.4			0.6	0.8	2.1	
9	60.0	4.3	28.0	0.5			3.2	2.9	1.1	
10	67.5	3.5	22.1	0.3			2.1	3.6	0.9	
11	60.7	10.3	0.5	15.4	5.8	7.2				
12	61.2	9.2	4.4	15.7	5.7	3.9				
13	62.2	8.8	5.0	12.9	4.7	2.8	1.3			2.3
14	61.3	3.1	30.1	0.6			1.4	2.0	1.4	

Figure 56. Intermetallic phases in alloy AlSi9Cu3(Fe) type 2 - 1 wt% Cr and 1 wt% Ni

The 1 wt% Ni addition leads to the nucleation of the fishbone phase Al_3CuNi; in particular, in the analyzed point of **Figure 56** (points 7, 8, 9, 10, 14), a certain amount of other elements such as Si and Fe were noticed. From the literature [135], this behaviour is attributable to another phase particle near the analyzed point, for instance, Q-phase, or to the dissolution of a few atoms of Mg, Si and Fe into the AlCuNi phase.

From the microstructure observation, along with the presence of Zn, it seems that the analyzed AlCuNi phases nucleated near the Q phase [138].

In type 3 alloy (**Figure 57**), only the 1 wt% Cr was added to the alloy AlSi9Cu3(Fe). This addition leads to the nucleation of polygonal-shaped [10]

intermetallic phases Al(Fe,Mn,Cr)Si. These polygonal phases are characterized by the phases $Al_x(Fe, Mn, Cr, Cu)_ySi_z$ where x=12.83÷13.4, y=3.09÷3.23 and z=2.

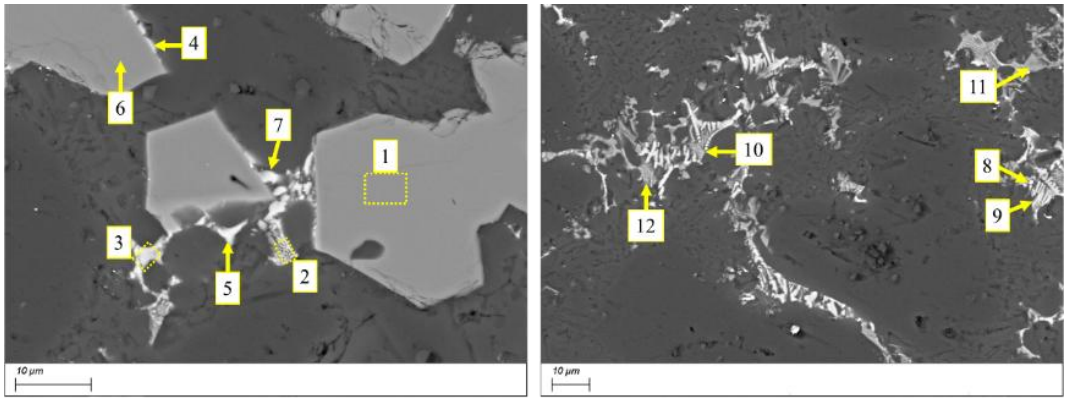

Points	Al	Si	Cu	Fe	Mn	Cr	Mg	Zn	Ni
1	60.7	9.4	1.0	16.9	7.2	4.8			
2	70.3	3.6	22.6				1.9	1.6	
3	58.2	2.4	34.7	0.6			1.3	1.3	1.4
4	61.5	7.3	10.0	12.8	5.2	3.1			
5	62.3	2.4	31.7	1.0			1.8	0.8	
6	60.4	9.8	1.1	17.2	6.9	4.6			
7	55.7	8.0	28.6	4.1	0.8	0.4	1.1		1.3
8	67.1	6.8	18.0	2.5			3.9	1.7	
9	84.4	1.2	11.7				0.7	2.0	
10	58.0	4.2	30.6	0.3			3.8	2.2	0.8
11	66.3	7.9	7.4	13.7	2.4	0.8		1.4	
12	60.4	5.2	27.1	0.3			4.3	1.7	1.0

Figure 57. Intermetallic phases in alloy AlSi9Cu3(Fe) type 3 - 1 wt% Cr

A certain amount of intermetallic phases Al-Cu-Ni fishbone shaped was noticed, probably caused by a certain amount of Ni in the scrap alloy. The nucleation of the Q-phase was noticed near the polygonal α-Fe phases, along with the π-Fe phase (points 4 and 5 in **Figure 57**).

After the addition of 0.5 wt% Cr, no polygonal-shaped phases were noticed. Conversely, α-Fe phases with a star-like form were observed (**Figure 58**). The α-Fe phase dimension appears smaller. Furthermore, the alloy appears mainly characterized by the π-Fe phase and the α-Fe Cr-containing phases are limited in amount. As already noticed, a certain amount of Ni was observed in fishbone-like Cu phases, while a certain amount of Sn was retained in the Q phase (point 6, **Figure 58**).

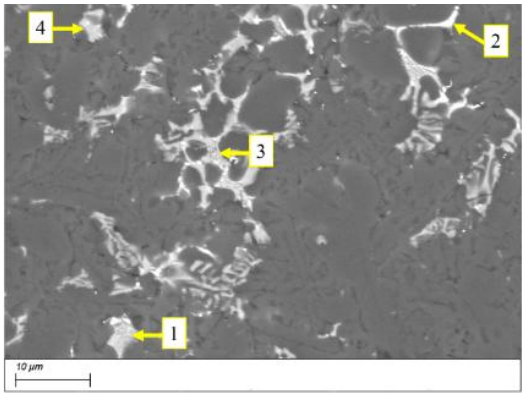

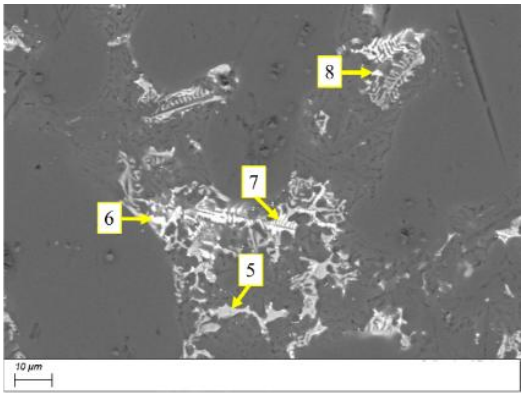

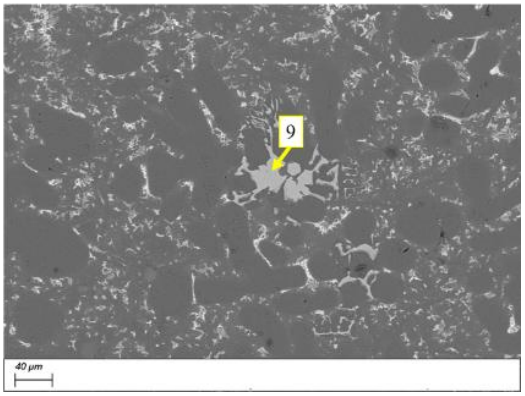

Points	Al	Si	Cu	Fe	Mn	Cr	Mg	Zn	Ni	Sn
1	74.6	3.4	19	0.2				1.4	0.5	
2	76.4	4.6	14.5	0.5			2.0	2.1		
3	65.4	4.0	27.1	0.8				2.1	0.6	
4	71.7	8.6	6.9	9.7	2.0			1.0		
5	62.7	5.0	29.1	0.4				2.2	0.6	
6	49.8	3.1	41.6				0.4	1.7	0.9	2.6
7	52.7	2.7	40.2	0.4			2.2	1.2	0.6	
8	60.0	4.9	31.0				1.3	2.0	0.8	
9	59.8	9.3	1.4	19.6	8.3	1.4				

Figure 58. Intermetallic phases in alloy AlSi9Cu3(Fe) type 4 – 0.5 wt% Cr

In **Figure 59** shows the SEM-EDS analyses of AlSi9Cu3(Fe) alloy with 0.5 wt% of Ni addition. This sample is mainly characterized by the fishbone-like intermetallic phases of AlCuNi.

The α-Fe phases were noticed, as in analyzed points 5, 6, 7,8 and 10. The x, y and z parameters for such phase $Al_x(Fe,Mn,Cu)_ySi_z$ were not calculated since it appears there is a certain amount of other elements (Ni, Zn, Mg) were noticed because of other phase particles near the analyzed point.

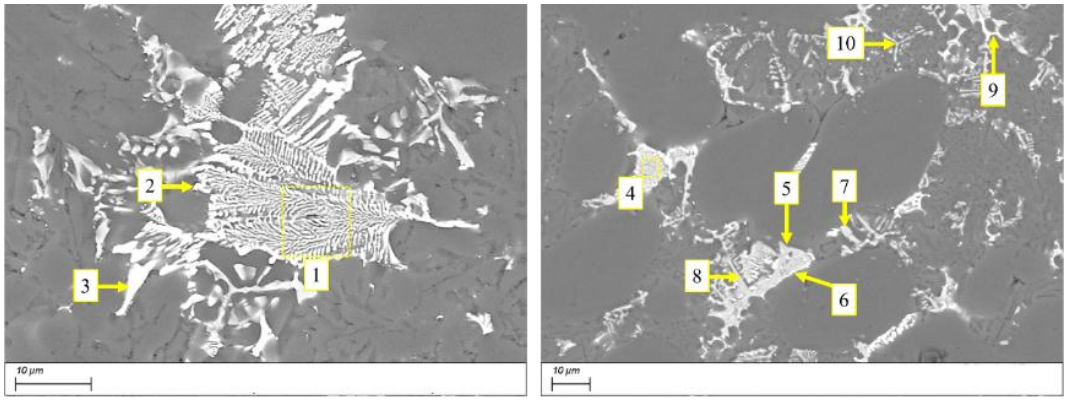

Points	Al	Si	Cu	Fe	Mn	Mg	Zn	Ni	Pb	O
1	62.0	4.5	24.9	0.6		4.1	2.1	1.8		
2	59.9	30.7	4.5			0.5	1.7		2.7	
3	60.6	3.7	28.6	0.4		3.4	1.8	1.5		
4	57.6	4.3	30.2	0.5		3.6	2.3	1.3		
5	72.7	6.6	5.6	10.2	2.8		1.5	0.7		
6	57.4	6.0	22.7	5.4	1.2	3.7	1.9	1.7		
7	63.3	9.1	5.8	15.1	4.5		1.1	1.1		
8	70.2	5.2	5.5	12.1	3.4		1.0	0.8		1.8
9	64.3	2.6	28.6	0.4		0.7	1.8	1.5		
10	82.6	3.5	4.2	6.0	1.6		1.5	0.5		

Figure 59. Intermetallic phases in alloy AlSi9Cu3(Fe) type 5 – 0.5 wt% Ni

Alloy type 6 is shown in **Figure 60**. In this sample, the α-Fe phases appear very extended, while was noticed the fishbone-like AlCuNi phase.

A certain amount of Pb and Sn were noticed and appeared to substitute the Si in the Q-phase.

The extent of α-Fe phase, in contrast with specimen type 2 (**Figure 56**), was not clearly noticeable from the optical microscope images (**Figure 54**) and appears to be limited in certain areas of the specimen. A certain amount of Cr was noticed, and x, y and z parameters of the phase $Al_x(Fe,Mn,Cu)_ySi_z$ are x=12.9÷13, y= 2.3÷2.4 and Z=2.

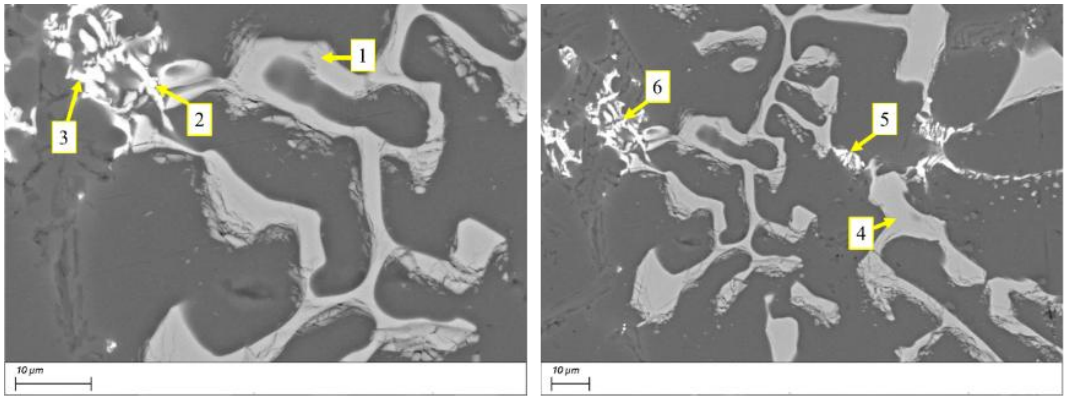

Points	Al	Si	Cu	Fe	Mn	Cr	Mg	Zn	Ni	O	Sn	Pb
1	60.3	9.7	1.9	19.3	7.7	1.1						
2	52.7	3.0	33.3	1.0			1.4	1.2	2.0			5.4
3	66.3	1.5	26.2	0.4			1.2	1.2	1.5	1.0	0.7	
4	59.7	9.5	1.8	19.9	7.9	1.2						
5	49.9	5.2	20.4	1.6			1.3	1.9	1.3		5.0	13.4
6	65.1	2.6	24.6	0.6			1.8	3.7	1.5			

Figure 60. Intermetallic phases in alloy AlSi9Cu3(Fe) type 6 – 1 wt% Ni

The addition of Cr and Ni affected the SDAS values. **Figure 61** shows the average SDAS values measured in all six alloy compositions. Box plots and dot plots highlight a certain data dispersion for specimens 1, 2 and 3, while specimens alloyed with Ni show a lower SDAS value, along with sample 4 having 0.5 wt% Cr. In the literature, it was reported that Cr and Ni addition in Al-Si alloys reduce SDAS values [128,139]. Nevertheless, it was reported from the literature that there was an increase in SDAS values with increasing porosities[140]. From this perspective, large porosities were noticed in specimens 3 and 5, which, in turn, showed higher values of SDAS than specimens 4 and 6, respectively. To better understand this behaviour, the samples' densities were evaluated through the principle of Archimedes (**Table 27**). It is reported that β-Fe phase and π-Fe phases are active in restricting the flow of the molten metal and causing shrinkage porosities, while α-Fe phases are less active in this sense [140].

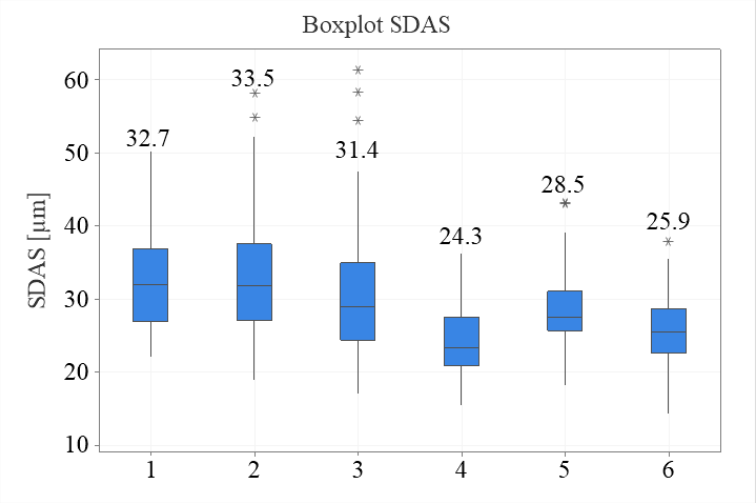

Figure 61. SDAS results in box plot

Table 27. Measured densities

Sample	Density [g/cm^3]	Sample	Density [g/cm^3]
1	2.68	*2*	2.70
3	2.55	*4*	2.64
5	2.68	*6*	2.67

5.2.1.1 Microhardness results and statistic

Microhardness statistical values (average, standard deviations, quartiles) were calculated through the MiniTab, and the results are graphically shown in **Figure 62**.

As α-Al regards, data appears non-uniform. Sample 3 shows a higher micro-hardness value, while other specimens show similar average results and, in particular, sample 1 shows higher α-Al homogeneity. Such a higher micro-hardness value may be attributable to the nucleation of fine particles of Al_7Cr distributed into

the α-Al matrix [141,142]. In fact, by comparing the α-Fe intermetallic phases, it is possible to notice less amount of Cr in alloy 2 phases, despite the same amount of chromium metal being added into the two alloys. Moreover, the absence of Ni in the alloy led to the nucleation of Guinier Preston θ-Al_2Cu zones homogeneously dispersed into the Al matrix.

As eutectic regards, sample 6 shows higher micro-hardness values, dramatically different from other specimens.

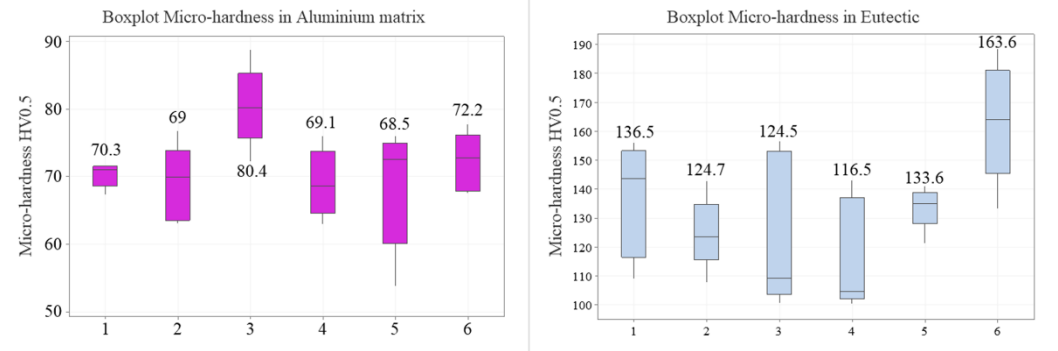

Figure 62. Box plot of micro-hardness measures: (left side: α-Al results, right side: eutectic results).

Conversely, only eutectic Si and small intermetallic compounds were indented in the eutectic regions. In such a case, since Ni tend to form intermetallic phases through Cu. Particularly, the Ni-containing phases are Al_3CuNi and Al_7Cu_4Ni if Ni content is lower than 0.3 wt%, while if Ni content exceeds 0.3 wt%, the typical intermetallic phase is Al_7Cu_4Ni [143] can be noticed. These nucleations lead to a certain amount of Cu consumption, which leads to less presence of the Guinier Preston θ-Al_2Cu phase. That normally acts to strengthen the α-Al matrix since they are thin disks shaped, with a diameter of about 3–5 nm. Homogeneously dispersed into the Al matrix [144].

5.2.1.2 Pin on disk results

Despite the low densities obtained for specimens, some mechanical tests, such as wear tests, can still be carried out. **Figure 63** shows the results for pin-on-disk

tests in the six alloys. In samples, Cr-containing are clearly visible the α-Fe phases in the alloy, out from the wear trace. Furthermore, fractures are evident on the wear surfaces, which mainly appear uneven in terms of wear.

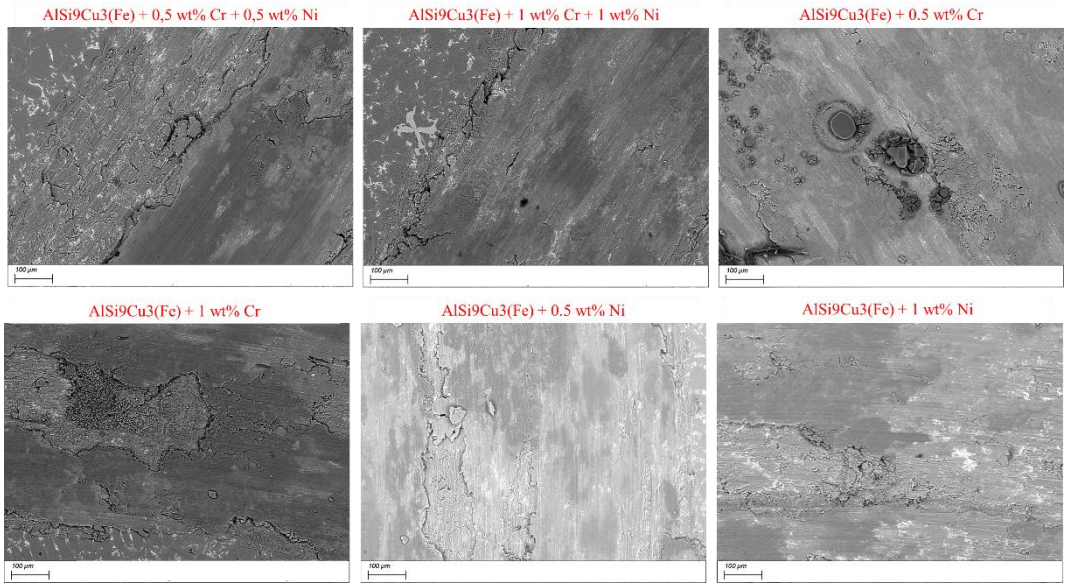

Figure 63. SEM images - samples' surfaces after pin-on-disk tests

The results in terms of wear coefficient COF and wear rate are shown in **Figure 64**. Samples Cr-containing are characterized by higher wear resistance, while specimens Ni-containing showed lower wear resistance. Specimens 1 and 2 that contain both Cr and Ni are characterized by an average wear rate value between the two conditions seen above. This behaviour may be attributable to the average micro-hardness of each specimen.

In **Figure 65**, some correlations are shown. In **Figure 65**-A, the relation between COF and wear rate was shown, highlighting that lower wear rates were noticed for Cr-containing specimens while the higher wear rate was measured for specimen 5. As for the COF vs eutectic micro-hardness relation (**Figure 65**-B), it was noticed that the Cr addition led to an increase in micro-hardness (**Figure 62**) that in turn led to an increase in average COF from 0.28 (0.5 wt% Cr) to 0.33 (1 wt% Cr).

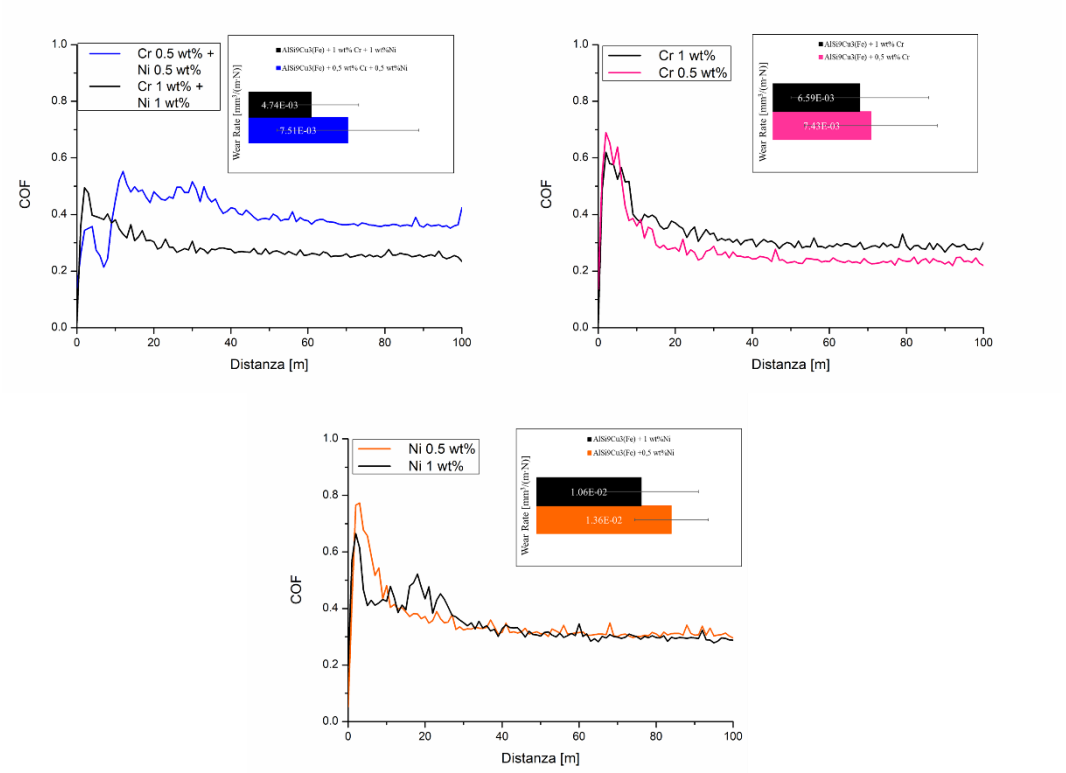

Figure 64. Average values of COF and wear rate.

A different behaviour was noticed in specimens Ni-containing (5 and 6). In this case, Ni addition leads to obtaining similar COF in the specimens (0.353 with 0.5 wt% Ni and 0.349 with 1 wt% Ni), although the average eutectic micro-hardness of specimens is markedly different between the two alloys: 133 HV0.5 in 0.5 wt% Ni sample (sample 5) and 163 HV0.5 with 1 wt% Ni (sample 6).

The addition of both Cr and Ni (samples type 1 and 2) leads to obtaining higher COF in the alloy characterized by higher eutectic micro-hardness.

The weight loss is directly related to the wear rate. On the other hand, no relation seems present between these two variables. This highlights that specimens characterized by high amount of pores, which in turn are characterized by lower density, were not apparently more prone to surface wear due to the presence of defects such as small pores and dendritic shrinkage.

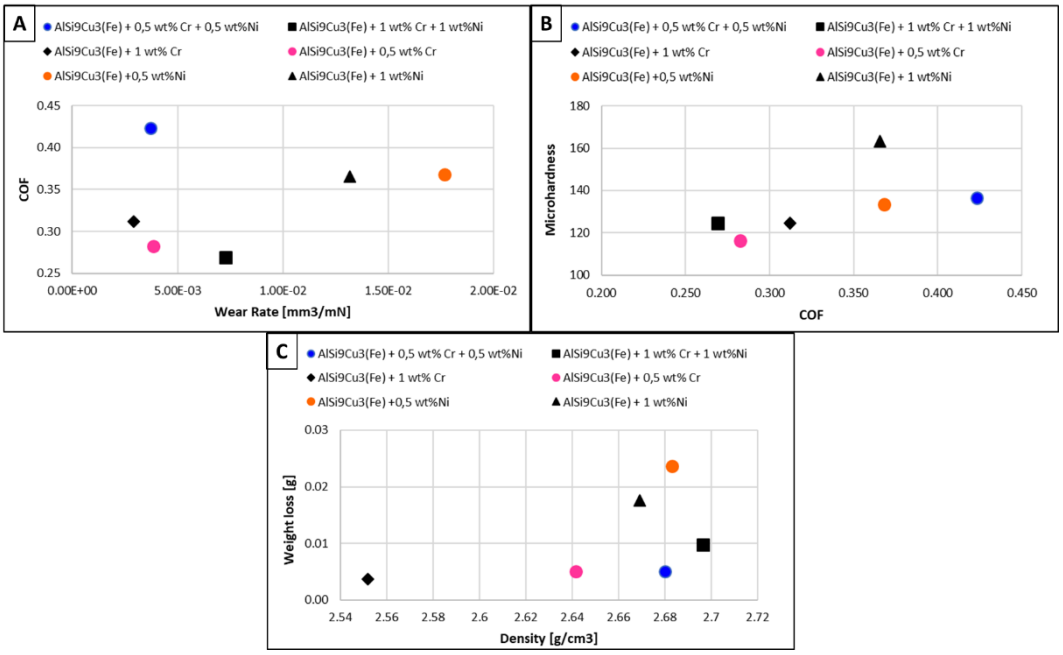

Figure 65. A: Wear rate vs COF, B: COF vs eutectic micro-hardness and C: specific weight vs lost weight.

5.3 Discussion

The characterization of alloy AlSi9Cu3(Fe) started from the castability tests on scraps. Since from the literature, the castability of such alloy was confirmed through re-melting by HPDC [12], while another research focused on the re-use of rejected castings in alloy AlSi9Cu3 [145] having an amount of almost 0.5 wt% Fe (less than half of the iron tenor of the alloy used in this work), here the addition of alloying elements was taken into account.

Tests performed mainly highlight an SDAS decrease with the addition of Cr or Ni if such elements are added separately (**Figure 61**). Nevertheless, porosities strongly affect the measured SDAS inside castings, despite from literature was noticed a SDAS decrease with Cr or Ni addition.

Gravity casting tests lead to not satisfactory results in terms of porosities: this behaviour was, on the other hand, explained by the presence of large intermetallic phases and sludge particles. Furthermore, the addition of metallic Cr and/ or metallic Ni leads to a strong increase in melting temperature to facilitate their dissolution. An increase in melting temperature leads to maintaining the alloy at

temperatures higher than the critical temperature, which, for the specific alloy used here, was calculated as 687 °C. At this temperature, following the indication in **Figure 51**, the nucleation of sludge particles appears possible; moreover, the critical amount of Fe resulted in about 0.7, a much lower value than the one that is actually contained in the alloy (**Table 23**). Re-melting with Cr and Ni addition, on the other hand, led to a change in intermetallic phases being detected. Furthermore, the eutectic silicon shape was affected by such a re-melting process **Figure 66**.

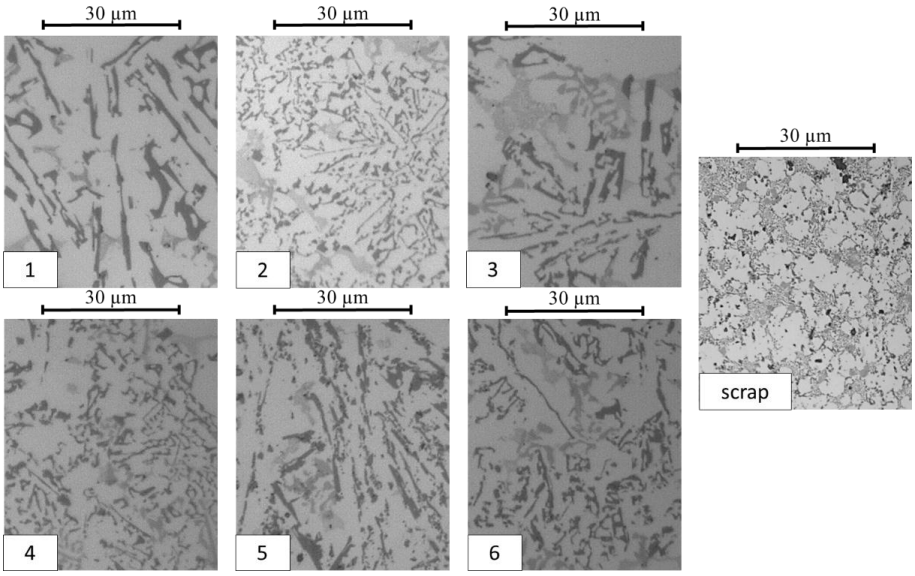

Figure 66. Details of eutectic region change during re-melting of AlSi9Cu3(Fe). Numbers indicates specimen types. Details of eutectic silicon in scrap component were reported.

In **Figure 67**, the main effects plots for SDAS and micro-hardness are shown as a function of the Cr or Ni amount. As plots do not show horizontal lines, it means that there is an interaction. As previously shown through SDAS and micro-hardness dot plot and box plot, Cr globally acts in reducing the eutectic micro-hardness since it forms a large intermetallic compound with Fe and Mn; on the other hand, the Ni addition appears to increase the micro-hardness in the eutectic area. As regards SDAS, Cr addition appears to increase the average SDAS, which in turn results in high porosities inside the casting. Conversely, the Ni addition up to 1 wt% leads to a decrease in the average SDAS.

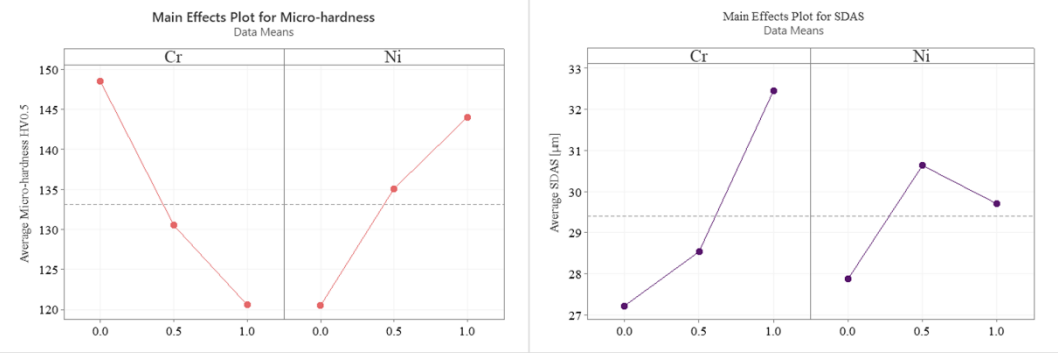

Figure 67. Main effect plots micro-hardness vs Cr/ Ni amount (left side) and SDAS vs Cr/ Ni amount (right side).

As pin-on-disk results, Figure 58 reports the main effects of Cr and Ni on wear rate and COF. The Cr addition reduces the wear rate and COF, while the Ni addition acts up to 0.5 wt%, increasing both the wear rate and the COF. If Ni is added up to 1 wt%, on the other hand, it leads to a decrease in both wear rate and COF, probably thanks to the nucleation of harder intermetallic phases.

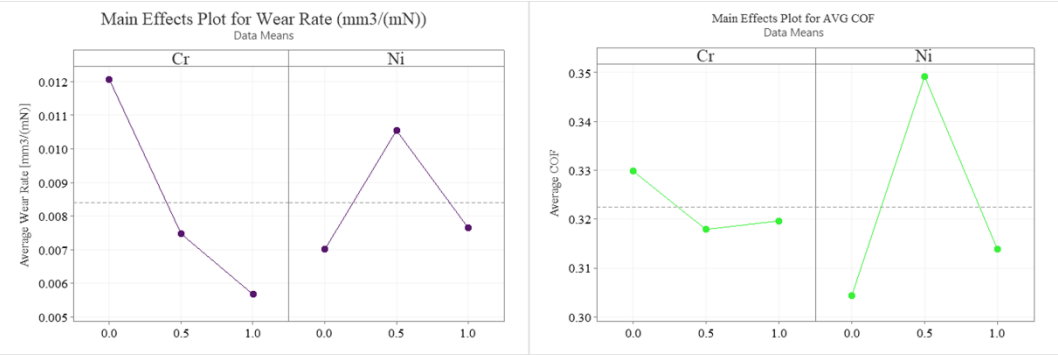

Figure 68. Main effect plots wear rate vs Cr/ Ni amount (left side) and COF vs Cr/ Ni amount (right side).

Despite the good mechanical properties results, the gravity casting procedure must be implemented to obtain specimens with a low amount of retained defects (gas pores, large sludge, shrinkage).

Chapter 6

6 Recycling AlSi9Cu3(Fe) by AM

This chapter is devoted to the recyclability of the alloy AlSi9Cu3(Fe) through additive manufacturing. The recycling was focused on the composition AlSi9Cu3(Fe). In this case, the recycling of the alloy was performed through the Additive Manufacturing route by Gas Atomization through the facilities available in the Additive Manufacturing laboratories of the Interdepartmental Center IAM, at the Alessandria Campus of Politecnico di Torino.

Starting from rejected castings (scraps) and ingot, the atomization procedure was carried out to produce fresh powder. After characterization, the powder was printed through the L-PBF process to realize the specimens.

Samples were subject to mechanical tests to assess the alloy printability and the sample's quality. Moreover, samples will tested in the as-built condition as well as after heat treatment T6.

The paragraphs highlight details about the powders' characterization route, selection of the L-PBF printing parameters and selection of the heat treatment parameters. Mechanical properties are evaluated and compared with results obtained by the state-of-the-art alloy for AM: AlSi10Mg.

6.1 Introduction

In alternative production methods such as additive manufacturing, aluminium has gained a strong popularity in recent years.

In 1.3, additive manufacturing was introduced as a possible way to recycle scrap materials. In this sense, for the present knowledge, only a few authors focused on scrap recycling.

In particular, in [146] authors recycled AM parts produced in AlSi10Mg alloy to produce new L-PBF specimens. Additive manufacturing specimens produced from scrap are characterized by lower yield strength than the AM part and almost half of the ultimate tensile strength. On the other hand, the ultimate tensile stress results are comparable to those of cast samples. Even the elongation at rupture is strongly reduced in AM scrap specimens.

In [147] authors summarize the use of recycled aluminium as feedstock in additive manufacturing. In particular, the recycling of powder was taken into account. The literature mainly focused on the recycling of AlSi10Mg powders.

Considering AlSi9Cu3(Fe), this alloy composition is not used in additive manufacturing at the present time. In particular, a similar composition of AlSi9Cu3 is used slightly, and some researchers have started studying this powder in L-PBF.

6.2 Materials and Methods

6.2.1 Alloy feedstock and atomization

In **Table 23**, ingot and scrap AlSi9Cu3(Fe) alloy compositions were reported. The feedstock materials for additive manufacturing are the same used for gravity casting (**Figure 49**); scraps and ingots were cut into smaller sections and placed into an alumina crucible of 1.25 l capacity; each atomization can load 4 kg of material. The alloy was heated under vacuum (8.3 10^{-3} mbar) while Argon was backfilled in the furnace at 400°C to cover the melt and remove any outgassed species. When the temperature reaches 850 °C, it will be equalized for 15 minutes, and then the induction furnace is further pressurized at 1.20 bar; then, the molten alloy is atomized at high velocity thanks to a De Laval nozzle with an inlet pressure

of 45 bar. After the atomization, the powder passivation is carried out to minimize the explosion behaviour of the fine powders.

Notably, after the atomization of the ingot alloy, a large amount of oxides was observed, along with a bluish patina covering the inner walls of the crucible and thick oxide skins at the crucible's bottom (**Figure 69**). Such a patina was easily removed but highlighted a different oxidation behaviour between scrap and ingot alloy, as primarily studied by the Dross Test in paragraph 2.5 and 5.2.1. After the atomization, the powder must be sieved in L-PBF size and then printed. After sieving, powders undergo various powder characterisations such as PSD evaluation, XRD and microstructural observations.

Figure 69. Bluish patina and oxide skins into the Alumina crucible after atomization of ingot AlSi9Cu3(Fe).

As powder batches regard, two batches for each type of alloy were produced. Starting from ingot alloy, an inlet pressure of 45 bar was used in the first atomization.

At the end of the first atomization, the powder's PSD resulted in quite large size, having a D_{10} of 17.9 µm, a D_{50} of 51.6 µm and a D_{90} of 146 µm. Such results indicated an yield lower than 50%. By the increasing of the pressure up to 50 bar, the powder PDS markedly change: a D_{10} of 13.4 µm, a D_{50} of 39.6 µm and a D_{90} of 96.3 µm. Such result indicates an higher yield.

Accordingly, the inlet pressure was mantained at 50 bar during the atomization of scrap alloy, obtaining very fine particles. The PSD of the two batches produced from scrap were: D_{10} of 12.2 µm, a D_{50} of 33.3 µm and a D_{90} of 67.3 µm. After the sieving, the amount of AlSi9Cu3(Fe) ingot powder (EN AC 46000) was 3.3 kg from two atomization, while AlSi9Cu3(Fe) scrap amount was 4.9 kg.

The PSD of the powders as-atomized are shown in **Figure 70**, while the powder batches are shown in **Figure 71**.

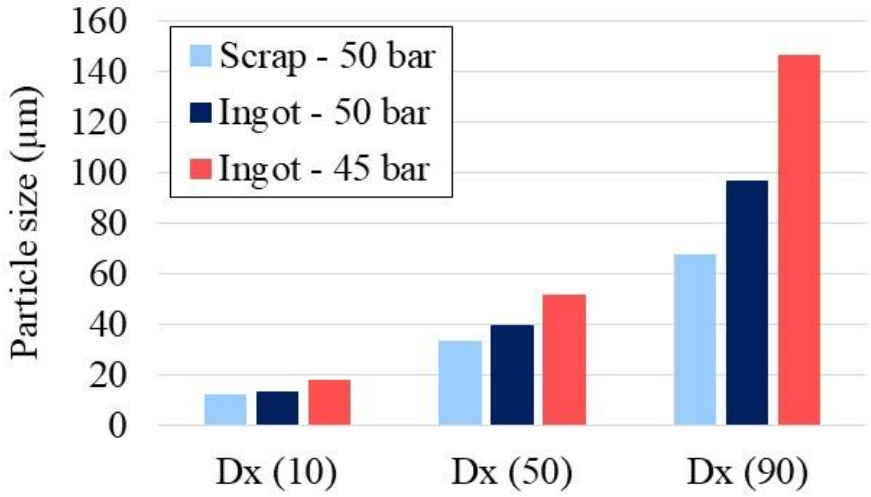

Figure 70. Main PSD size in first ingot and scrap powder atomization at different inlet pressures.

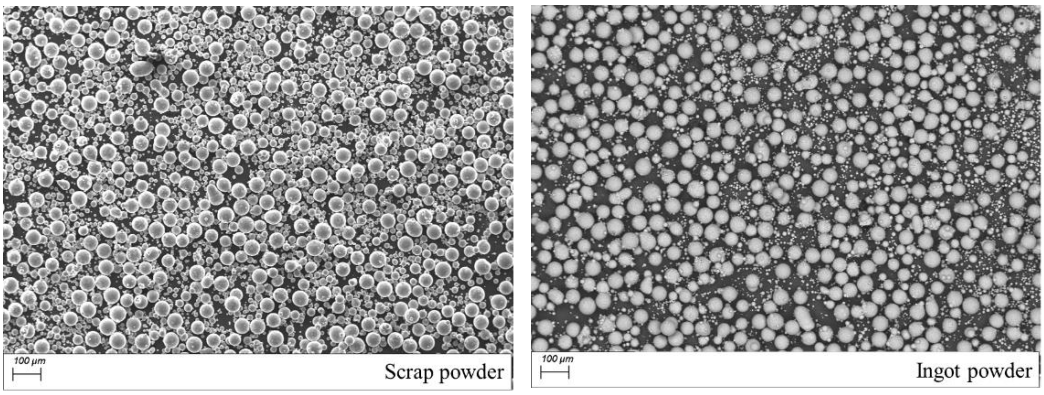

Figure 71. SEM-BSD images of the two alloy powder batches.

6.2.2 Powder characterizations

The evaluation of AM powder properties is crucial for material exploration, particularly in this specific case where the feedstock alloy is based on foundry alloys rich in Cu and Fe.

In this sense, specific evaluations, such as PSD, flowability, and XRD analyses, must be performed, as in [115], by following the Standard ISO/ASTM 52907:2019(E) and ATM F3049–14.

The microstructural characterization of powders is conducted by embedding powders into epoxy resin and using a Scanning Electron Microscope equipped with an EDS probe (SEM Zeiss EVO 15 and Oxfor Ultim Max 40 probe) to analyse semi-quantitatively the intermetallic phases. Specimens for SEM-EDS must be polished as previously explained in 4.1.2. Powders were subjected to DSC, rheology measures and XDR analyses.

X-ray diffraction (XRD) analyses were conducted on both powders using a diffractometer Empyrean (Malvern Panalytical, Malvern, United Kingdom) using the Bragg-Brentano geometry (CuKα, λ = 1.5406 Å radiation, scanning speed of 0.02º/min in 2θ = 20-140 deg. Range) to identify the intermetallic phases. Results were analyzed through X'Pert HighScore software (Malvern Panalytical, Malvern, United Kingdom).

The quantities of oxygen, nitrogen and hydrogen were assessed in both the bulk specimen and on the atomized powders using the elemental analysis LECO® (ONH836). This analysis provided insights into the oxygen, hydrogen and nitrogen contents at various particle sizes.

The rheological measurements were performed by a shear cell rheometer (Freemantech FT4) on powders in the 20 µm - 63 µm size range (Standards B331-0 and B527-23), while the flowability in 20 µm – 63 µm range, was measured according to standards ASTM B212-21 (Hall Flowmeter Funnel) and ASTM 964-23 (Carney Flowmeter Funnel). Before the flowability tests, powders were dried in a climatic chamber for 2 hours.

Picnometry (Anton Paar Picnometer) was performed in He atmosphere at room temperature to measure the true density of the powders, following the standard ASTM D3766.

6.2.3 L-PBF

Laser Powder Bed Fusion process was performed on AlSi9Cu3(Fe) sieved scrap and ingot powders in 20 µm - 63 µm size through a Renishaw AM125 machine, employing a pulsed Nd YAG laser with wavelength 1070 nm, maximum average power of 200 W and a spot size of 35 µm.

A parameter study was conducted on scrap alloy to select the optimal L-PBF printing parameters to obtain a higher density. In order to perform such a study, two sets of square samples 10×10×10 mm were printed by varying the process conditions, as in **Table 28**.

In the first process, the laser power and the hatch spacing were changed to select the best combination, while the other parameters were constant, as reported in **Table 28**. The scanning speed was set to a lower value with respect to AlSi9Cu3 literature, which appears to facilitate the process by reducing porosity, defects and displacements. Such setup was performed by printing 9 cubes of specimens with pins as sample support while the platform was set at 30 °C.

Table 28. L-PBF print parameters in AlSi9Cu3(Fe)

Parameters	First set of samples	Second set of samples
Laser power [W]	200/175/150	200
Layer thickness [µm]	30	30
Hatch spacing [µm]	100/90/80	80
Exposure Time [µs]	50	50/100/150
Point distance [µm]	140	40/60/80
Scanning speed [mm/s]	360	266.67÷1600
Atmosphere	Argon	Argon
Scanning strategy	Rotation 67°	Rotation 67°
Platform Temperature [°C]	30	30

6.2.4 Residual stress analysis

L-PBF samples were subjected to residual stress analyses to evaluate the effect of the printing process on the residual stresses.

X-ray analyses were conducted on L-PBF comparing the residual stresses of the component in the as-built condition, machined condition and heat-treated condition by a diffractometer X-ray Residual Stress Analyzer μ-X360s, equipped with a Cr X-ray target, by measuring the 2θ-shift of specific diffraction peaks: 2θ at 139,497° for (311) planes. Measurements were carried out by adopting a detector inclination of 25° and a distance between the sample surface and the detector of 39 mm. **Figure 72** depicts the analyzed points and the direction of analysis intended as the XRD apparatus orientation with respect to the specimen.

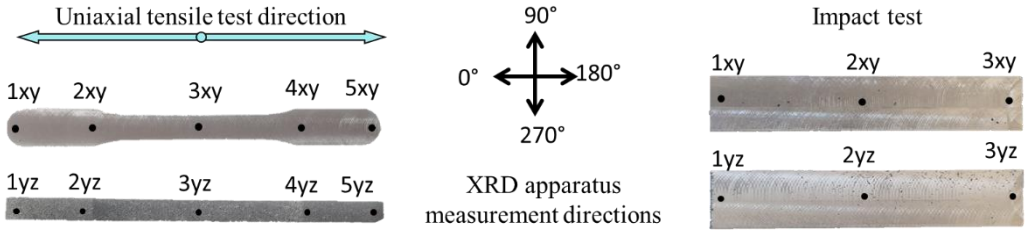

Figure 72. Residual stress analysis. Directions of analyses and analyzed points

6.2.5 Heat treatments

Heat treatments were performed in a static furnace Nabertherm in an air atmosphere on cube specimens. After the solubilization, specimens were quenched in room-temperature water and artificially aged. Treatments were performed following the recommendations of standard ISO/ASTM 52908:2023(E). After heat treatment, the micro-hardness of cubes was measured to evaluate the T6 treatment effects.

The heat treatments were selected as a function of the attended intermetallic phases. In the literature, it appears that the T6 heat treatments that can be performed on AlSi9Cu3(Fe) are mainly conducted at solution temperatures of 470 °C [97] or at about 520 °C [107]. At temperatures lower than 480 °C is expected to emphasize the θ-Al_2Cu phase dimension since its dissolution starts at about 480 °C; conversely, a solution treatment up to 515°C promotes the whole dissolution of θ-Al_2Cu [148].

Considering the literature, two sets of heat treatments were performed by changing the solution temperature and using an artificial ageing temperature of 165 °C.

- Solution at 470 °C 6 h, quench and artificial ageing at 160 °C for 6 h, 12 h, 18 h and 24 h. Even the natural ageing NA was considered;
- Solution at 515 °C 4 h, quench and artificial ageing at 160 °C for 6 h, 12 h, 18 h and 24 h. Even the natural ageing NA was considered.

The reference specimens in AlSi10Mg were treated T5:

- Artificial ageing at 160 °C for 6 hours.

6.2.6 Mechanical tests

Microhardness was characterized on a Vickers and Knoop microdurometer Leica Type VMHT through microvickers indenter by applying 50 g of load for 15 seconds (ASTM Standard F3122-14).

Specimens for tensile and impact tests were printed through L-PBF and tested at room temperature. Uniaxial tensile tests were performed on a 100 kN Zwick-Roell GmbH &Co machine (SMT1-FR100TL.A80). After printing, specimens were machined to remove a few tenths of material from the top and for the bottom of samples to equalise surface roughness.

Impact tests were performed on a 50 J Zwick-Roell GmbH &Co. machine (TG5113E) using samples without the notch.

6.3 Results

6.3.1 Powder characterizations

The first characterization performed regards the particle size distribution of the two alloys. After sieving powders in the 20-63 μm range, the powders' flowability and rheology properties were evaluated.

Powders appear spherical with a very low amount of irregular particles. Scrap powder is characterized by a d_{50} value (the median particle size) of 35.7 µm, while ingot powder has a d_{50} value of 33.7 µm. The SEM images in backscattered electron (BSE) and PSD are shown in **Figure 73**. The main compositional analysis of powders was performed through SEM-EDS, and the results are shown in **Table 29**.

Table 29. Powder composition measured through SEM-EDS

Sample	Si	Cu	Fe	Mn	Mg	Zn	Al
ingot powder	11.57	2.75	0.83	0.3	0.25	0.98	Bal.
scrap powder	11.13	3	0.9	-	0.3	1.14	Bal.

As regards flowability, powders were first subjected to Hall and Carney Flowability tests. As in the literature, no data for AlSi9Cu3(Fe) alloy is available; data from other aluminium alloy compositions were considered for comparison. Chu et al. [149] studied the flowability of the alloy AlSi10Mg. The authors used two batches of powders, one having a span value of 0.94 (D_{10} 22.7 µm, D_{50} 35.5 µm and D_{90} 55.7 µm) and the second one having a span value of 1.17 (D_{10} 22.6 µm, D_{50} 39.3 µm and D_{90} 68.5 µm). Both the powder batches did not flow in Hall flowability tests, confirming the high cohesion forces inside powder particles.

Conversely, Lerma et al. [150] studied the flowability of three Al-Si powders obtained from AlSi7Mg alloy. Mainly, the authors highlight that powders having larger sizes (D_{10} 48 µm, D_{50} 63 µm and D_{90} 83µm and powder having D_{10} 54 µm, D_{50} 70 µm and D_{90} 91µm) have a span of about 0.56 µm and 0.53 µm respectively and can flow in both Hall and Carney tests (about 33 s/50g for Hall and 6.1 s/50g for Carney). Conversely, powders having lower sizes (D_{10} 14 µm, D_{50} 31 µm and D_{90} 58 µm and span of 1.42 µm) do not flow in the Hall Flow test while flow in the Carney funnel in 15.3 s/50g. These results indicate that the flowability in Al powders decreases with the decrease of the PSD and the increase of span. The atomized AlSi9Cu3(Fe) powder has a span of 1.09 µm and did not flow through either the Hall or the Carney funnel.

In particular, powders start flowing into the Carney funnel for up to 15-17 seconds and then stop flowing. Since it was not possible to perform such apparent density tests, only a rheometer can be used to characterize powder flowability.

Rheology results, obtained as an average of three measurements in the 20-63 µm range, are shown in

Figure 74.

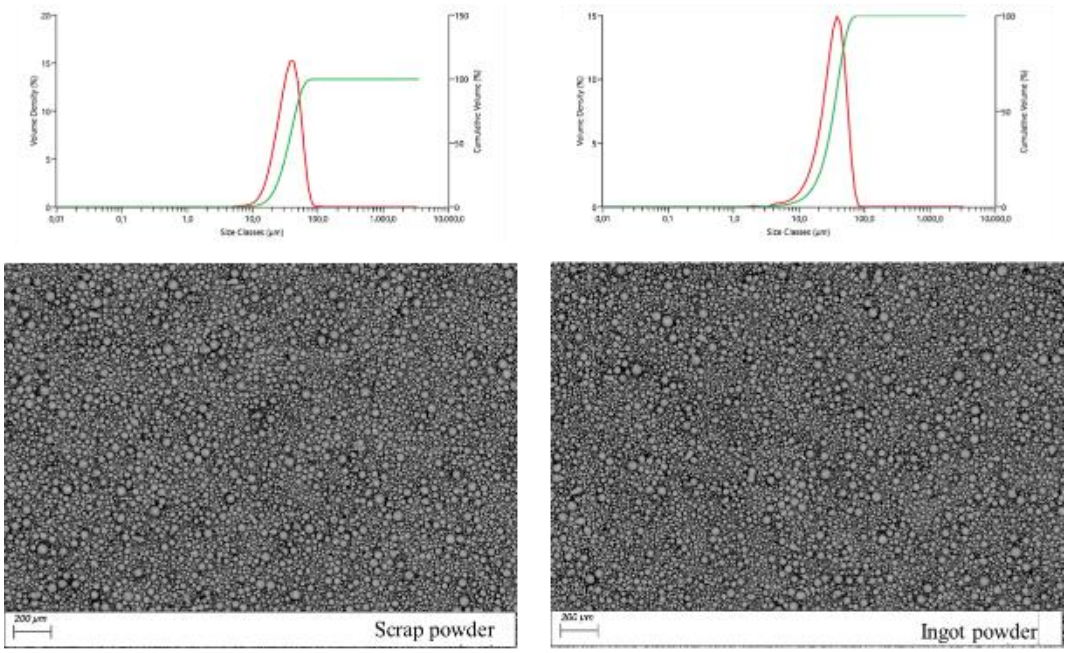

Figure 73. PSD and SEM images of powders. Left side: scrap powders. Right side: ingot powders.

The Basic Flowability Energy (BFE) results in higher values for the ingot powders (188 ± 5.8 mJ) than in scrap powders (160 ± 4.3 mJ), indicating a more efficient packing within the bulk for the ingot powder [117]. Conversely, scrap powder has a low BFE value, indicating enhanced powder flowability. The consolidation flow energy (CE) of the consolidated powders quantified the further resistance to the flow of powder after a step of consolidation. Almost double the energy was measured for scrap powder (about 630 mJ/g compared to about 373 mJ/g of ingot). Such value influenced the compressibility index CI.

The Conditioning Bulk Density (CBD) is measured to assess the ability of the aluminium powder to retain its density and behaviour during processing or storage: both powders gave the same result: 1.69 g/ml.

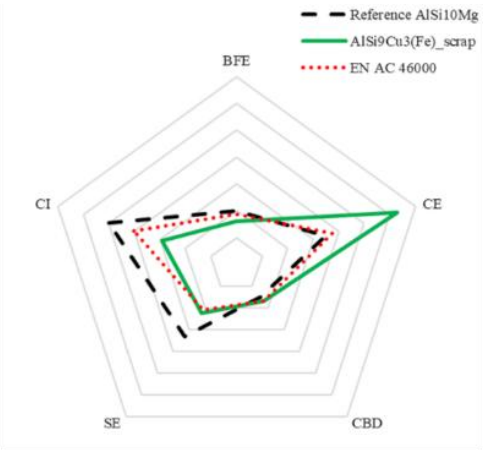

	BFE [mJ]		CE [mJ/g]		CBD [g/cm^3]		SE [mJ/g]		CI [%]	
	AVG	st. dev.	AVG	st. dev.	AVG	st. dev.	AVG	st. dev.	AVG	st. dev.
Reference AlSi10Mg	201.1	11.00	349.7	3.50	1.5	0.10	3.3	0.20	5.0	0.20
AlSi9Cu3(Fe)_scrap	160.0	4.29	629.7	8.65	1.7	0.01	2.2	0.09	3.9	0.16
EN AC 46000	188.1	5.79	372.8	12.48	1.7	0.01	2.1	0.09	2.0	0.03

Figure 74. Qualitative Radar diagram and obtained rheological parameters in scrap powder, ingot powder (EN AC 46000) and state-of-the-art AlSi10Mg powder [149].

Specific Energy (SE) does not differentiate the two powders. Relatively low values were obtained, indicating that low energy is required to spread both powders. Values obtained were 2.10 ± 0.09 mJ/g in ingot powders and 2.23 ± 0.09 mJ/g in scrap powders. SE results are mainly affected by interparticle forces. In powder bulk flow, these forces increase as the particle size decreases [151]. SE value is slightly higher in scrap powders as scrap powder has lower particle sizes.

A low compressibility value (CI) indicates good powder flowability. The different compressibility values observed at 15kPa between ingot and scrap powders are attributable to the influence of the powder's size (Figure 4). A very low compressibility result reflects the relatively efficient packing of the particles due to their spherical shape [152].

The stability index SI resulted in a value close to one: 0.98 in scrap powders and 1.03 in ingot powders. As any value outside the range of 0.9 – 1.1 indicates

instability, both powders can be considered stable; thus, they are not affected by the repetitive application of shear stresses.

The behaviour of the two powders in terms of Flow Rate Index (FRI) is similar; the closer the FRI value is to 1, the more insensitive the powder is to the change in flow rate. Ingot powder FRI resulted in 1.35 ±0.02, scrap powder in 1.44 ±0.01. Finally, the ingot powder had a tap density of 1.79 g/ml, lower than the scrap powder tap density (1.84 g/ml). These values mean that scrap powders may be compacted slightly more effectively. As regards SI, FRI, and tap density, no information on state-of-the-art powders was found.

Through He picnometry, the true densities of powders were measured, finding a powder density very similar in both compositions, of 2.7656 g/cm^3 for ingot powder and 2.7602 g/cm^3 for scrap powder.

XRD analyses were performed in both ingot and scrap powders; results are shown in **Figure 75**.

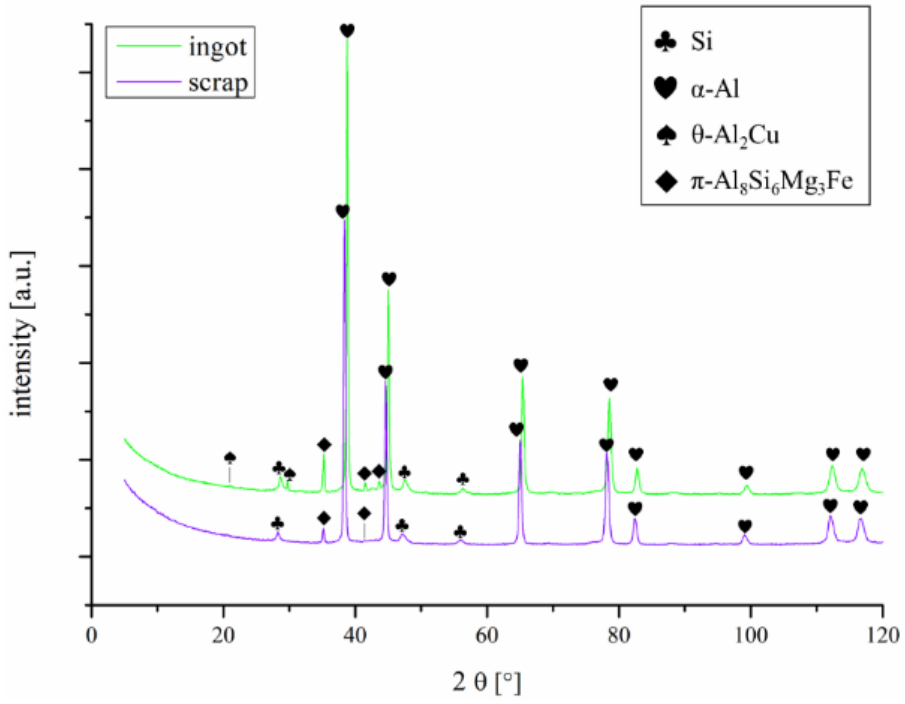

Figure 75. XRD in ingot and scrap powders (20-63 µm size).

Both powders exhibit specific peaks corresponding to the α-Al matrix phase, the eutectic Silicon, θ-Al_2Cu and the π-Fe phase $Al_8Si_6Mg_3Fe$. Ingot powder is characterized by a higher amount of peaks in the 2θ range 20°-60°, belonging to θ-Al_2Cu and the π-Fe phases.

Figure 76 depicts the SEM-BSE images of the two powders; in particular, the figure shows the intermetallic phases noticed. Both powders exhibit intermetallic phases, Cu-containing and Fe-containing. These intermetallic phases are homogeneous distributed inside the particles.

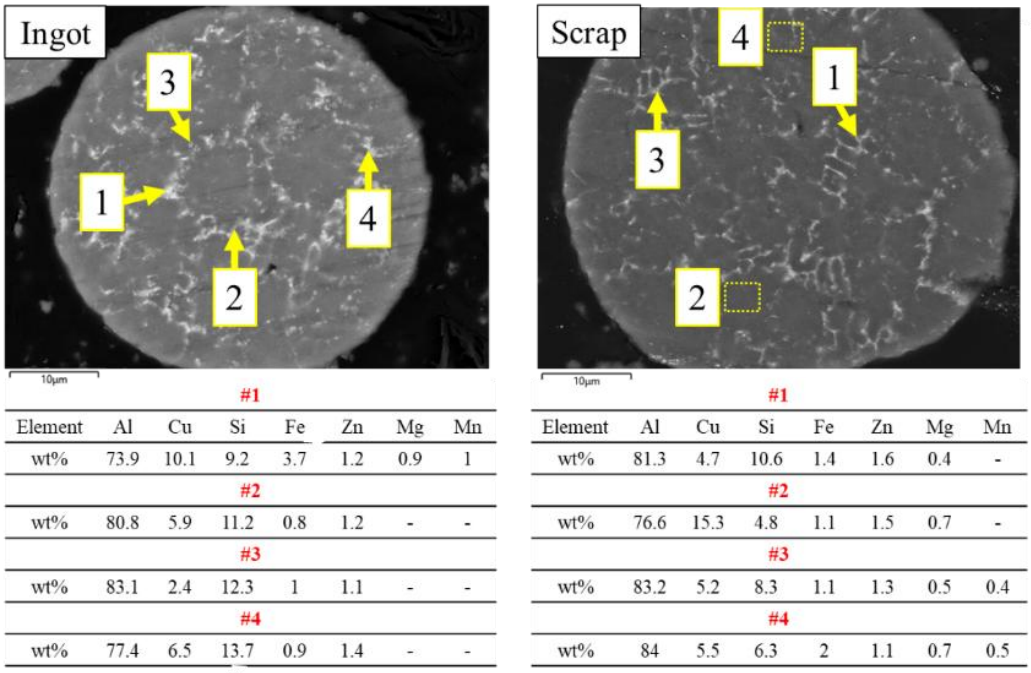

Ingot							
#1							
Element	Al	Cu	Si	Fe	Zn	Mg	Mn
wt%	73.9	10.1	9.2	3.7	1.2	0.9	1
#2							
wt%	80.8	5.9	11.2	0.8	1.2	-	-
#3							
wt%	83.1	2.4	12.3	1	1.1	-	-
#4							
wt%	77.4	6.5	13.7	0.9	1.4	-	-

Scrap							
#1							
Element	Al	Cu	Si	Fe	Zn	Mg	Mn
wt%	81.3	4.7	10.6	1.4	1.6	0.4	-
#2							
wt%	76.6	15.3	4.8	1.1	1.5	0.7	-
#3							
wt%	83.2	5.2	8.3	1.1	1.3	0.5	0.4
#4							
wt%	84	5.5	6.3	2	1.1	0.7	0.5

Figure 76. SEM-EDS analysis. Intermetallic compositions

6.3.2 L-PBF

After the first set-up of **Table 28**, it was clearly noticed that low Laser power and high hatch distance lead to a higher amount of porosities and defects inside samples (see **Figure 77**). The best result was achieved with 200 W as laser power and 80 μm as hatch distance; on the other hand, samples were still not sufficiently dense and free of defects.

After selecting the optimized condition of laser power and hatch distance, in the second step of printing parameter set-up, point distance and exposure time were changed to print 9 cubes. As a consequence of point distance and exposure time variations, even the printing speed changed. Notably, low exposure time leads to a marked lack in density regardless of point distance value. Very good results were achieved at 150 μs of exposure time and a small point distance (40 μm).

After printing, cubes were cut along the built direction and polished to observe the microstructure cross-section and measure the density using image analysis software. Image analysis software works on the black-and-white scale, considering the black signal as a lack of material. Samples exhibiting low density are characterized by a lack of fusion and gas porosity.

Despite the cubes being successfully printed using platform temperature at 30 °C, difficulties were noticed in printing bar samples. Notably, the platform at room temperature appears to affect the residual stresses inside the specimens, causing sample displacements and the need to interrupt the whole printing process or stop some specimens that exhibit displacements. In this sense, a platform temperature of 165 °C was selected instead of 30°C. Remarkably, such temperature represents the maximum machine temperature.

Figure 78 shows mechanical specimens while the parameters used to print mechanical specimens are shown in **Table 30**.

Despite the increase in the platform temperature up to 165 °C, few displacements were still noticed. In the first instance, different pin shapes that connect the sample to the printing platform were used to avoid displacements. Nevertheless, displacements were still present, leading to printing specimens directly on the platform, without pins. The first approach using pins permits quick removal of the printed specimens and rapid restoration of the platform surface by grinding to smooth its surface. On the other hand, pins appear to cause displacements in large specimens, as in **Figure 79**.

After selecting the best printing conditions even for large mechanical specimens, two betches containing six sample each were print directly on the platform suface, without pins, using parameters as in **Table 30**.

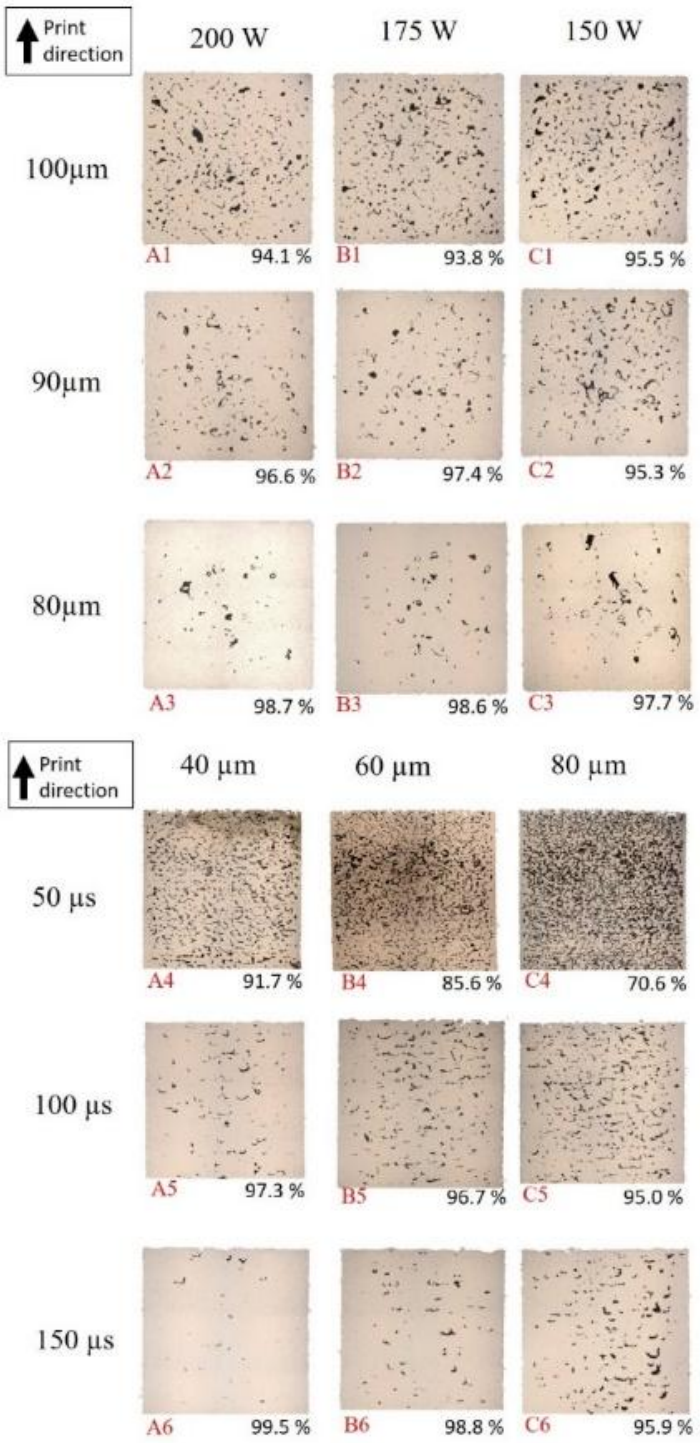

Figure 77. Printing setup. Microstructures (OM) and density percentage. First setup (left side) power vs hatch distance; second setup (right side) point distance vs exposure time.

Table 30. L-PBF parameters

Laser power W	Layer thickness [µm]	Hatch spacing [µm]	Speed [mm/s]	Atmosphere	Scanning strategy	Platform T. [°C]
200	30	80	266.67	Ar	rot. 67°	165 °C

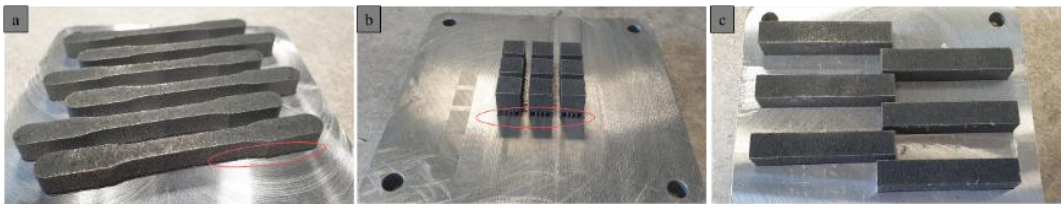

Figure 78. L-PBF specimens. a) tensile specimens; b) cubs with pins; c) impact samples (bars).

(a) Cube displacements and flaking behaviour

(b) interrupted printing for high residual stresses - flaking behaviour

(c) interrupted printing for feeding issues

Figure 79. L-PBF specimens. Defects during printing

Micro-hardness was measured in as-built specimens printed at 30 °C and at 165 °C. Notably, samples printed at 30 °C result in higher micro-hardness of 146.9 ± 5.5 HV0.5, while specimens printed at 165 °C result in 117.3 ± 5.9 HV0.5.

The printing set-up with the direct print on the platform and the platform heating strongly reduced the residual stresses inside specimens, avoiding shape defects. Conversely, direct print requires machining processes to remove specimens from the platform, increasing costs and time.

Figure 80 shows the microstructures of L-PBF AlSi9Cu3(Fe) specimens observed at the OM. As a reference, L-PBF AlSi10Mg specimens were printed in an external laboratory; cubes and mechanical specimens (dog bones for uniaxial tensile tests and bars for Charpy impact test) were printed.

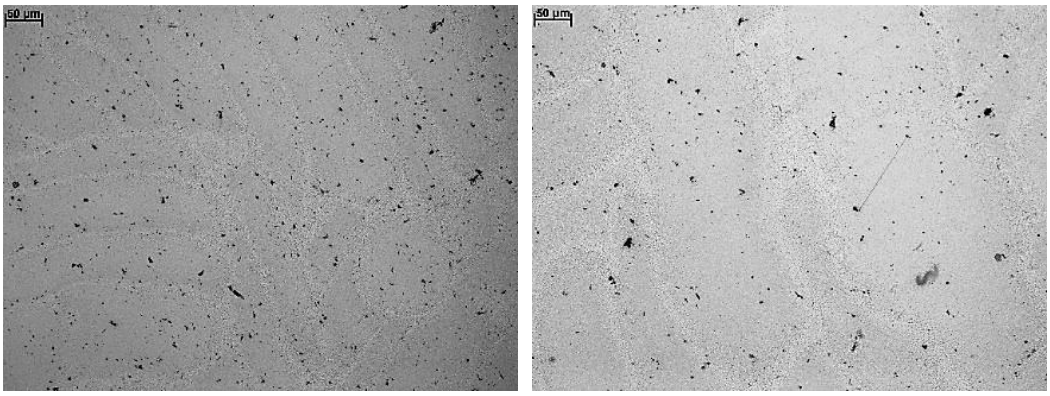

(a) OM - AlSi9Cu3(Fe) scrap (b) OM - AlSi9Cu3(Fe) ingot

Figure 80. Optical Microscope images of the two alloys in the as-built state.

6.3.3 As-built microstructure

As-built microstructures are shown in

Figure 81. Both alloys appear to have a fine microstructure and a homogeneous distribution of intermetallic phases along the melt pools. The composition of the as-built specimens was measured by SEM-EDS and is reported in **Table 31**.

The analyses through SEM-EDS do not evidence the presence of θ-Al_2Cu intermetallics; the Mg depletion hindered the Q-phase nucleation, while phases Al-Si-Cu-Fe were noticed.

Figure 82 shows details about the melt pool microstructure. The observed microstructures are characterized by superimposed melt pools having an average height of about 29.1 ± 1 μm and a measured length of 144.8 ± 28.5 μm. Very fine cellular structures were observed in both alloys at higher magnification. The fine cellular substructure is clearly noticeable.

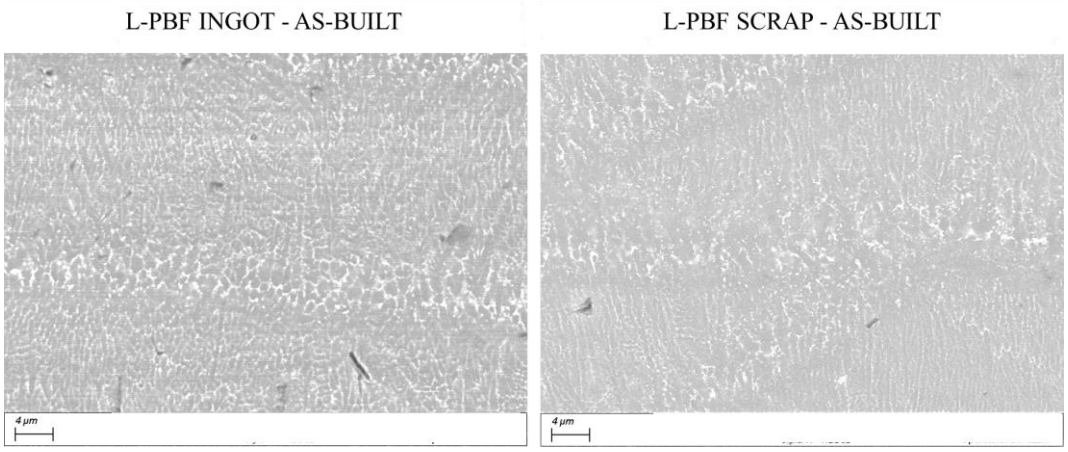

Figure 81. SEM images - ingot and scrap specimens printed by L-PBF.

Table 31. L-PBF samples composition measured through SEM-EDS

Sample	Si	Cu	Fe	Mn	Mg	Zn
L-PBF ingot	9.6	1.4	0.5	0.2	0.3	0.3
L-PBF scrap	86.2	2.7	0.8	0.3	-	0.7

Inside each melting pool, cells are finer, and visible elongation can be noticed in a specific direction. Such elongation is determined by the gradient in temperature inside the melt pool because the heat conduction takes place radially. Cells can be distinguished from each other thanks to the melt pool borders that are characterized by large cells that are mainly rounded.

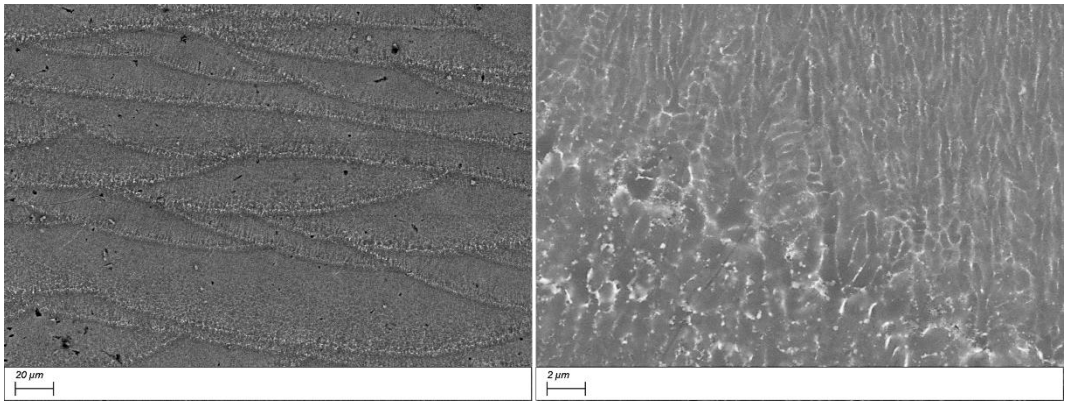

Figure 82. Details in L-PBF scrap sample (as-built). Melt pools (left side) and cellular structure (right side).

6.3.4 Residual stresses

To understand the residual stress behaviour of specimens before the uniaxial tensile test, residual stress measures were performed. Particularly, measures were conducted in one sample in the as-built state (print parameter as **Table 30**) and after the sample machining.

Figure 83 shows residual stress results for a dog-bone L-PBF specimen.

In particular, specimens in the as-built state showed an almost uniform tensile stress behaviour in all the examined directions, in particular in the direction 90 ° and 180 °.

After the machining, stresses become compressive, while in the zy direction of the specimen, they become almost zero. A stress state after machining leads to a compressive stress state on the specimen's surface; compressive stresses are preferable when performing uniaxial tensile tests because they can hinder the initiation cracks, mainly in fatigue tests [153].

Residual stress measures were even performed on the bar sample in the as-built state and after machining and results are shown in

Figure 84. As noticed in dog bone specimens, substrate residual stresses become compressive after machining. These analyses want to assess the feasibility of the machining that appears to positively affect the surface stress behaviour.

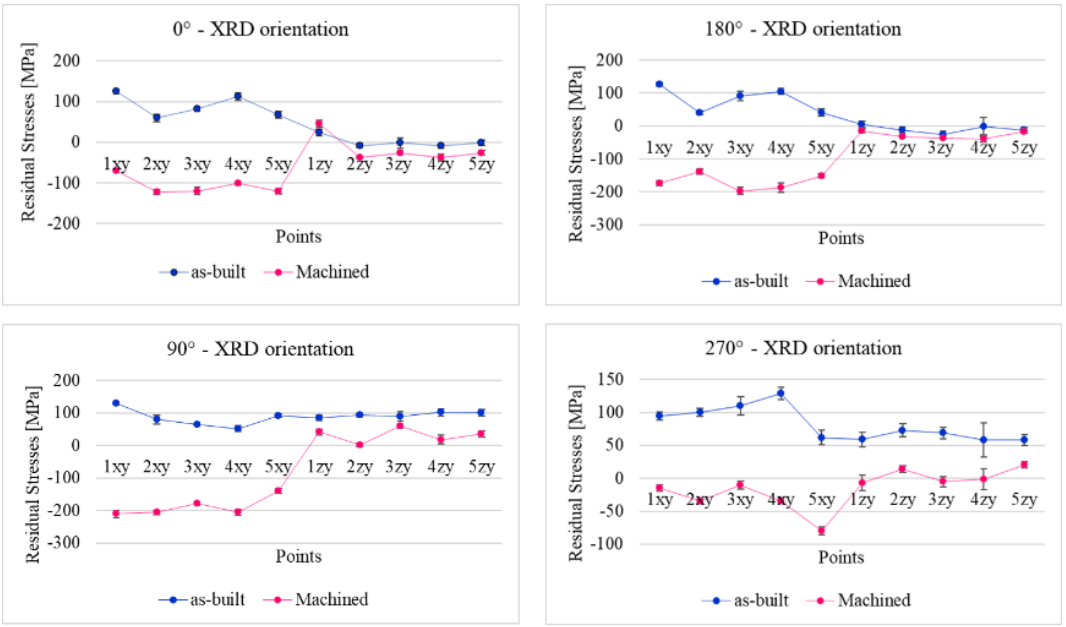

Figure 83. Residual stress measures on L-PBF ingot dog bone specimen

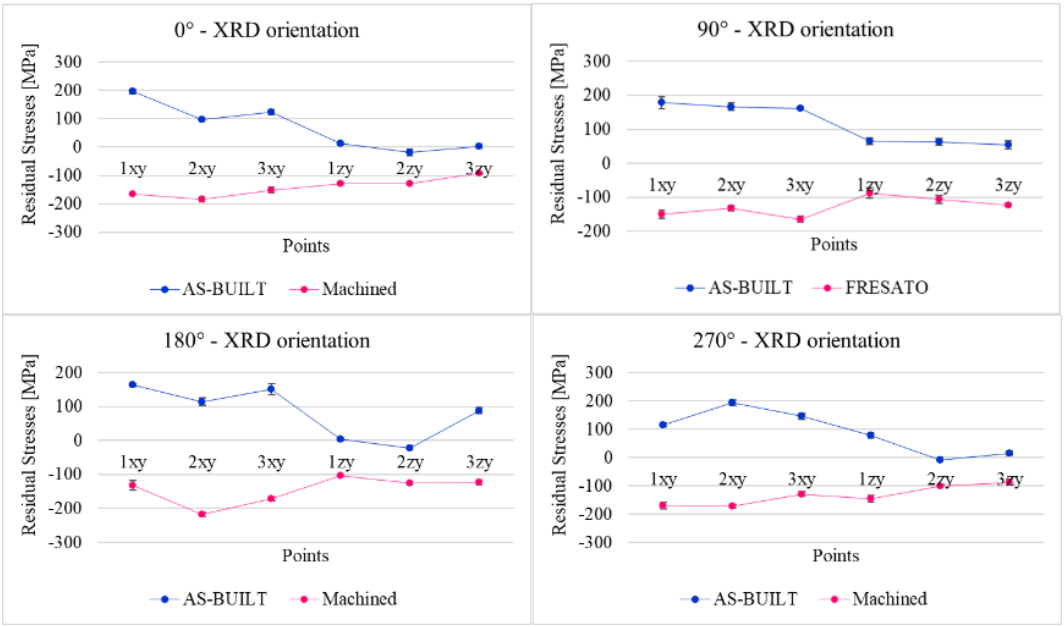

Figure 84. Residual stress measures on L-PBF ingot bar specimen

6.3.5 Heat treatments

The application of heat treatments leads to a change in the specimen's microstructures. As explained in 6.2.5, two different solubilization temperatures were used, followed by the same artificial ageing process.

Heat treatment at high temperatures (515 °C) strongly affects the porosity amounts and size, as will be noticeable from SEM analyses. Conversely, a solubilization temperature of 470 °C less affects the specimens' porosities. Eutectic silicon becomes coarser during the heat treatments.

In

Figure 85, the cross sections of L-PBF-scrap specimens after heat treatments are shown. In particular, a certain Si coarsening can be noticed after the solubilization treatment conducted at 515 °C, while Si starts to diffuse from the oversaturated solid solution.

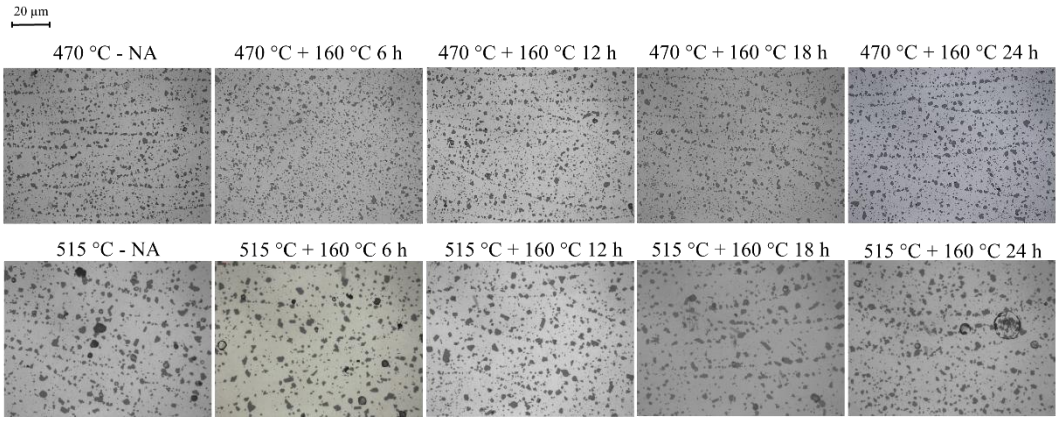

Figure 85. Eutectic Silicon evolution in T6 heat treatments at 470 °C and 515 °C

After T6 heat treatment, the alloy microstructure appears homogenized, and the Si network is disintegrated while intermetallic phases are visible in the melt pool borders. The higher the solubilization temperature, the higher the Si particle dimension, as can be noticed from

Figure 86. Moreover, plate-like Al-Si-Cu-Ni-Fe intermetallic phases were noticed after the solution temper at 515 °C.

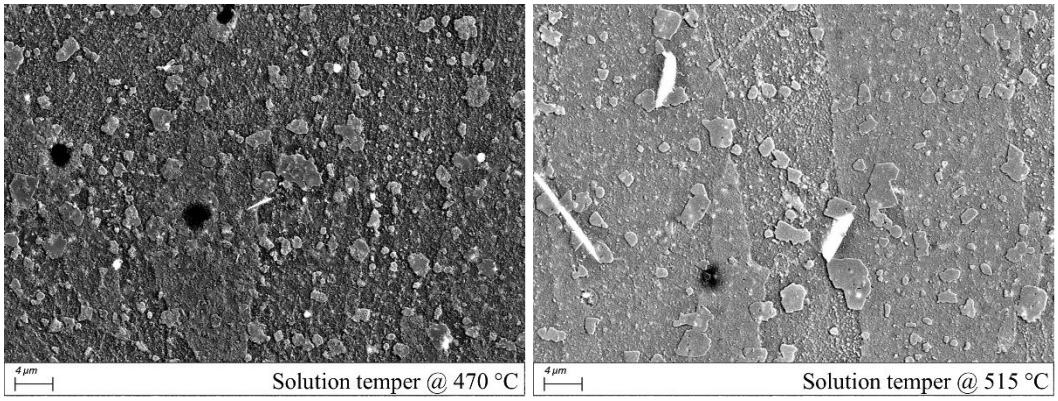

Figure 86. Effect of different solution temper temperatures on the silicon particle dimension and intermetallic phases.

The ageing conducted at 160 °C will promote the decomposition of the oversaturated α-Al matrix obtained after the quenching. The coherent Guinier Preston zones obtained after quenching are dissolved during the long heat treatment and precipitate in θ" phase; for long treatment, the incoherent equilibrium phase θ-Al_2Cu is obtained.

A significant amount of porosities was noticed in specimens treated at a solubilization temperature of 515 °C (**Figure 87**). These porosities are probably due to the θ-Al_2Cu phase present in the as-built microstructure that undergoes melting during the solution temper. In fact, up to 495 °C, the risk of incipient melting of the θ-Al_2Cu phase exist.

Moreover, from the literature, maximum strength in Al-Si-Cu alloys is obtained at the maximum amount of θ" phase [126]. In this sense, the micro-hardness of the samples at the different heat treatment steps was measured, and the micro-hardness

obtained is summarized in

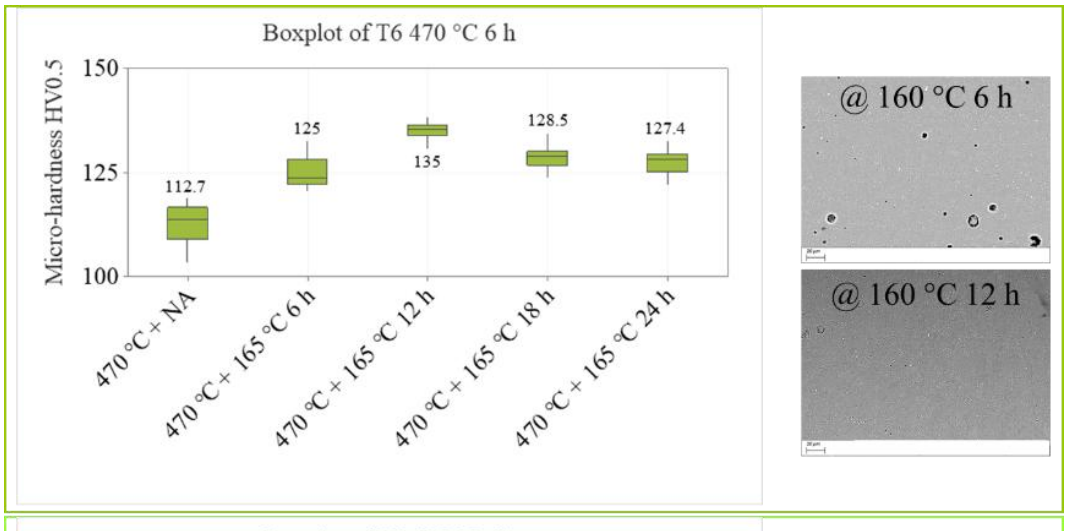

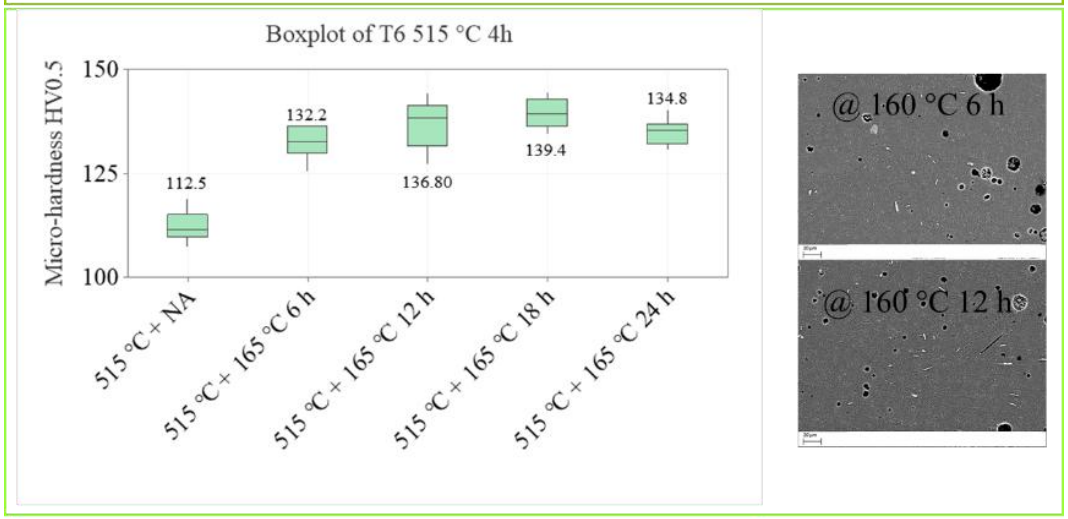

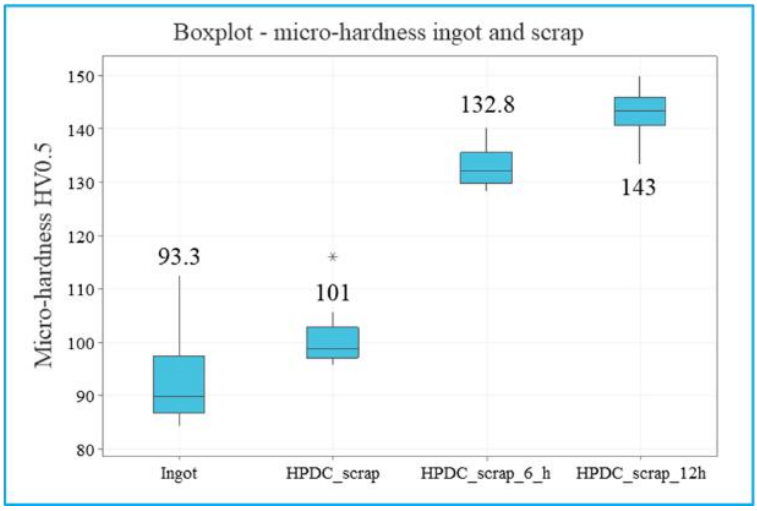

Figure 88.

Micro-hardness results were compared with the micro-hardness results of ingot alloy, scrap HPDC component and micro-hardness of scrap HPDC subjected to heat treatment.

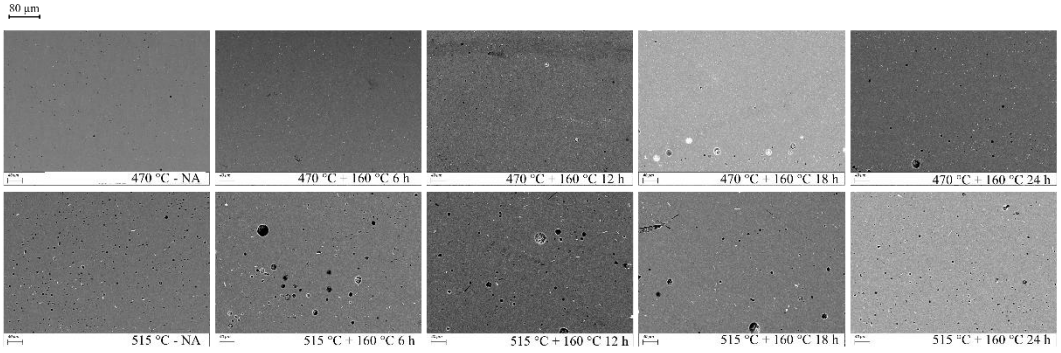

Figure 87. SEM-BSE electron images at 500x magnification. Porosities arise after heat treatments.

In

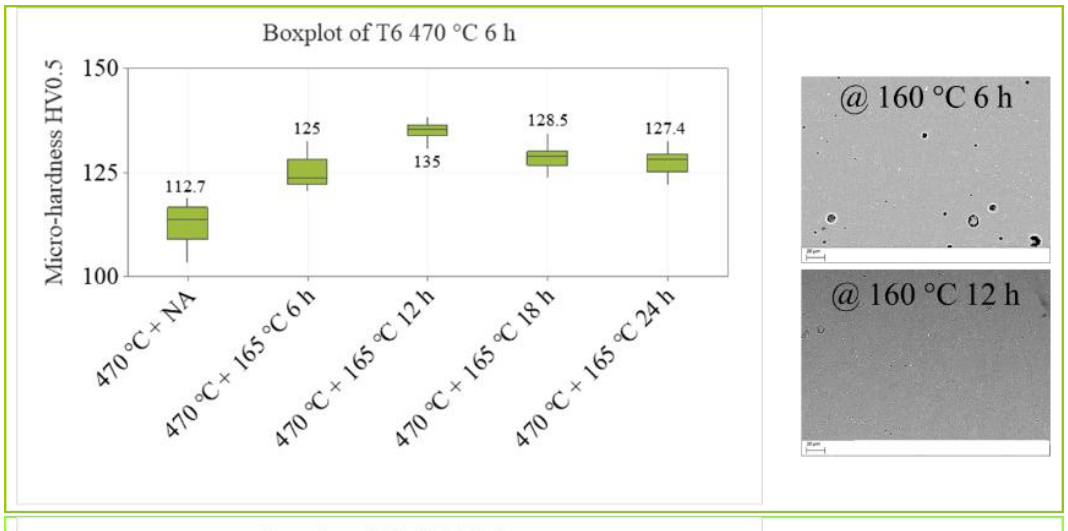
Boxplot of T6 470 °C 6 h
Micro-hardness HV0.5
150
125
100
112.7
125
135
128.5
127.4
470 °C + NA
470 °C + 165 °C 6 h
470 °C + 165 °C 12 h
470 °C + 165 °C 18 h
470 °C + 165 °C 24 h
@ 160 °C 6 h
@ 160 °C 12 h

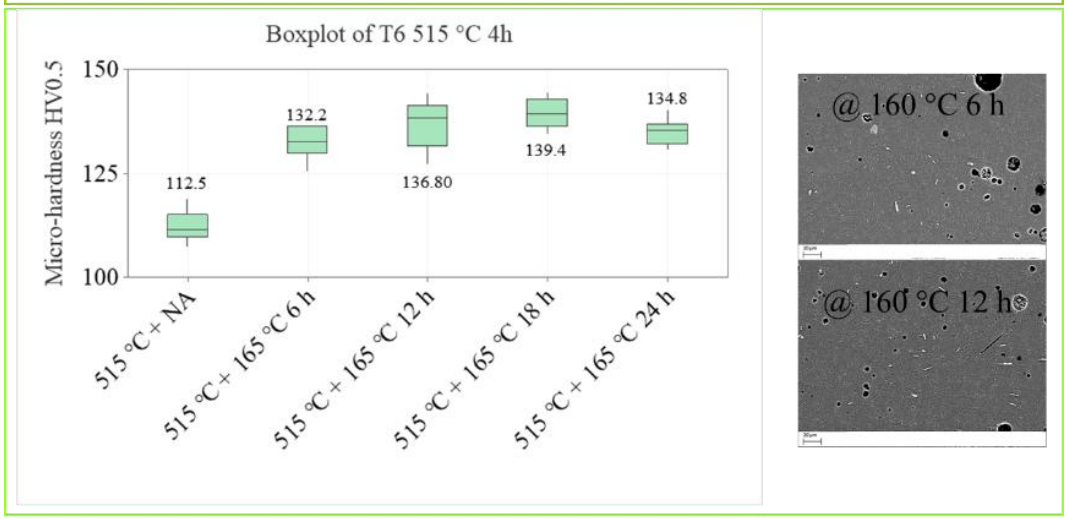
Boxplot of T6 515 °C 4h
Micro-hardness HV0.5
150
125
100
112.5
132.2
136.80
139.4
134.8
515 °C + NA
515 °C + 165 °C 6 h
515 °C + 165 °C 12 h
515 °C + 165 °C 18 h
515 °C + 165 °C 24 h
@ 160 °C 6 h
@ 160 °C 12 h

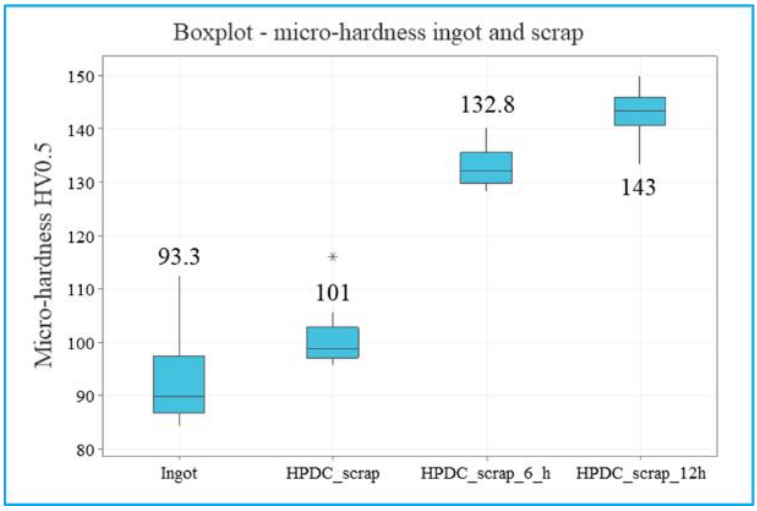
Boxplot - micro-hardness ingot and scrap
Micro-hardness HV0.5
150
140
130
120
110
100
90
80
93.3
101
132.8
143
Ingot
HPDC_scrap
HPDC_scrap_6_h
HPDC_scrap_12h

Figure 88 the microstuctures of specimens that correspond to the high micro-hardness values are shown.

Notably, as previously discussed, a certain amount of pores can be noticed in specimens aged at 515 °C because of the melt of θ-Al_2Cu; furthermore, few porosites can be due to the print process too. In heat treatments at 470 °C, no melting of θ-Al_2Cu is attended. From the DSC, θ-Al_2Cu melting is attended at temperatures up to 490 °C (**Figure 53**).

Micro-hardness values at a solubilization temperature of 515 °C appear to increase up to 18 hours, then at 24 hours of ageing, a decrease in average micro-hardness was measured. The maximum average value obtained is 139.4 HV0.5 at 18 hours of artificial ageing. Conversely, at 470 °C as solubilization temperature, the maximum micro-hardness value was noticed at 12 hours of artificial ageing; then, values started decreasing.

In
Figure 89, the microstructures after the solution temper are shown.

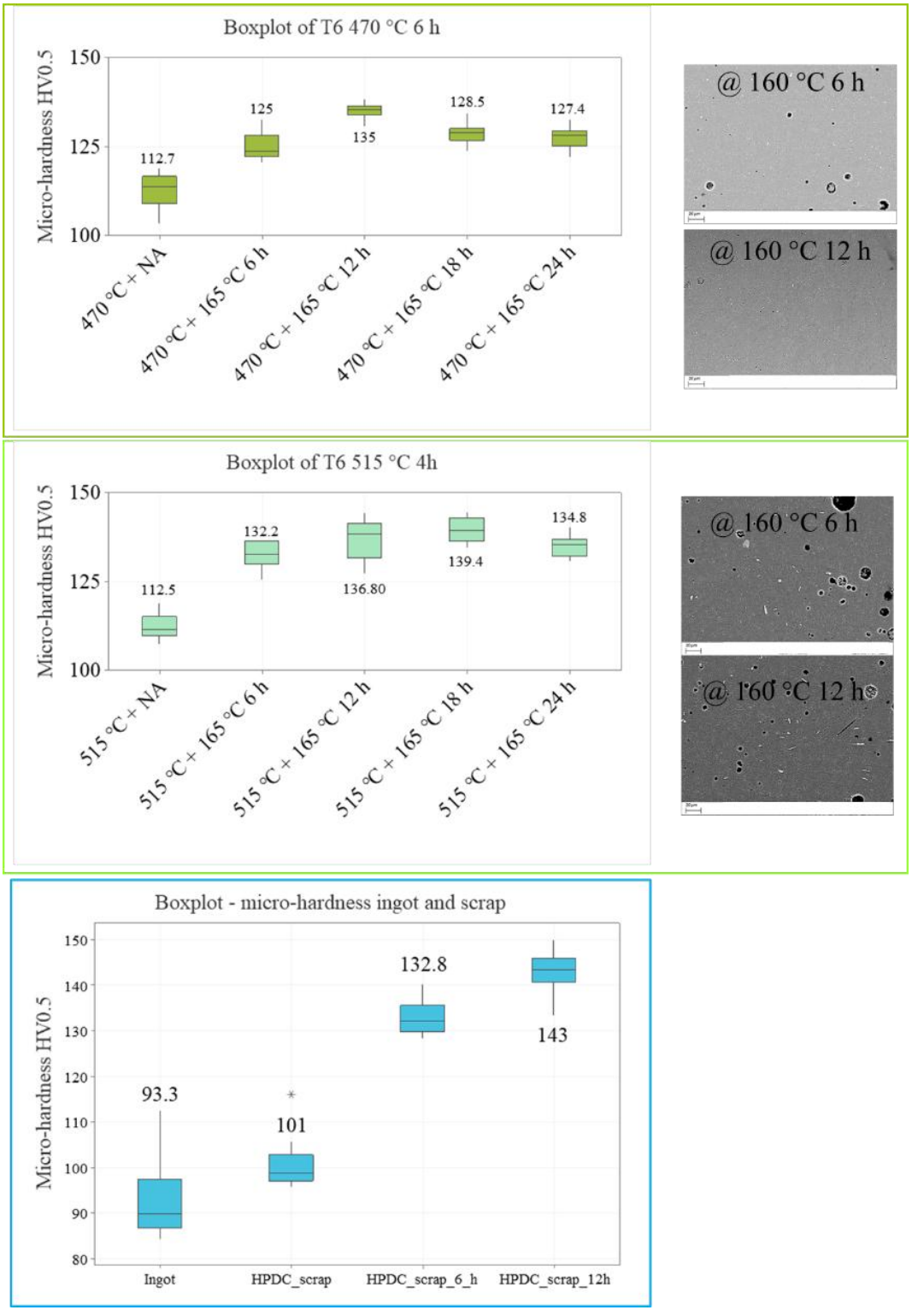

Figure 88. Relation between micro-hardness and ageing times. Box plots for T6 heat treatments at 470 °C and 515 °C solution temperatures.

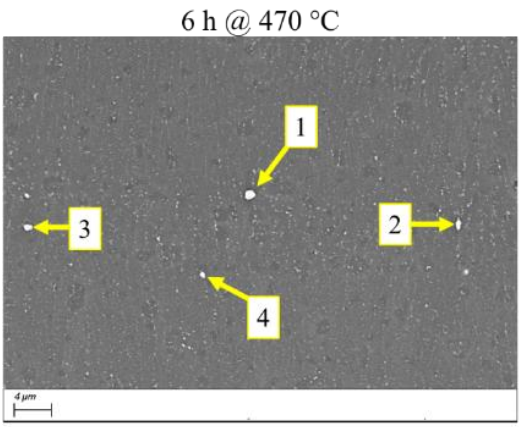

Phase composition

at %	Al	Si	Zn	Cu	Fe
1	76.4	22.7	0.1	0.6	0.2
2	60.7	38.5	-	0.7	-
3	94.4	4.7	-	0.9	-
4	93.0	5.8	-	1.1	-

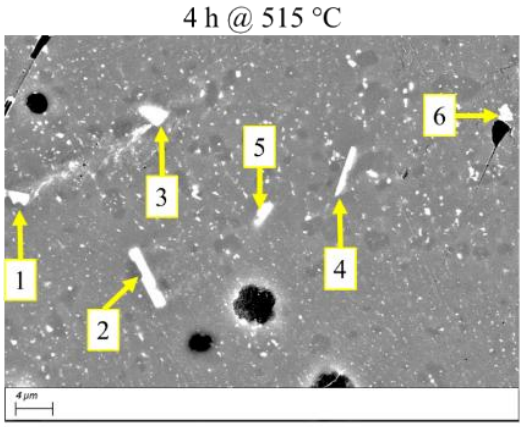

Phase composition

at %	Al	Si	Ni	Cu	Fe	Mn	O
1	55.2	40.1	1.5	2.1	1.2	-	-
2	64.7	22.3	5.4	4.3	3.0	0.3	-
3	75.1	11.0	5.6	4.9	3.1	0.4	-
4	85.5	9.2	0.4	1.4	0.3	-	3.2
5	80.9	15.2	1.0	2.1	0.8	-	-
6	94.8	3.1	-	1.5	0.5	-	-

Figure 89. Heat treatments T6, natural ageing.

After the solution temper at 515 °C, the microstructure is characterized by large platelet-like intermetallic phases Al-Si-Ni-Fe, as reported in [154]. Nickel, particularly, was noticed only in such intermetallic phases, while no significant amount was detected in the base alloy or during the powder compositional analyses. These intermetallic phases Ni-containing were only noticed in the sample treated at 515 °C, while the specimen solubilized at 470 °C showed θ-Al_2Cu embedded into the Si network.

After the first 6 hours of ageing (

Figure 90), microstructure and intermetallic phases appear similar to the as-solubilized state. On the other hand, an increase in micro-hardness values up to 10 HV0.5 in sample solubilized at 470 °C and up to 20 HV0.5 in sample solubilized up to 515 °C were noticed. Such micro-hardness increase is consistent with the precipitation of θ" phase, not discernible through SEM.

6 h @ 470 °C + 160 °C 6 h

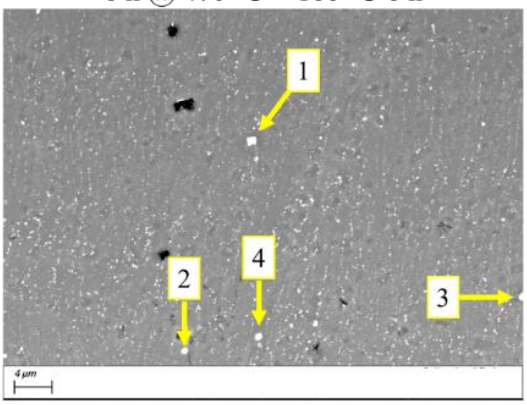

Phase composition

at %	Al	Si	Mn	Cu	Fe
1	97.0	2.3	-	0.7	-
2	95.2	4.1	-	0.7	-
3	63.5	35.9	-	0.4	0.2
4	80.3	18.4	0.2	0.8	0.3

4 h @ 515 °C + 160 °C 6 h

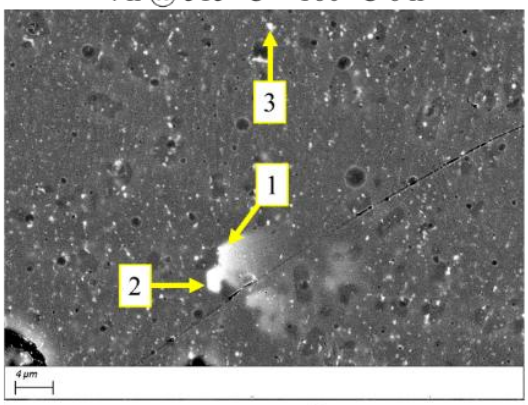

Phase composition

at %	Al	Si	Ni	Cu	Fe	Mn
1	77.9	9.9	4.8	4.2	3	-
2	72.1	16.8	4.2	4.2	2.6	-
3	85.3	9.7	-	2.1	2.2	0.7

Figure 90. Heat treatments T6, artificial ageing 6 h at 160 °C.

Specimen treated T6 6 h at 470 °C and aged 6 h at 160 °C showed intermetallic phases slightly larger than specimen after solution temper, while the phase composition resulted similar. On the other hand, after T6 4 h at 515 °C and ageing of 6 h at 160 °C large intermetallic phases Ni-containing were still noticed.

In

Figure 91, the microstructures after an ageing of 12 hours are reported. Focusing on different intermetallic phases. Both Al-Cu phases and Ni-containing phases were noticed, having different shapes. AlCu phases appear spherical, while Ni-containing phases have a rod shape and are characterized by a higher amount of Ni and Cu than the phases after 6 hours of ageing.

In

Figure 92, the microstructures of heat-treated specimens at 18 hours of ageing are shown. After 18 hours of ageing and a solubilization temperature of 515 °C, two types of intermetallic phases were noticed. The one containing Cu and iron and the one Ni-containing, as in the previous case. On the other hand, the amount of Ni, Cu

and Fe in those phases appears reduced. The micro-hardness value measured is similar to the value after 12 hours. Specimen solubilized at 470 °C started showing a decrease in average micro-hardness up to 7 HV0.5, while in the microstructure, intermetallic phases Ni containing were noticed.

6 h @ 470 °C + 160 °C 12 h

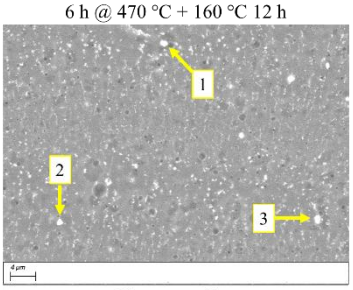

Phase composition

at %	Al	Si	Ni	Cu
1	65.8	24.7	2.3	7.2
2	85.7	6.9	1.7	5.8
3	71.6	20.2	1.4	

4 h @ 515 °C + 160 °C 12 h

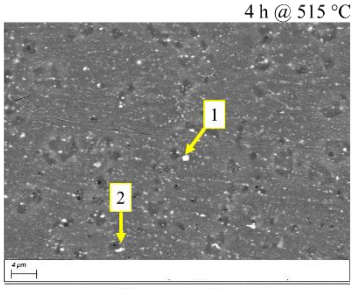

Phase composition

at %	Al	Si	Cu	Fe
1	92.8	5.4	1.5	0.3
2	59	39.5	1.1	0.4

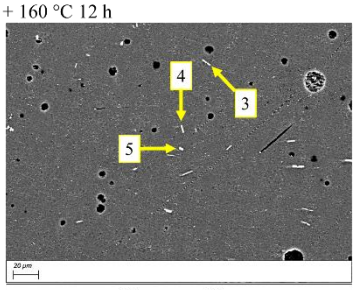

Phase composition

at %	Al	Si	Cu	Fe	Ni	Mn
3	76.6	9	6.6	3.1	4.7	-
4	63.9	12.3	8.9	4.9	9.4	0.6
5	57.7	11.5	10.9	6.7	12.3	0.9

Figure 91. Heat treatments T6, artificial ageing 12 h at 160 °C.

6 h @ 470 °C + 160 °C 18 h

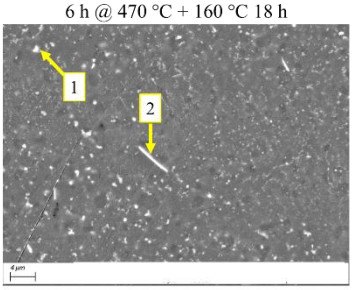

Phase composition

at %	Al	Si	Ni	Cu	Fe
1	89.6	8.3	-	1.5	0.6
2	87	9.5	0.9	2.0	0.6

4 h @ 515 °C + 160 °C 18 h

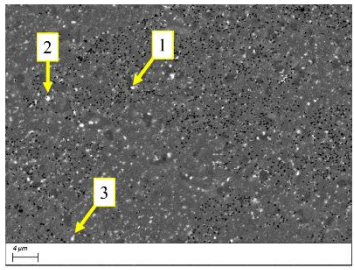

Phase composition

at %	Al	Si	Cu	Fe	Mn
1	37.5	61.3	0.7	0.6	-
2	64.9	31.7	1.5	1.5	0.5
3	31.0	67.0	0.6	0.8	-

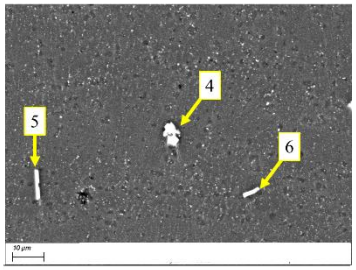

Phase composition

at %	Al	Si	Cu	Fe	Mn	Ni
4	71.1	16.3	4.5	2.9	-	5.2
5	77	10.8	4.5	2.6	0.5	4.7
6	65	23.1	4.2	3.1	-	4.6

Figure 92. Heat treatments T6, artificial ageing 18 h at 160 °C.

After 24 hours of artificial ageing (

Figure 93), Ni-based intermetallic phases were noticed in all the T6 heat treatments, even if in a higher amount in the sample solubilized at 515 °C. Large intermetallic phases were noticed in the specimen solubilized at 515 °C while its average micro-hardness started to decrease.

Specimen solubilized at 470 °C showed rod-type Ni-based intermetallics and only a slight decrease in micro-hardness with respect to the previous measure.

6 h @ 470 °C + 160 °C 24 h

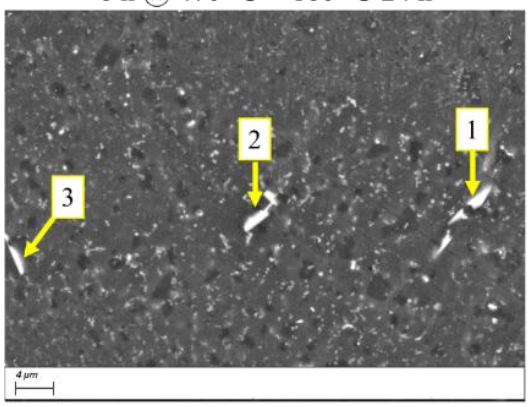

Phase composition

at %	Al	Si	Ni	Cu	Fe	Mn	Zn	O
1	69.7	19.5	2.7	3.3	1.6	0.2	0.2	2.7
2	85.4	3.3	0.7	5.4	1.9	-	-	3.3
3	82.7	10.2	1.0	2.1	0.9	-	0.3	2.8

4 h @ 515 °C + 160 °C 24 h

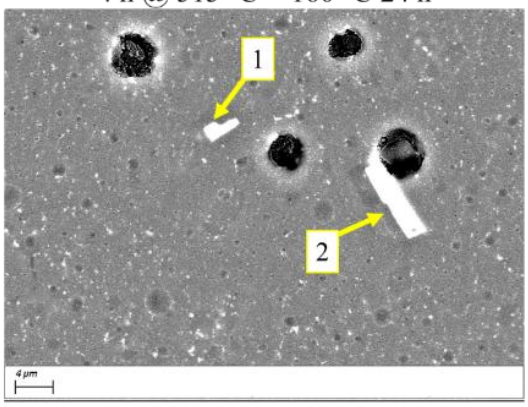

Phase composition

at %	Al	Si	Cu	Fe	Ni	Mn
1	81.1	6.5	4.1	3.0	5.3	-
2	58.2	26.0	5.2	3.4	6.7	0.5

Figure 93. Heat treatments T6, artificial ageing 24 h at 160 °C

The analyses of intermetallic phases, the observation of the internal porosities and the micro-hardness values lead to selecting the optimal heat treatment. Particularly, treatments involving the solubilization at 470 °C were preferred in the perspective of preserving the elongation at rupture. Furthermore, the rod-shaped intermetallic phases noticed in specimens solubilized at 515 °C can be detrimental to the alloy ductility.

Particularly, two heat treatments were selected:

- Solution temper at 460 °C 6 hours and ageing 6 hours at 160 °C;
- Solution temper at 460 °C 6 hours and ageing 12 hours at 160 °C

Additionally, the heat treatments selected were performed on the HPDC scrap part to highlight the differences in terms of microstructure and hardness. In **Figure 88**, the micro-hardness of such specimens is shown.

Notably, the micro-hardness of the ingot alloy and HPDC scrap part was lower than that of the L-PBF micro-hardness. Ingot alloy resulted in 93.3 ± 9.2 HV0.5, HPDC scrap has 101 ± 6.1 and L-PBF samples printed at 165 °C 117.3 ± 5.9. After the T6 heat treatments, HPDC scrap alloy micro-hardness increased to 132.7 ± 3.8 after 6 hours of ageing and to 143 ± 4.6 after 12 hours.

In **Figure 94**, the obtained microstructures were reported as a comparison. In such microstructures are clearly noticeable a certain amount of β-Fe detrimental phase at 6 hours of ageing and sludge α-Fe already in the as-HPDC sample.

The cast specimens showed a higher micro-hardness value than L-PBF samples; on the other hand, the microstructures are rich in detrimental phases such as β-Fe that act as stress efforts intermetallic, stimulating a fragile behaviour of the alloy.

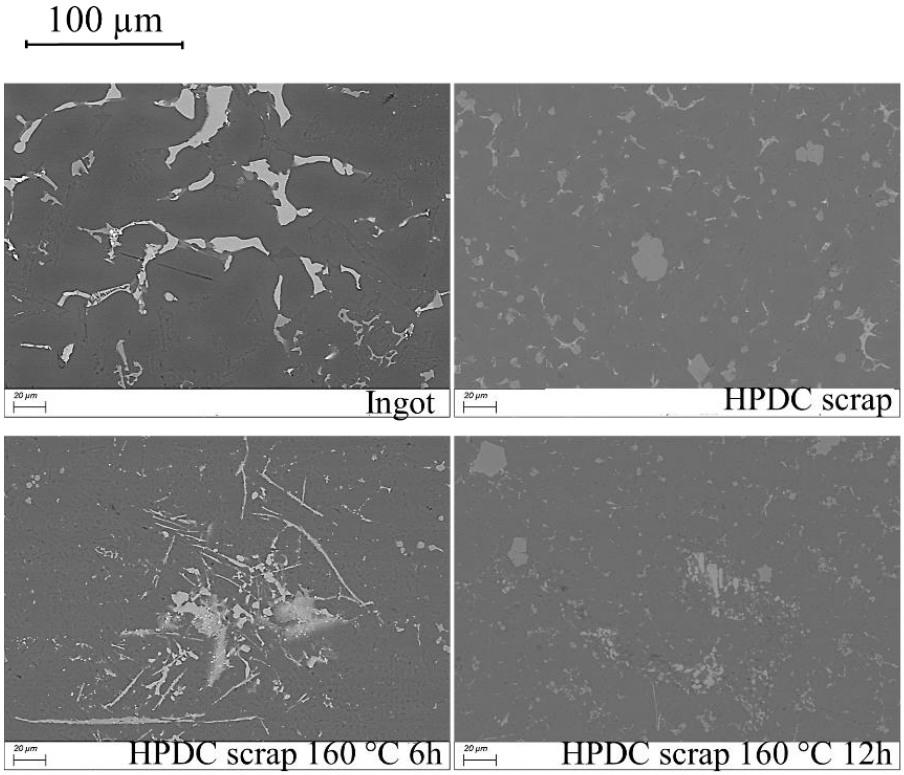

Figure 94. Microstructure of ingot and HPDC scrap before and after T6 HT.

The selected heat treatment in L-PBF was performed directly on the machined specimens. After the heat treatments, samples undergo mechanical tests.

6.3.6 Mechanical properties

The uniaxial tensile test results of the as-built and heat-treated T6 specimens are reported in

Figure 95. Results refer to L-PBF scrap and ingot specimens, while further specimens produced through AlSi10Mg were printed as a comparison. L-PBF AlSi10Mg specimens were tested in as-built condition and after a T5 heat treatment, performing artificial ageing at 160 °C 6 hours [155].

Table 32 reports the uniaxial tensile test data from the literature for HPDC AlSi9Cu3(Fe) alloy and L-PBF specimens in as-built and T6 heat treatment. From the results reported in the table, it appears that tensile L-PBF specimens outperformed with respect to cast specimens.

Nevertheless, mechanical results depend not only on the microstructural features but also on the amount of porosity. In this sense, porosity amounts appear lower in specimens aged up to 6 hours, as shown in

Figure 87.

AlSi10Mg specimens resulted in the best performances in terms of ultimate tensile stress Rm and yield strength $Rp_{0,2}$, in both as-built and T5 heat-treated. Moreover, AlSi10Mg samples appear more uniform in terms of microstructure; in fact, the standard deviation is always low.

AlSi10Mg shows lower results in elongation at rupture; AlSi9Cu3 (Fe) scrap gives very good results as A%; on the other hand, internal defects in a few specimens lead to a large data dispersion.

Table 32. Mechanical properties of L-PBF and HPDC AlSi9Cu3 from literature.

Condition	Rm, $Rp_{0,2}$ [MPa] A [%]	HV	Details	Ref.
As-built	462.5 ± 0.2; 266.1 ± 0.1 4.5 ± 0.12	157.3	Powder size 20-63 µm	[109]
	Powder 1: 455 ± 2.3; 228 ± 2 5.1 ± 0.1 Powder 2: 486.7 ± 4.4; 253.7 ± 2.7 5.3 ± 0.3	-	Powders: Powder 1: avg 46.7 µm Powder 2: avg 42.6 µm	[96]
	374 ± 11; 219 ± 20 2.5 ± 0.2	135.2 ± 4.8	-	[107]
T6	318.7; 206 7.8	-	470 °C 6 h + quenching + 160 °C 24 h	[97]
	380 ± 13; 326 ± 23 2.6 ± 0.2	152.4 ± 5.5	-	[107]
HPDC AlSi9Cu3(Fe)	257 ± 17; 173 ± 14 1.2 ± 0.5	108.1 ± 3.1		[110]

Impact test values resulted in similar values than the HPDC specimens. Notably, the average values shown in

Figure 95 are characterized by a high standard deviation. This means that L-PBF specimens can behave better than HPDC specimens; on the other hand, the amount of printing defects negatively affects the final result. Bar samples of L-PBF scrap printed during the same job and tested in as-built condition, particularly, give very different results in terms of absorbed energy: one absorbed 31.8 J while the other one was only 9 J. The same behaviour was noticed in T6 specimens aged 6 hours: for specimens obtained in the same job, the maximum value was 27.6 J while the minor was 11.6 J.

Conversely, ingot specimens are mainly characterized by a higher porosity amount than scrap specimens: this led to less dispersed results, as noticed for the reference specimens AlSi10Mg.

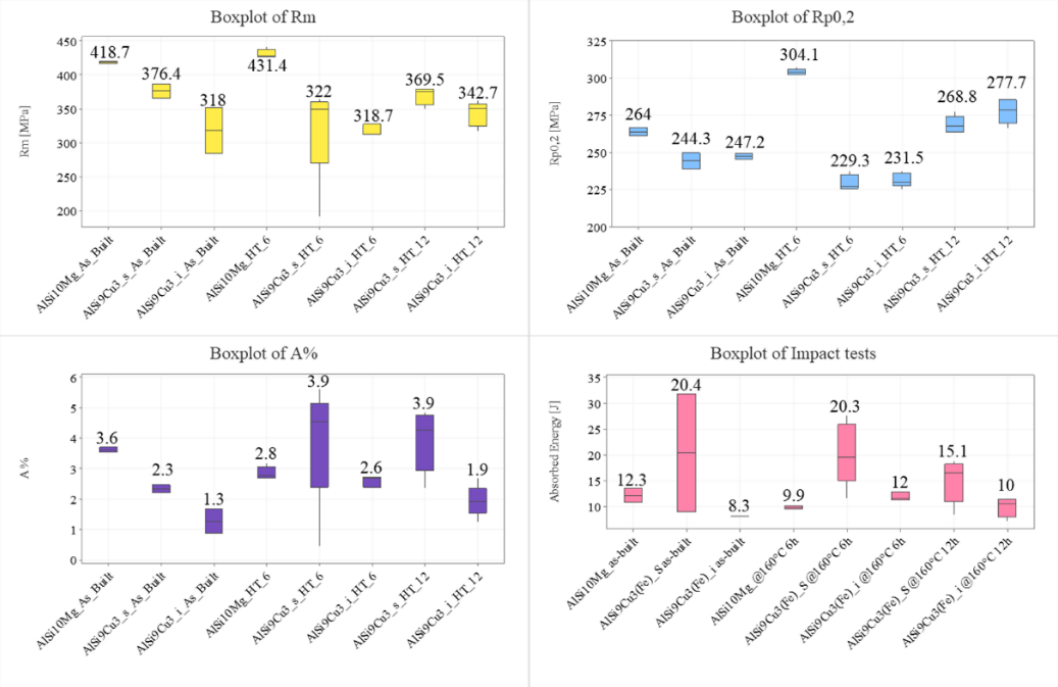

Figure 95. Mechanical test results – $R_{p0,2}$, R_m, A% and absorbed energy (average values).

In

Figure 96, the fracture surfaces of specimens (one for each type of sample) were shown. Notably, scrap specimens in as-built and T6 conditions revealed a low amount of defects. Conversely, ingot specimens showed a high amount of porosities in the whole fracture surface. Similarly to scrap specimens, even the reference specimens AlSi10Mg are characterized by a low amount of defects.

Interestingly, in the as-built state, the Rm values resulted in high because the strength in the as-built specimen depends on different contributions. First of all there is a solution strengthening because of the rapid cooling of the melt pool. The α-Al matrix resulted in the supersaturation of Si and Cu alloying elements. Secondly, there is a strengthening of grain boundary contribution because of the presence of fine grains and the cellular structure.

Finally, even the dislocation strengthening is relevant [156]. Mainly, the network structure of Si acts as a barrier to the dislocation motion.

Furthermore, in T6 heat-treated samples, even the precipitation strengthening takes place; T6 treatment increases the number of the contributions that positively affect the mechanical strength, even if the solution strengthening contribution decreases because Si and Cu start forming intermetallic phases.

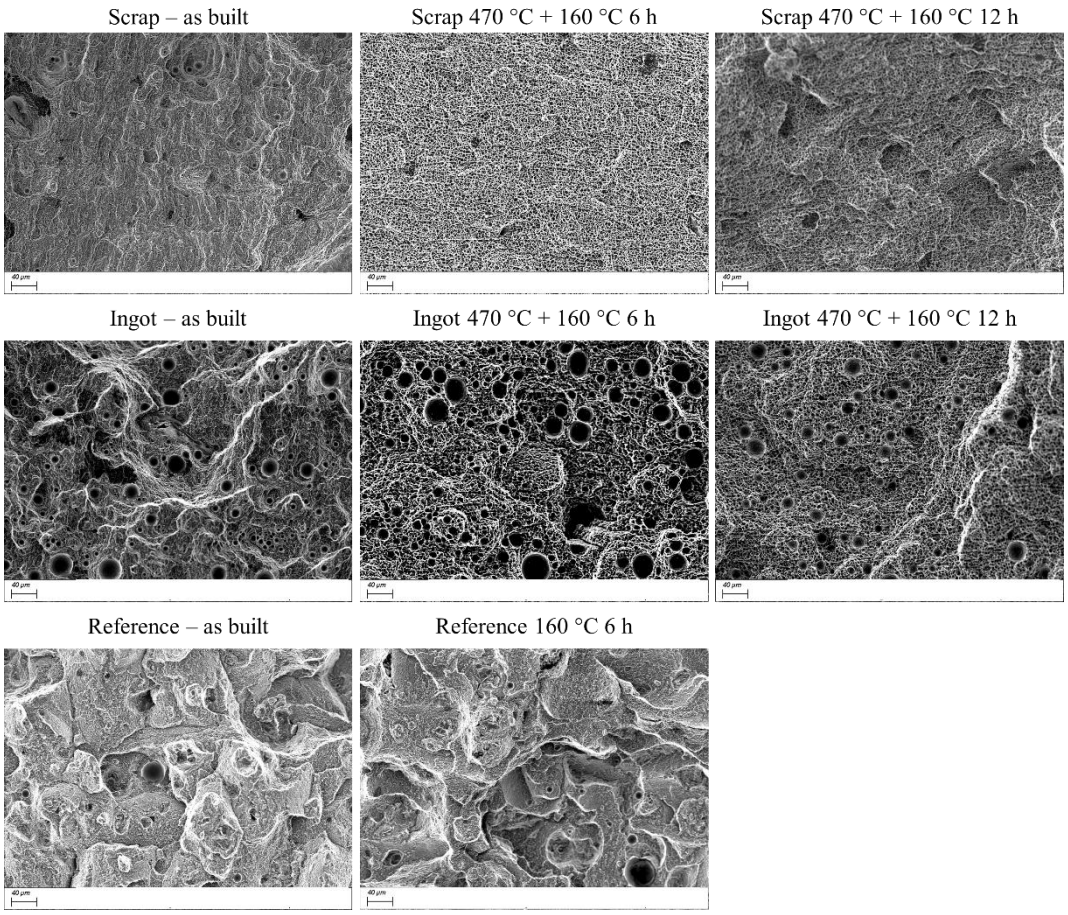

Figure 96. Fracture surfaces in tensile test specimens.

Mainly, the θ″ precipitates that nucleated from the Guinier Preston zone, which play the major role in the alloy strengthening.

Another consideration about as-built samples can be drawn. In fact, paragraph 6.2.3 was reported that the first printing operations were conducted using a platform temperature of 30 °C, nevertheless, after the printing of bars, strong internal stresses were noticed, leading to an increase of the platform temperature at 165 °C.

Cube samples printed on the platform at 30 °C showed a higher micro-hardness value of about 147 HV0.5, while specimens printed at 165 °C resulted in 117 HV0.5. Six dogbone specimens were printed before the change in platform temperatures: six dogbones fractured for residual stresses directly on the platform, while the other three appeared intact. Such three specimens were tested in the as-built state to evaluate the properties when the platform temperature is at about 30 °C.

Figure 97 summarizes the results of uniaxial tensile stress and micro-hardness in scrap L-PBF specimens at different building platform temperature. From

Figure 97, it can be deduced that the high micro-hardness of the specimen printed on a building platform at 30 °C showed lower mechanical properties in as-built conditions. This behaviour can be attributable to the higher residual stresses inside specimens printed at 30 °C.

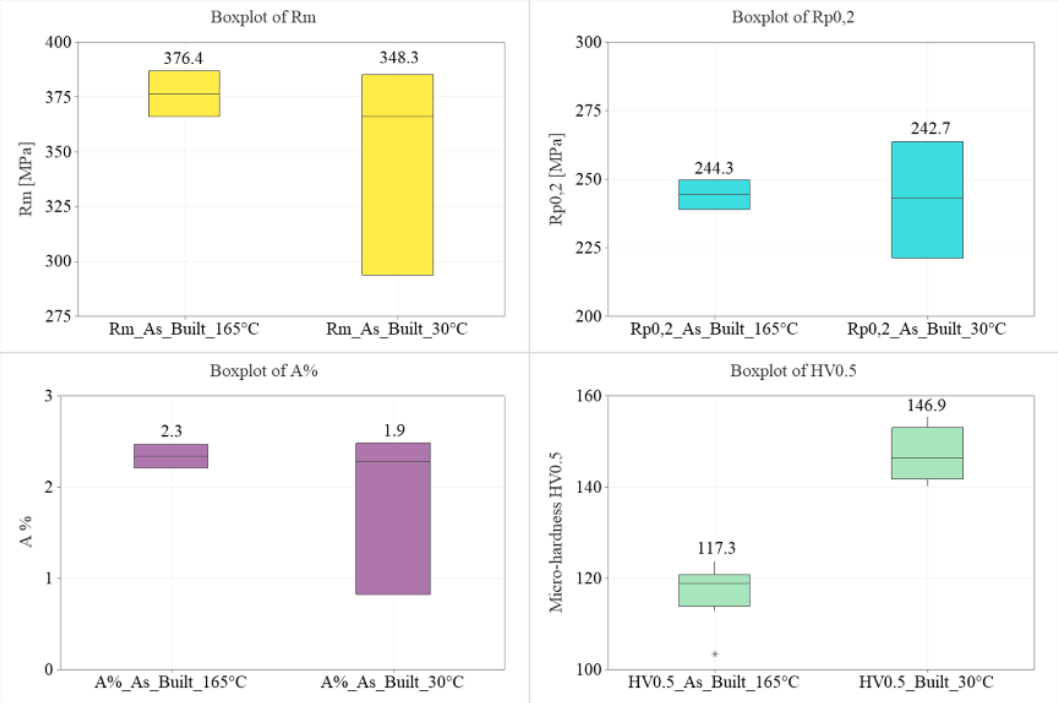

Figure 97. Boxplot for L-PBF_Scrap samples. Mechanical properties with the platform at 30 °C or 165 °C (average values).

As impact tests are regards, the best average results were noticed for AlSi9Cu3(Fe) scrap specimens in as-built and T6 conditions. Nevertheless, the standard deviation resulted high because of a certain amount of defects detected into the specimens during the fracture surface analyses.

Figure 98 reports the fracture surface observed for some impact test samples. The response in terms of porosities detected appears to be similar to the fracture surfaces after tensile tests. Similarly to what was noticed in A% values (

Figure 95), specimens of ingot type resulted the one that absorbed less energy during the rupture. Nevertheless, even the reference specimen resulted in low absorbed energy. In both elongation at rupture and impact tests, L-PBF Scrap specimens appear the best, having the highest average value results despite the high standard deviation.

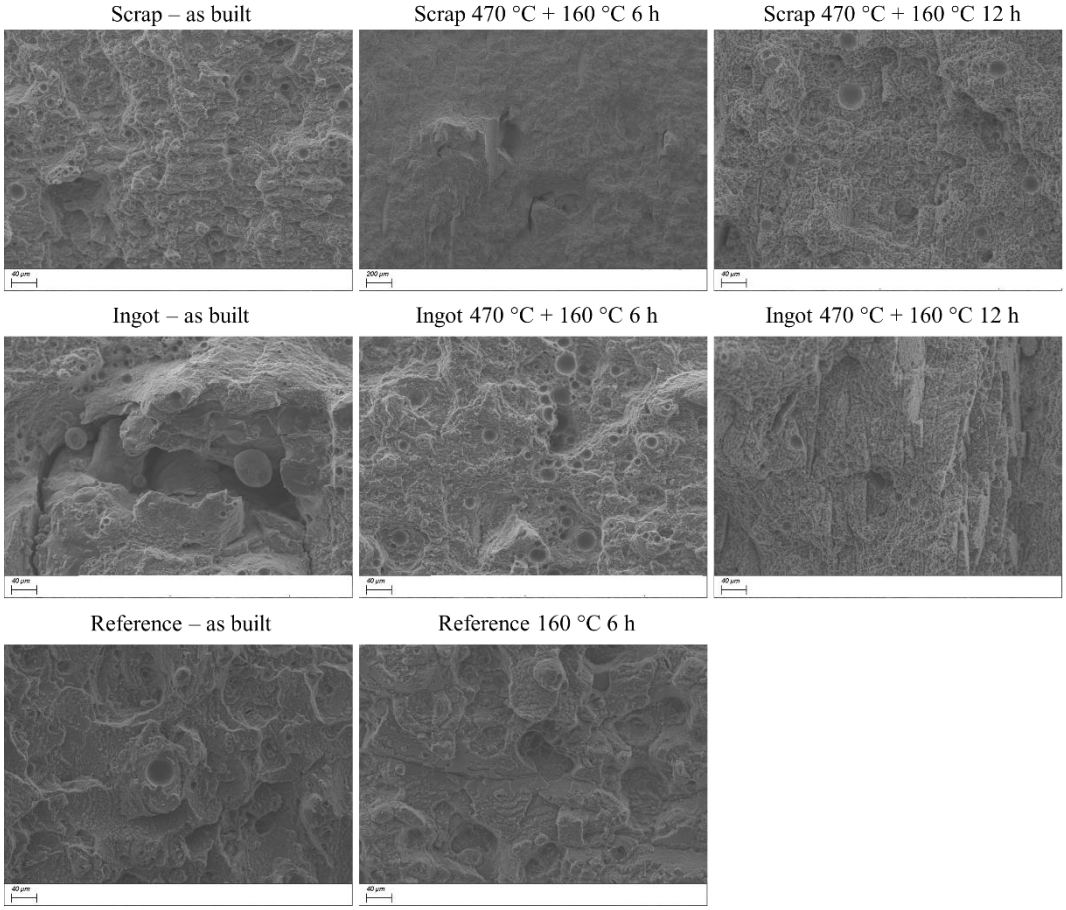

Figure 98. Fracture surfaces in impact test specimens.

6.4 Discussion

The recyclability of alloy AlSi9Cu3(Fe) through gas atomization was evaluated by producing powders starting from scrap HPDC components. To make a comparison, even the ingot alloy was atomized.

The obtained powders are characterized by very good properties in terms of rheology behaviour, compositional range and sphericity.

The powders were successfully printed by L-PBF after the printing parameter study. As the main effects regards, the L-PBF process parameters were examined to highlight the main effects with respect to the obtained density. Results are shown in

Figure 99. In particular, all the parameters have an effect on the final density of the sample; it is necessary to examine the interaction plot to highlight the significance of such main effects.

As laser power regards, an interaction between the laser power and the point distance seems to exist. Mainly, with the larger point distance of 140 µm, no effects were noticed. On the other hand, if the point distance value changes, even the speed changes, and the speed has a crucial role with respect to the density. The larger the point distance, the lower the final density of the piece.

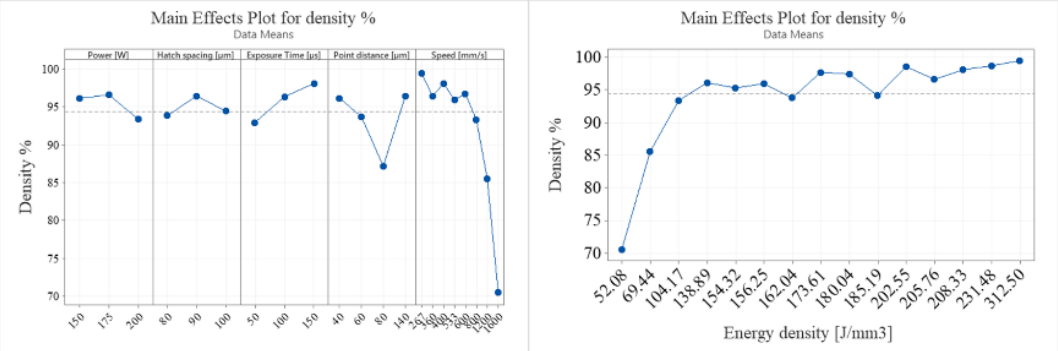

Figure 99. Main effects. Effects of process parameters on samples density

As point distance and exposure time affect the speed, the higher the exposure time, the lower the speed and the higher the final density of the printed part.

From the interaction plot, it can be noticed that the increase in speed led to a decrease in density; despite the literature for similar alloy speeds of 1200 and 1300 mm/s were used (**Table 13**). In this specific case, it can be noticed from

Figure 99 that a scanning speed of about 1200 mm/s led to a very low density of the obtained sample.

Considering the energy density (5) and the build rate (6), it is possible to compare the results with those of the state of the art.

$$E = \left[\frac{J}{mm^3}\right] = \frac{P}{v \times d \times t} \quad (5)$$

$$\mathrm{BR} = \frac{p_d \times d \times t}{exp_{time}} \quad (6)$$

The energy density formula uses the laser power P (W), the laser scan speed υ (mm/s), the hatching distance d (mm) and the layer thickness t (mm). The energy density for the printing parameter selected is shown in **Table 33**, along with a comparison with the state-of-the-art powders.

Table 33. Comparison of energy density of scrap alloy AlSi9Cu3(Fe) and state of the art in AlSi10Mg and AlSi9Cu3

Alloy type	% Density achieved	Energy density [J/mm^3]	Ref.
AlSi9Cu3(Fe)	99.50	321.5	Present work
AlSi10Mg	99.80	35.6	[157]
AlSi9Cu3	99.81	350	[96]
AlSi9Cu3	99.87	45.3	[97]

The parameters selected permit the obtaining of dense L-PBF samples, particularly in scrap alloy. Specimens printed in ingot alloy resulted in high porosity amounts; such behaviour can be attributed to the very cohesive nature of the powders, which are characterized by a very low flow index, as noticed in 6.3.1 [158].

Mechanical results resulted in higher values with respect to the alloy produced by conventional HPDC methods, thanks to the very fine microstructure.

Chapter 7

7 Conclusions and Outlook

7.1 Results

In this thesis, rejected automotive components in Al-Si alloys were successfully recycled through traditional casting methods, such as gravity casting and through advanced production processes, such as additive manufacturing. The recycling of internally rejected components has crucial importance since, in the foundry, a certain amount of scrap is produced daily.

Considering the two alloy compositions studied, various conclusions can be drawn, mainly focusing on the type of the alloy and the recycling route.

7.1.1 AlSi7Cu0.5Mg

The recycling of AlSi7Cu0.5Mg alloy can be easily performed through traditional casting, such as the Gravity Casing technique. The study has highlighted that such alloy can be successfully re-melted multiple times before degradation of the microstructure, with the coarsening of sludge particles and a moderate increase in secondary harm spacings SDAS with the increase of the re-melting processes. Particularly, re-meltings cause a gradual change in eutectic silicon shape from small and refined to coarse microstructure. An increase in micro-hardness of the eutectic phase was noticed with multiple re-melting; this behaviour can be attributed to a progressively higher probability of indenting coarse intermetallic phases.

The study, furthermore, highlights that the addition of metallic chromium inside the melt leads to a change in microstructures, mainly due to Cr-based intermetallic phases, and a severe and inhomogeneous change in eutectic microstructure can be observed already after the second re-melt.

Those results highlight that the combination of multiple re-melt and Cr addition leads to an inhomogeneous microstructure, mainly due to the high tenor of Cr addition. On the other hand, AlSi7Cu0.5Mg without Cr addition continue to show good microstructural features even after the third re-melt.

This result opens the possibility of casting components through scrap alloy instead of ingot alloy, and such scrap alloy can at least be reused up to 3 times. To better understand the mechanical properties of such recycled alloy, a comparison between the mechanical properties of alloy in ingot and scrap state of delivery, as well as castings with variable amounts of scrap alloy, was performed.

Mechanical results highlight that ingot and scrap alloys have comparable behaviours and mechanical properties in terms of uniaxial tensile tests, while alloys containing a certain amount of scrap perform better in terms of absorbed energy during impact tests.

These results open the possibility of cast components starting from defective castings even multiple times. The slight reduction in mechanical properties can eventually lead to the reserving of such alloy for products that are not excessively mechanically stressed.

7.1.2 AlSi9Cu3(Fe)

Notably, the recyclability of scraps in AlSi9Cu3(Fe) has recently started to be investigated. On the other hand, the recycling route by gravity casting of scrap AlSi9Cu3(Fe) can be challenging given the high amount of hydrogen retained in the HPDC components. In this work, the recyclability of AlSi9Cu3(Fe) was as performed through Gravity Casting without degassing and scorification processes, as for alloy AlSi7Cu0.5Mg.

Despite the results in terms of mechanical properties being good, a gravity casting procedure must be implemented to obtain dense specimens, reducing the large number of retained defects detected.

The melting and casting of such alloy composition in the form of the ingot was performed in literature through gravity casting; conversely, the melting and casting by gravity casting of scraps remain a little-explored territory. Since to be both of the Autor's knowledge, only one publication deals with the study of the re-use of rejected castings in alloy AlSi9Cu3, in this work, the alloying through metallic Cr and/or Ni was taken into account.

Re-melting tests performed on AlSi9Cu3(Fe) scraps highlight a SDAS decrease with the addition of Cr or Ni, if such elements are added separately. Nevertheless, porosities strongly affected the measured SDAS inside castings. For this reason, the gravity casting tests did not produce satisfactory results in terms of final microstructures.

Moreover, the large intermetallic phases that nucleated during the alloy solidification may hinder the aluminium melt flow inside the mould, causing pores and shrinkage.

Since results in terms of mechanical properties appear attractive, the need to perform re-melting, even adding Cr and Ni through GC using degassing systems, appears to be the best solution to highlight the feasibility of such a promising recycling route, as highlighted in 5.3.

Alloy AlSi9Cu3(Fe) was successfully gas atomized and printed through L-PBF. In particular, crack-free specimens were printed using L-PBF parameters optimization, obtaining a density of 99.4%. The cross-section of these specimens reveals a fine-grained microstructure and fine Cu-based intermetallic phases. SEM analyses reveal the presence of intermetallic phases Ni-based after the solutioning temper. Notably, the nucleation of such an intermetallic phase can affect the mechanical performance since it appears rod-shaped.

The selection of an optimal heat treatment, starting from treatments suggested in the literature for the casting alloy AlSi9Cu3(Fe), led to the selection of a heat treatment that guarantees mechanical performances and elongation at rupture without penalising the resilience. Comparing mechanical properties with the mechanical properties of the HPDC alloy, L-PBF specimens overperformed despite a certain amount of defects detected in the fracture surfaces.

7.1.3 Sustainability

Notably, the successful use of rejected parts instead of ingot alloy demonstrated the potentiality of sustainability in classical production processes such as Gravity Casting and additive manufacturing. This process, from the perspective of foundries, leads to a reduction in energy consumption and a strong reduction in carbon footprint compared to the use of ingots.

Moreover, the mechanical tests performed on recycled AlSi7Cu0.5Mg alloys resulted in properties comparable to ingot alloys and very high processability, together with clear economic benefits for aluminium foundries.

In terms of powder production, the possibility of producing powder from rejected parts results in a significant reduction of emission to produce specific additive manufacturing alloys with controlled levels of alloyed elements.

This research was able to integrate the circular economy paradigm in both casting and additive manufacturing.

7.2 Outlook

This thesis presented the primary results of the recycling of rejected scrap components coming from the automotive production process line.

From these results, the potentiality of the results in terms of circular economy in the foundry appears evident. The research also opens up the possibility of considering additive manufacturing as a possible production process for producing automotive components.

The interaction between the production process and obtained components, starting from rejected components, must be further studied by industrial facilities, such as gravity castings and HPDC, to compare the obtained results.

Additive manufacturing of powder produced starting from scraps can be further enhanced by tailoring the composition by adding alloying elements to understand the variations in the rheological properties and their printability. The composition tailoring can influence the intermetallic phases and the printability.

8 References

[1] M. Tisza, I. Czinege, Comparative study of the application of steels and aluminium in lightweight production of automotive parts, International Journal of Lightweight Materials and Manufacture 1 (2018). https://doi.org/10.1016/j.ijlmm.2018.09.001.

[2] ASTM International, ASTM B179-18 Standard Specification for Aluminum Alloys in Ingot and Molten Forms for Castings from All Casting Processes, 2018.

[3] British Standard, Aluminium and aluminium alloys – Castings – Chemical composition and mechanical properties BS EN 1706:2020+A1:2021, 2018.

[4] M. Djurdjevic, S. Manasijevic, M. Mihailović, S. Stopic, From Bauxite as a Critical Material to the Required Properties of Cast Aluminum Alloys for Use in Electro Automotive Parts, Metals (Basel) 13 (2023) 1796. https://doi.org/10.3390/met13111796.

[5] S. Al-Alimi, N.K. Yusuf, A.M. Ghaleb, M.A. Lajis, S. Shamsudin, W. Zhou, Y.M. Altharan, H.S. Abdulwahab, Y. Saif, D.H. Didane, I. S T T, A. Adam, Recycling aluminium for sustainable development: A review of different processing technologies in green manufacturing, Results in Engineering 23 (2024) 102566. https://doi.org/10.1016/j.rineng.2024.102566.

[6] L. Cabrera-Correa, L. González-Rovira, J. de Dios López-Castro, M. Castillo-Rodríguez, F.J. Botana, Effect of the heat treatment on the mechanical properties and microstructure of Scalmalloy® manufactured by Selective Laser Melting (SLM) under certified conditions, Mater Charact 196 (2023). https://doi.org/10.1016/j.matchar.2022.112549.

[7] H.R. Kotadia, G. Gibbons, A. Das, P.D. Howes, A review of Laser Powder Bed Fusion Additive Manufacturing of aluminium alloys: Microstructure and properties, Addit Manuf 46 (2021). https://doi.org/10.1016/j.addma.2021.102155.

[8] J. Piekło, A. Garbacz-Klempka, Use of selective laser melting (SLM) as a replacement for pressure die casting technology for the production of automotive casting, Archives of Foundry Engineering 21 (2021) 9–16. https://doi.org/10.24425/afe.2021.136092.

[9] G. Scampone, G. Timelli, R. Pirovano, S. Mascetti, Formation and distribution of entrainment defects in gravity AlSi7Cu0.5Mg alloy castings, Metallurgia Italiana 114 (2022).

[10] G. Timelli, F. Bonollo, The influence of Cr content on the microstructure and mechanical properties of AlSi9Cu3(Fe) die-casting alloys, Materials Science and Engineering: A 528 (2010). https://doi.org/10.1016/j.msea.2010.08.079.

[11] T. Szymczak, G. Gumienny, L. Klimek, M. Goły, T. Pacyniak, Microstructural characteristics of alsi9cu3(Fe) alloy with high melting point elements, Metals (Basel) 10 (2020). https://doi.org/10.3390/met10101278.

[12] E. Fracchia, C. Mus, Low carbon footprint aluminium components for E-Mobility, Acta Metallurgica Slovaca 30 (2024) 24–28. https://doi.org/10.36547/ams.30.1.1997.

[13] P. Xiao, S. Xu, L. Chen, Y. Liu, J. Li, Z. Xiao, X. Meng, Effect of Casting Process and Thermal Exposure on Microstructure and Mechanical Properties of Al-Si-Cu-Ni Alloy, Materials 17 (2024) 4598. https://doi.org/10.3390/ma17184598.

[14] J. Tenkamp, M. Awd, S. Siddique, P. Starke, F. Walther, Fracture–mechanical assessment of the effect of defects on the fatigue lifetime and limit in cast and additively manufactured aluminum–silicon alloys from hcf to vhcf regime, Metals (Basel) 10 (2020). https://doi.org/10.3390/met10070943.

[15] J. Zhu, Z. Luo, S. Wu, H. Yan, The effect of Sr on the microstructure and wear properties of AlSi5Cu1Mg alloy, Advances in Mechanical Engineering (2018). https://doi.org/10.1177/1687814018819536.

[16] E. Fracchia, F.S. Gobber, M. Rosso, Effect of Alloying Elements on the Sr Modification of Al-Si Cast Alloys, Metals (Basel) 11 (2021) 342. https://doi.org/10.3390/met11020342.

[17] M. Wang, W. Xu, Q. Han, Study of refinement and morphology change of AlFeSi phase in A380 alloy due to addition of Ca, Sr/ Ca, Mn and Mn, Sr, Mater Trans (2016). https://doi.org/10.2320/matertrans.M2015329.

[18] Ž. Rajić, M. Torkar, I. Paulin, B. Žužek, Č. Donik, M. Bizjak, Properties of AlSi5Cu1Mg modified with Sb, Sr and Na, Materiali in Tehnologije (2014).

[19] V. Páramo, R. Colás, E. Velasco, S. Valtierra, Spheroidization of the Al-Si eutectic in a cast aluminum alloy, J Mater Eng Perform (2000). https://doi.org/10.1361/105994900770345467.

[20] E. Ogris, A. Wahlen, H. Lüchinger, P.J. Uggowitzer, On the silicon spheroidization in Al-Si alloys, Journal of Light Metals (2002). https://doi.org/10.1016/S1471-5317(03)00010-5.

[21] M. Zavala-Arredondo, N. Boone, J. Willmott, D.T.D. Childs, P. Ivanov, K.M. Groom, K. Mumtaz, Laser diode area melting for high speed additive manufacturing of metallic components, Mater Des 117 (2017). https://doi.org/10.1016/j.matdes.2016.12.095.

[22] J. Zhang, B. Song, Q. Wei, D. Bourell, Y. Shi, A review of selective laser melting of aluminum alloys: Processing, microstructure, property and developing trends, J Mater Sci Technol 35 (2019). https://doi.org/10.1016/j.jmst.2018.09.004.

[23] N.T. Aboulkhair, M. Simonelli, L. Parry, I. Ashcroft, C. Tuck, R. Hague, 3D printing of Aluminium alloys: Additive Manufacturing of Aluminium alloys using selective laser melting, Prog Mater Sci 106 (2019). https://doi.org/10.1016/j.pmatsci.2019.100578.

[24] K. Kermeli, P.H. ter Weer, W. Crijns-Graus, E. Worrell, Energy efficiency improvement and GHG abatement in the global production of primary aluminium, Energy Effic 8 (2015). https://doi.org/10.1007/s12053-014-9301-7.

[25] The International Aluminium Institute (IAI), Aluminium industry reports decline in greenhouse gas emissions, (2024). https://international-aluminium.org/aluminium-industry-reports-decline-in-greenhouse-gas-emissions/#:~:text=This%20opportunity%20is%20met%20by,reduce%20emissions%20while%20growing%20production (accessed September 15, 2024).

[26] Ecocap's, Aluminium recycling: 2023 record year, (2024). https://www.ecocaps.com/en/aluminium-recycling-2023-record-year/ (accessed September 15, 2024).

[27] A. Rolseth, M. Carlsson, E. Ghassemali, L. Pérez Caro, A.E.W. Jarfors, Impact of functional integration and electrification on aluminium scrap in the automotive sector: A review, Resour Conserv Recycl 205 (2024). https://doi.org/10.1016/j.resconrec.2024.107532.

[28] J.C. Viala, M. Peronnet, F. Barbeau, F. Bosselet, J. Bouix, Interface chemistry in aluminium alloy castings reinforced with iron base inserts, in: Compos Part A Appl Sci Manuf, 2002. https://doi.org/10.1016/S1359-835X(02)00158-6.

[29] EPD International AB, The International EPD System, (n.d.). https://www.environdec.com/about-us/the-international-epd-system-about-the-system (accessed September 25, 2024).

[30] A.K. Tripathy, S. Mahalik, C.K. Sarangi, B.C. Tripathy, K. Sanjay, I.N. Bhattacharya, A pyro-hydrometallurgical process for the recovery of alumina from waste aluminium dross, Miner Eng 137 (2019). https://doi.org/10.1016/j.mineng.2019.04.009.

[31] F.A. Cruz Sanchez, H. Boudaoud, M. Camargo, J.M. Pearce, Plastic recycling in additive manufacturing: A systematic literature review and opportunities for the circular economy, J Clean Prod 264 (2020). https://doi.org/10.1016/j.jclepro.2020.121602.

[32] Asia's first sustainable metal powder facility has begun its operations in Singapore, (2022). https://www.edb.gov.sg/en/about-edb/media-releases-publications/molyworks-expands-global-footprint-to-setup-asias-first-sustainable-metal-powder-facility-in-Singapore.html (accessed September 25, 2024).

[33] f3nice Srl, (2024). https://f3nice.com/ (accessed October 31, 2024).

[34] R. Ding, H. Yang, S. Li, G. Hu, J. Mo, M. Chu, S. Paddea, S. Zhang, P. Zhang, Z. Liu, J. Wei, Failure analysis of H13 steel die for high pressure die casting Al alloy, Eng Fail Anal 124 (2021). https://doi.org/10.1016/j.engfailanal.2021.105330.

[35] B.K. Kosec, L. Kosec, J. Kopač, Analysis of casting die failures, Eng Fail Anal 8 (2001). https://doi.org/10.1016/S1350-6307(00)00032-7.

[36] Y. Zhang, E. Lordan, K. Dou, S. Wang, Z. Fan, Influence of porosity characteristics on the variability in mechanical properties of high pressure die casting (HPDC) AlSi7MgMn alloys, J Manuf Process 56 (2020). https://doi.org/10.1016/j.jmapro.2020.04.071.

[37] T.A. Baser, E. Umay, V. Akinci, New trends in aluminum die casting alloys for automotive applications, in: Eurasia Proceedings of Science, Technology, Engineering and Mathematics, 2022. https://doi.org/10.55549/epstem.1227541.

[38] F.C.R. Hernandez, J.M.H. Ramírez, R. Mackay, Al-Si Alloys: Automotive, Aeronautical, and Aerospace Applications, 2017. https://doi.org/10.1007/978-3-319-58380-8.

[39] G. Nicoletto, R. Konečná, S. Fintova, Characterization of microshrinkage casting defects of Al-Si alloys by X-ray computed tomography and metallography, in: Int J Fatigue, 2012. https://doi.org/10.1016/j.ijfatigue.2012.01.006.

[40] R. Gopalan, N.K. Prabhu, Oxide bifilms in aluminium alloy castings - A review, Materials Science and Technology 27 (2011). https://doi.org/10.1179/1743284711Y.0000000033.

[41] M. Réger, J. Gáti, F. Oláh, R. Horváth, E.R. Fábián, T. Bubonyi, Detection of Porosity in Impregnated Die-Cast Aluminum Alloy Piece by Metallography and Computer Tomography, Crystals (Basel) 13 (2023). https://doi.org/10.3390/cryst13071014.

[42] Y. Li, J. Liu, Q. Zhang, W. Huang, Casting defects and microstructure distribution characteristics of aluminum alloy cylinder head with complex structure, Mater Today Commun 27 (2021). https://doi.org/10.1016/j.mtcomm.2021.102416.

[43] S. Samavedam, S. Sundarrajan, Al-Si and Al-Si-Mg Cast Alloys Shrinkage Porosity Estimation, Archives of Foundry Engineering 16 (2016). https://doi.org/10.1515/afe-2016-0004.

[44] M.L. Hu, H.M. Guo, K.Y. Yang, W. jie Chang, B. Deng, J. tao Luo, Bifilm Defects in AlSi10MgMn Alloy Castings, International Journal of Metalcasting (2023). https://doi.org/10.1007/s40962-023-01207-2.

[45] N. Sultana, M. Rafiquzzaman, Y. Rahman, A. Das, Solidification and Filling Related Defects Analysis Using Casting Simulation Technique with Experimental Validation, International Journal of Mechanical Engineering and Applications 6 (2018) 150–160. https://doi.org/10.11648/j.ijmea.20180606.12.

[46] F.S. Gobber, A.G. Pisa, D. Ugues, M. Rosso, Design of a Test Rig for the Characterization of Thermal Fatigue and Soldering Resistance of the Surfaces of Tool Steels for High-Pressure Die-Casting Dies, Steel Res Int (2020). https://doi.org/10.1002/srin.201900480.

[47] T.O. Mbuya, B.O. Odera, S.P. Ng'ang'a, Influence of iron on castability and properties of aluminium silicon alloys: Literature review, International Journal of Cast Metals Research 16 (2003). https://doi.org/10.1080/13640461.2003.11819622.

[48] E. Samuel, A.M. Samuel, H.W. Doty, S. Valtierra, F.H. Samuel, Intermetallic phases in Al-Si based cast alloys: New perspective, International Journal of Cast Metals Research 27 (2014). https://doi.org/10.1179/1743133613Y.0000000083.

[49] D. Song, Y. Zhao, Y. Jia, R. Li, N. Zhou, K. Zheng, Y. Fu, W. Zhang, Study of the evolution mechanisms of Fe-rich phases in Al-Si-Fe alloys with Mn modification using synchrotron X-ray imaging, J Alloys Compd 915 (2022). https://doi.org/10.1016/j.jallcom.2022.165378.

[50] J. Kasińska, D. Bolibruchová, M. Matejka, The influence of remelting on the properties of AlSi9Cu3 alloy with higher iron content, Materials 13 (2020). https://doi.org/10.3390/ma13030575.

[51] E. Samuel, A.M. Samuel, H.W. Doty, S. Valtierra, F.H. Samuel, Highlights on the Role of Fe, Sr, and Solidification Time on Porosity Formation in Al–Si Cast Alloys, International Journal of Metalcasting (2024). https://doi.org/10.1007/s40962-024-01409-2.

[52] D. Qian, K. Lan, Y. Yang, Microstructure evolution of a novel low-silicon cast aluminum alloy modified with Mn and Cr during solution treatment, Mater Charact 217 (2024) 114319. https://doi.org/10.1016/j.matchar.2024.114319.

[53] L. Lattanzi, M. Di Giovanni, M. Giovagnoli, A. Fortini, M. Merlin, D. Casari, M. Di Sabatino, E. Cerri, G. Garagnani, Room Temperature Mechanical Properties of A356 Alloy with Ni Additions from 0.5 Wt to 2 Wt %, Metals (Basel) 8 (2018) 224. https://doi.org/10.3390/met8040224.

[54] B. Callegari, T.N. Lima, R.S. Coelho, The Influence of Alloying Elements on the Microstructure and Properties of Al-Si-Based Casting Alloys: A Review, Metals (Basel) 13 (2023). https://doi.org/10.3390/met13071174.

[55] L.-W. Xue, H.-L. Jia, P. Ma, J.-W. Song, M. Zha, H.-Y. Wang, Influence of Mg and Cu on precipitation behaviors and mechanical properties of Al-Si Alloys, Materials Science and Engineering: A (2024) 146775. https://doi.org/10.1016/j.msea.2024.146775.

[56] A. Bobel, K. Kim, C. Wolverton, M. Walker, G.B. Olson, Equilibrium composition variation of Q-phase precipitates in aluminum alloys, Acta Mater 138 (2017). https://doi.org/10.1016/j.actamat.2017.07.048.

[57] E. Aghaie, D. Sediako, Properties of various phases in Al powertrain alloys: A review, in: Materials Science and Technology 2018, MS and T 2018, 2019. https://doi.org/10.7449/2018/MST_2018_966_973.

[58] L. Zuo, B. Ye, J. Feng, X. Kong, H. Jiang, W. Ding, Effect of Q-Al5Cu2Mg8Si6 phase on mechanical properties of Al-Si-Cu-Mg alloy at elevated temperature, Materials Science and Engineering: A 693 (2017). https://doi.org/10.1016/j.msea.2017.03.087.

[59] C. Puncreobutr, P.D. Lee, K.M. Kareh, T. Connolley, J.L. Fife, A.B. Phillion, Influence of Fe-rich intermetallics on solidification defects in Al-Si-Cu alloys, Acta Mater 68 (2014). https://doi.org/10.1016/j.actamat.2014.01.007.

[60] J.A. Taylor, G.B. Schaffer, D.H. StJohn, The role of iron in the formation of porosity in Al-Si-Cu-based casting alloys: Part I. Initial experimental observations, Metall Mater Trans A Phys Metall Mater Sci 30 (1999). https://doi.org/10.1007/s11661-999-0101-1.

[61] E. Gariboldi, J.N. Lemke, L. Rovatti, O. Baer, G. Timelli, F. Bonollo, High-temperature behavior of high-pressure diecast alloys based on the Al-Si-Cu system: The role played by chemical composition, Metals (Basel) 8 (2018). https://doi.org/10.3390/met8050348.

[62] L. Ceschini, A. Morri, S. Toschi, A. Bjurenstedt, S. Seifeddine, Influence of sludge particles on the fatigue behavior of Al-Si-Cu secondary aluminium casting alloys, Metals (Basel) 8 (2018). https://doi.org/10.3390/met8040268.

[63] E. Granhed, A. De Mori, E. Battaglia, L. Arnberg, G. Lindwall, A CALPHAD-Based Investigation of the Sludge Factor, International Journal of Metalcasting 18 (2024). https://doi.org/10.1007/s40962-023-01018-5.

[64] I. Švecová, E. Tillová, L. Kuchariková, V. Knap, Possibilities of predicting undesirable iron intermetallic phases in secondary Al-alloys, in: Transportation Research Procedia, 2021. https://doi.org/10.1016/j.trpro.2021.07.047.

[65] J.A. Taylor, Iron-Containing Intermetallic Phases in Al-Si Based Casting Alloys, Procedia Materials Science 1 (2012). https://doi.org/10.1016/j.mspro.2012.06.004.

[66] P. Krall, I. Weißensteiner, S. Pogatscher, Recycling aluminum alloys for the automotive industry: Breaking the source-sink paradigm, Resour Conserv Recycl 202 (2024) 107370. https://doi.org/10.1016/j.resconrec.2023.107370.

[67] D. Raabe, D. Ponge, P.J. Uggowitzer, M. Roscher, M. Paolantonio, C. Liu, H. Antrekowitsch, E. Kozeschnik, D. Seidmann, B. Gault, F. De Geuser, A. Deschamps, C. Hutchinson, C. Liu, Z. Li, P. Prangnell, J. Robson, P. Shanthraj, S. Vakili, C. Sinclair, L. Bourgeois, S. Pogatscher, Making sustainable aluminum by recycling scrap: The science of "dirty" alloys, Prog Mater Sci 128 (2022). https://doi.org/10.1016/j.pmatsci.2022.100947.

[68] D. Bolibruchová, M. Matejka, M. Kuriš, Analysis of the Impact of the Change of Primary and Secondary AlSi9Cu3 Alloy Ratio in the Batch on its Performance, Manufacturing Technology 19 (2019). https://doi.org/10.21062/ujep/363.2019/a/1213-2489/mt/19/5/734.

[69] P. Noga, L. Tuz, K. Żaba, A. Zwoliński, Analysis of microstructure and mechanical properties of alsi11 after chip recycling, co-extrusion, and arc welding, Materials 14 (2021). https://doi.org/10.3390/ma14113124.

[70] R.P. Barot, M.P. Sutaria, Effect of multiple remelting on behaviour of AlSi5Cu3 Aluminium alloy, in: Mater Today Proc, 2022. https://doi.org/10.1016/j.matpr.2022.04.608.

[71] R. Honzátko, Š. Michna, J. Cais, The influence of porosity on mechanical properties of casts produced from Al - Si Alloys, Manufacturing Technology 13 (2013). https://doi.org/10.21062/ujep/x.2013/a/1213-2489/mt/13/3/319.

[72] M. Žbontar, M. Petrič, P. Mrvar, The influence of cooling rate on microstructure and mechanical properties of alsi9cu3, Metals (Basel) 11 (2021). https://doi.org/10.3390/met11020186.

[73] A.K. Prasada Rao, W.Q. Ain, M.K. Faisal, B.I. Mazni, Undiluted Recycling of Aluminum Scrap Alloy Using Hume-Rothery's Rule, Metallography, Microstructure, and Analysis 7 (2018). https://doi.org/10.1007/s13632-018-0431-8.

[74] G. Niu, Y. Wang, L. Zhu, J. Ye, J. Mao, Fluidity of casting Al–Si series alloys for automotive light-weighting: a systematic review, Materials Science and Technology (United Kingdom) 38 (2022). https://doi.org/10.1080/02670836.2022.2068274.

[75] M. Matvija, M. Fujda, O. Milkovič, M. Vojtko, R. Kočiško, M. Glogovský, Microstructure Changes and Improvement in the Mechanical Properties of As-Cast AlSi7MgCu0.5 Alloy Induced by the Heat Treatment and ECAP Technique at Room Temperature, Advances in Materials Science and Engineering 2018 (2018). https://doi.org/10.1155/2018/5697986.

[76] M. Matvija, M. Fujda, M. Vojtko, R. Kočiško, Homogenization of AlSi7MgCu0.5 alloy as-cast structure by ECAP processing, in: Materials Science Forum, 2014. https://doi.org/10.4028/www.scientific.net/MSF.782.390.

[77] R. Wang, C.B. Gonzalez, B. Stauder, R.F. Gutiérrez, M. Albu, S. Sommadossi, E. Povoden-Karadeniz, M.C. Poletti, Influence of the heat treatment path on the precipitation sequence in an AlSi7Cu0.5Mg-alloy, J Alloys Compd 990 (2024). https://doi.org/10.1016/j.jallcom.2024.174450.

[78] E. Kilinc, Y. Birol, Optimising the T6 heat treatment for gravity cast AlSi7MgCu0.5 alloy V8 cylinder heads, International Journal of Cast Metals Research 30 (2017). https://doi.org/10.1080/13640461.2017.1290309.

[79] H. Nunes, O. Emadinia, M. F. Vieira, A. Reis, Low- and High-Pressure Casting Aluminum Alloys: A Review, in: Recent Advancements in Aluminum Alloys, 2024. https://doi.org/10.5772/intechopen.109869.

[80] B. Dybowski, A. Kiełbus, Ł. Poloczek, Effects of die-casting defects on the blister formation in high-pressure die-casting aluminum structural components, Eng Fail Anal 150 (2023). https://doi.org/10.1016/j.engfailanal.2023.107223.

[81] R. Wang, C.B. Gonzalez, B. Stauder, R.F. Gutiérrez, M. Albu, S. Sommadossi, E. Povoden-Karadeniz, M.C. Poletti, Influence of the heat treatment path on the precipitation sequence in an AlSi7Cu0.5Mg-alloy, J Alloys Compd 990 (2024) 174450. https://doi.org/10.1016/j.jallcom.2024.174450.

[82] R.N. Lumley, D.R. Gunasegaram, M. Gershenzon, R.G. O'donnell, Effect of alloying elements on heat treatment response of aluminium high pressure die castings, International Heat Treatment and Surface Engineering 4 (2010). https://doi.org/10.1179/174951409X12542264514004.

[83] L. Hurtalová, E. Tillová, M. Chalupová, The structure analysis of secondary (Recycled) AlSi9Cu3 cast alloy with and without heat treatment, Engineering Transactions 61 (2013).

[84] R. Wang, D. Ram, B. Stauder, R.F. Gutiérrez, E. Gariboldi, M.C. Poletti, Stress Relaxation during Artificial Aging of an AlSi7Cu0.5Mg Cast Alloy, Crystals (Basel) 12 (2022). https://doi.org/10.3390/cryst12081168.

[85] L. Hurtalová, E. Tillová, M. Chalupová, Identification and analysis of intermetallic phases in age-hardened recycled AlSi9Cu3 cast alloy, Archive of Mechanical Engineering 59 (2012). https://doi.org/10.2478/v10180-012-0020-3.

[86] P.N. Anyalebechi, Techniques for determination of the Hydrogen Content in Aluminium and its Alloys—a Review, Cast Metals 3 (1990) 182–201. https://doi.org/10.1080/09534962.1990.11819039.

[87] B. Chokkalingam, S. Boovendravarman, R. Tamilselvan, V. Raja, APPLICATION OF ISHIKAWA DIAGRAM TO INVESTIGATE SIGNIFICANT FACTORS CAUSING ROUGH SURFACE ON SAND CASTING, Proceedings on Engineering Sciences 2 (2020). https://doi.org/10.24874/PES02.04.002.

[88] R. Montanari, A. Palombi, M. Richetta, A. Varone, Additive Manufacturing of Aluminum Alloys for Aeronautic Applications: Advantages and Problems, Metals (Basel) 13 (2023). https://doi.org/10.3390/met13040716.

[89] Y. Mao, H. Chen, J. Xiong, Research progress in laser additive manufacturing of aluminum alloys: Microstructure, defect, and properties, Journal of Materials Research and Technology 30 (2024). https://doi.org/10.1016/j.jmrt.2024.03.099.

[90] Exactitude Consultancy, Global High-Performance Aluminium Alloys Market Expected to Experience Strong Growth by 2031, (2024). https://www.globenewswire.com/news-release/2024/09/24/2952153/0/en/Global-High-Performance-Aluminium-Alloys-Market-

Expected-to-Experience-Strong-Growth-by-2031-Exactitude-Consultancy.html (accessed September 25, 2024).

[91] FIA 2024 Fédération Internationale de l'Automobile, 2026 FORMULA 1 TECHNICAL REGULATIONS, (2024). https://www.fia.com/sites/default/files/fia_2026_formula_1_technical_regulations_issue_8_-_2024-06-24.pdf (accessed September 24, 2024).

[92] J. Wang, M. Xia, J. Wu, C. Ge, Ladle Nozzle Clogging in Vacuum Induction Melting Gas Atomization: Influence of the Melt Viscosity, Metallurgical and Materials Transactions B: Process Metallurgy and Materials Processing Science 53 (2022). https://doi.org/10.1007/s11663-022-02537-y.

[93] W.E. Frazier, Metal additive manufacturing: A review, J Mater Eng Perform 23 (2014). https://doi.org/10.1007/s11665-014-0958-z.

[94] M.S. Kenevisi, Y. Yu, F. Lin, A review on additive manufacturing of Al–Cu (2xxx) aluminium alloys, processes and defects, Materials Science and Technology (United Kingdom) 37 (2021). https://doi.org/10.1080/02670836.2021.1958487.

[95] Y. Huang, T.G. Fleming, S.J. Clark, S. Marussi, K. Fezzaa, J. Thiyagalingam, C.L.A. Leung, P.D. Lee, Keyhole fluctuation and pore formation mechanisms during laser powder bed fusion additive manufacturing, Nat Commun 13 (2022). https://doi.org/10.1038/s41467-022-28694-x.

[96] J. Suchy, L. Pantelejev, D. Palousek, D. Koutny, J. Kaiser, Processing of AlSi9Cu3 alloy by selective laser melting, Powder Metallurgy 63 (2020) 197–211. https://doi.org/10.1080/00325899.2020.1792675.

[97] J. Fiocchi, C.A. Biffi, A. Tuissi, Selective laser melting of high-strength primary AlSi9Cu3 alloy: Processability, microstructure, and mechanical properties, Mater Des 191 (2020). https://doi.org/10.1016/j.matdes.2020.108581.

[98] L. Deillon, F. Jensch, F. Palm, M. Bambach, A new high strength Al–Mg–Sc alloy for laser powder bed fusion with calcium addition to effectively prevent magnesium evaporation, J Mater Process Technol 300 (2022). https://doi.org/10.1016/j.jmatprotec.2021.117416.

[99] R.M. Gouveia, F.J.G. Silva, E. Atzeni, D. Sormaz, J.L. Alves, A.B. Pereira, Effect of scan strategies and use of support structures on surface quality and hardness of L-PBF AlSi10Mg parts, Materials 13 (2020). https://doi.org/10.3390/ma13102248.

[100] M. Rafieazad, P. Fathi, M. Mohammadi, A. Nasiri, Effects of Laser-Powder Bed Fusion Process Parameters on the Microstructure and Corrosion Properties of AlSi10Mg Alloy, J Electrochem Soc 168 (2021). https://doi.org/10.1149/1945-7111/abdfa8.

[101] R. Konecna, F. Uriati, G. Nicoletto, V. Tibor, Surface quality and fatigue behavior of L-PBF AlSi10Mg in as-built condition, in: Procedia Structural Integrity, 2021. https://doi.org/10.1016/j.prostr.2021.12.020.

[102] Z.Y. Chua, S.K. Moon, L. Jiao, I.H. Ahn, Geometric influence of the laser-based powder bed fusion process in Ti6AL4V and AlSi10Mg, International Journal of Advanced Manufacturing Technology 114 (2021). https://doi.org/10.1007/s00170-021-07089-0.

[103] S. Lorenzi, M. Cabrini, A. Carrozza, L. Gritti, L. Nani, T. Pastore, T. Tirelli, On the selective corrosion mechanism of LPBF-produced AlSi10Mg: Potentiostatic polarization effects, Electrochim Acta 470 (2023). https://doi.org/10.1016/j.electacta.2023.143354.

[104] Eos GmbH, EOS Aluminium AlSi10Mg, Https://Www.Eos.Info/En-Us/Metal-Solutions/Metal-Materials/Aluminium#eos-Aluminium-Alsi10mg (2024).

[105] Carpenter additive, PowderRange AlSi10Mg, Https://Www.Carpenteradditive.Com/Hubfs/Resources/Datasheets%202023/PowderRange_AlSi10Mg_DataSheet.Pdf (2024).

[106] Nikon SLM Solutions, MATERIAL DATA SHEET AlSi10Mg, Https://Www.Slm-Solutions.Com/Fileadmin/Content/Powder/MDS/Nw/2024/MDS_AlSi10Mg_2024-04.1_EN.Pdf (2024).

[107] M. Roudnická, O. Molnárová, D. Dvorský, L. Křivský, D. Vojtěch, Specific Response of Additively Manufactured AlSi9Cu3Fe Alloy to Precipitation Strengthening, Metals and Materials International 26 (2020) 1168–1181. https://doi.org/10.1007/s12540-019-00504-y.

[108] M. Fousova, V. Valesova, D. Vojtech, Corrosion of 3D-Printed AlSi9Cu3Fe Alloy, 2019.

[109] J. Fiocchi, C. Colombo, L.M. Vergani, A. Fabrizi, G. Timelli, A. Tuissi, C.A. Biffi, materials Heat Treatments for Stress Relieving AlSi9Cu3 Alloy Produced by Laser Powder Bed Fusion, (2021). https://doi.org/10.3390/ma.

[110] M. Fousova, D. Dvorsky, M. Vronka, D. Vojtech, P. Lejcek, The use of selective laser melting to increase the performance of AlSi9Cu3Fe alloy, Materials 11 (2018). https://doi.org/10.3390/ma11101918.

[111] m4p - Metals for Printing, m4p ™ AlSi9Cu3, Https://Www.Metals4printing.Com/Wp-Content/Uploads/2021/Data_Sheets/EN/Al-Base/02_m4p_DataSheet_AlSi9Cu3_EN.Pdf (2024).

[112] F. Alghamdi, X. Song, A. Hadadzadeh, B. Shalchi-Amirkhiz, M. Mohammadi, M. Haghshenas, Post heat treatment of additive manufactured AlSi10Mg: On silicon morphology, texture and small-scale properties, Materials Science and Engineering: A 783 (2020). https://doi.org/10.1016/j.msea.2020.139296.

[113] M. Roudnicka, D. Dvorsky, D. Vojtech, The effect of heat treatment on the microstructure and mechanical properties of 3D-printed AlSi9Cu3Fe alloy, in: IOP Conf Ser Mater Sci Eng, Institute of Physics Publishing, 2018. https://doi.org/10.1088/1757-899X/461/1/012071.

[114] F. Marinucci, A. Aversa, D. Manfredi, M. Lombardi, P. Fino, Evaluation of a Laboratory-Scale Gas-Atomized AlSi10Mg Powder and a Commercial-Grade Counterpart for Laser Powder Bed Fusion Processing, Materials 15 (2022). https://doi.org/10.3390/ma15217565.

[115] J.A. Slotwinski, E.J. Garboczi, P.E. Stutzman, C.F. Ferraris, S.S. Watson, M.A. Peltz, Characterization of metal powders used for additive manufacturing, J Res Natl Inst Stand Technol 119 (2014). https://doi.org/10.6028/jres.119.018.

[116] J. Zegzulka, D. Gelnar, L. Jezerska, R. Prokes, J. Rozbroj, Characterization and flowability methods for metal powders, Sci Rep 10 (2020) 21004. https://doi.org/10.1038/s41598-020-77974-3.

[117] J. Clayton, D. Millington-Smith, B. Armstrong, The Application of Powder Rheology in Additive Manufacturing, JOM 67 (2015). https://doi.org/10.1007/s11837-015-1293-z.

[118] L. Wirths, M. Bleckmann, K. Paetzold, A structured approach to reduce design iterations in additive manufacturing, in: Proceedings of the Design Society, 2021. https://doi.org/10.1017/pds.2021.24.

[119] E. Fracchia, M. Rosso, Development and Characterization of New Functionally Graded Aluminium Alloys, in: Aluminium Alloys - Design and Development of Innovative Alloys, Manufacturing Processes and Applications, 2022. https://doi.org/10.5772/intechopen.101022.

[120] Z. Chen, K. Liu, E. Elgallad, F. Breton, X.G. Chen, Differential scanning calorimetry fingerprints of various heat-treatment tempers of different aluminum alloys, Metals (Basel) 10 (2020). https://doi.org/10.3390/met10060763.

[121] X. Dong, S. Amirkhanlou, S. Ji, Formation of strength platform in cast Al–Si–Mg–Cu alloys, Sci Rep 9 (2019). https://doi.org/10.1038/s41598-019-46134-7.

[122] J. Piątkowski, R. Przeliorz, J. Szymszal, The application of ATD and DSC methods to study of the EN AC-48000 alloy phase transformations, Archives of Foundry Engineering (2017). https://doi.org/10.1515/afe-2017-0076.

[123] G. Wang, Q. Sun, L. Feng, L. Hui, C. Jing, Influence of Cu content on ageing behavior of AlSiMgCu cast alloys, Mater Des 28 (2007). https://doi.org/10.1016/j.matdes.2005.11.015.

[124] S. Ferraro, A. Bjurenstedt, S. Seifeddine, On the Formation of Sludge Intermetallic Particles in Secondary Aluminum Alloys, Metall Mater Trans A Phys Metall Mater Sci 46 (2015). https://doi.org/10.1007/s11661-015-2942-0.

[125] I. Sadeghi, M.A. Wells, S. Esmaeili, Effect of particle shape and size distribution on the dissolution behavior of Al2Cu particles during homogenization in aluminum casting alloy Al-Si-Cu-Mg, J Mater Process Technol 251 (2018). https://doi.org/10.1016/j.jmatprotec.2017.08.042.

[126] E. Sjölander, S. Seifeddine, The heat treatment of Al-Si-Cu-Mg casting alloys, J Mater Process Technol (2010). https://doi.org/10.1016/j.jmatprotec.2010.03.020.

[127] L.A. Dobrzañski, R. Maniara, J.. H. Sokolowski, The effect of cooling rate on microstructure and mechanical properties of AC AlSi9Cu alloy, Archives of Materials Science and Engineering 28 (2007).

[128] V.A. Aranda, I.A. Figueroa, G. González, J.A. García-Hinojosa, I. Alfonso, Study of the microstructure and mechanical properties of Al-Si-Fe with additions of chromium by suction casting, J Alloys Compd 853 (2021). https://doi.org/10.1016/j.jallcom.2020.157155.

[129] K. Singh, B.P. Kashyap, Effects of Remelting on Variations in Composition, Microstructure, and Hardness Property of Binary Al-Si Alloys, J Mater Eng Perform 32 (2023). https://doi.org/10.1007/s11665-022-07323-0.

[130] F.S. Gobber, E. Fracchia, R. Spotorno, A. Fais, D. Manfredi, Wear and corrosion resistance of alsi10mg–cp–ti metal–metal composite materials produced by electro-sinter-forging, Materials 14 (2021). https://doi.org/10.3390/ma14226761.

[131] J. Piątkowski, R. Przeliorz, A. Gontarczyk, The Study of Phase Transformations of AlSi9Cu3 Alloy by DSC Method, Archives of Foundry Engineering 16 (2016) 109–112. https://doi.org/10.1515/afe-2016-0093.

[132] D.H. Kim, J.H. Kim, E. Kobayashi, Enhanced mechanical properties of Al–Si–Cu–Mg(-Fe) alloys by a deformation-semisolid extrusion process, Materials Science and Engineering: A 825 (2021). https://doi.org/10.1016/j.msea.2021.141667.

[133] S.W. Choi, H.S. Cho, S. Kumai, Influence of precipitation on the coefficient of thermal expansion of Al-Si-Mg-Cu-(Ti) alloys, J Alloys Compd 655 (2016). https://doi.org/10.1016/j.jallcom.2015.09.207.

[134] Y. Fu, G.G. Wang, A. Hu, Y. Li, K.B. Thacker, J.P. Weiler, H. Hu, Formation, characteristics and control of sludge in Al-containing magnesium alloys: An overview, Journal of Magnesium and Alloys 10 (2022). https://doi.org/10.1016/j.jma.2021.11.031.

[135] M. Warmuzek, Chemical composition of the Ni-containing intermetallic phases in the multicomponent Al alloys, J Alloys Compd 604 (2014). https://doi.org/10.1016/j.jallcom.2014.03.119.

[136] Y. Zedan, A.M. Samuel, H.W. Doty, V. Songmene, F.H. Samuel, Effects of Free-Cutting Elements Addition on the Microstructure, Hardness, and Machinability of Al-11%Si–Cu–Mg Casting Alloys, International Journal of Metalcasting 16 (2022). https://doi.org/10.1007/s40962-021-00740-2.

[137] V.S. Grebenkin, T. V. Sil'chenko, A.A. Gorshkov, I.Y. Dzykovich, Effect of magnesium on the distribution of tin and lead in Al-Si alloys, Metal Science and Heat Treatment 14 (1972). https://doi.org/10.1007/BF00690773.

[138] A. Biswas, D.J. Siegel, D.N. Seidman, Compositional evolution of Q-phase precipitates in an aluminum alloy, Acta Mater 75 (2014). https://doi.org/10.1016/j.actamat.2014.05.001.

[139] T. Bogdanoff, A.K. Dahle, S. Seifeddine, Effect of Co and Ni Addition on the Microstructure and Mechanical Properties at Room and Elevated Temperature of an Al–7%Si Alloy, International Journal of Metalcasting 12 (2018). https://doi.org/10.1007/s40962-017-0178-z.

[140] A. Samuel, Y. Zedan, H. Doty, V. Songmene, F.H. Samuel, A Review Study on the Main Sources of Porosity in Al-Si Cast Alloys, Advances in Materials Science and Engineering 2021 (2021). https://doi.org/10.1155/2021/1921603.

[141] H. Okamoto, Al-Cr (Aluminum-Chromium), J Phase Equilibria Diffus 29 (2008). https://doi.org/10.1007/s11669-007-9225-4.

[142] A. Almeida, R. Vilar, Al-Al7Cr eutectic in Al-Cr alloys synthesized by laser alloying, Scr Mater 63 (2010). https://doi.org/10.1016/j.scriptamat.2010.06.022.

[143] R. Zhu, W. Chen, X. Li, Z. Chen, Y. Sui, Y. Qu, Effect of Ni on microstructure and mechanical properties of Al-Cu-Mn alloy, Mater Today Commun 38 (2024). https://doi.org/10.1016/j.mtcomm.2023.107964.

[144] M.H. Abdelaziz, E.M. Elgallad, H.W. Doty, F.H. Samuel, Strengthening precipitates and mechanical performance of Al–Si–Cu–Mg cast alloys containing transition elements, Materials Science and Engineering: A 820 (2021). https://doi.org/10.1016/j.msea.2021.141497.

[145] J. Šmalc, M. Vončina, P. Mrvar, T. Balaško, V. Krutiš, M. Petrič, The Influence of Foundry Scrap Returns on Chemical Composition and Microstructure Development of AlSi9Cu3 Alloy, Crystals (Basel) 13 (2023). https://doi.org/10.3390/cryst13050757.

[146] M. Coşkun, K.C. Dizdar, G. Tarakçi, G. Özer, D. Dispinar, Recycling of additive manufactured AlSi10Mg and its effect on mechanical properties, Mater Chem Phys 289 (2022). https://doi.org/10.1016/j.matchemphys.2022.126411.

[147] V. Yakubov, H. Ostergaard, S. Bhagavath, C.L.A. Leung, J. Hughes, E. Yasa, M. Khezri, S.K. Löschke, Q. Li, A.M. Paradowska, Recycled aluminium feedstock in metal additive manufacturing: A state of the art review, Heliyon 10 (2024) e27243. https://doi.org/10.1016/j.heliyon.2024.e27243.

[148] H. Barhoumi, S. Souissi, M. Ben Amar, F. Elhalouani, Influence of heat treatment on the microstructures and mechanical properties of squeeze cast AlSi9Cu3 alloys, International Journal of Microstructure and Materials Properties 10 (2015). https://doi.org/10.1504/IJMMP.2015.074999.

[149] F. Chu, K. Zhang, H. Shen, M. Liu, W. Huang, X. Zhang, E. Liang, Z. Zhou, L. Lei, J. Hou, A. Huang, Influence of satellite and agglomeration of powder on the processability of AlSi10Mg powder in Laser Powder Bed Fusion, Journal of Materials Research and Technology 11 (2021). https://doi.org/10.1016/j.jmrt.2021.02.015.

[150] J.A. Muñiz-Lerma, A. Nommeots-Nomm, K.E. Waters, M. Brochu, A comprehensive approach to powder feedstock characterization for powder bed fusion additive

manufacturing: A case study on AlSi7Mg, Materials 11 (2018). https://doi.org/10.3390/ma11122386.

[151] D. Langlais, V. Demers, V. Brailovski, Rheology of dry powders and metal injection molding feedstocks formulated on their base, Powder Technol 396 (2022). https://doi.org/10.1016/j.powtec.2021.10.039.

[152] R. Freeman, X. Fu, Characterisation of powder bulk, dynamic flow and shear properties in relation to die filling, in: Advances in Powder Metallurgy and Particulate Materials - 2008, Proceedings of the 2008 World Congress on Powder Metallurgy and Particulate Materials, PowderMet 2008, 2008.

[153] N. Huber, J. Heerens, On the effect of a general residual stress state on indentation and hardness testing, Acta Mater 56 (2008). https://doi.org/10.1016/j.actamat.2008.08.029.

[154] M. Varmazyar, S. Yousefzadeh, M.M. Sheikhi, Effect of Ni on Microstructure and Creep Behavior of A356 Aluminum Alloy, Metals and Materials International 28 (2022). https://doi.org/10.1007/s12540-020-00892-6.

[155] G. Di Egidio, L. Ceschini, A. Morri, M. Zanni, Room- and High-Temperature Fatigue Strength of the T5 and Rapid T6 Heat-Treated AlSi10Mg Alloy Produced by Laser-Based Powder Bed Fusion, Metals (Basel) 13 (2023). https://doi.org/10.3390/met13020263.

[156] K. Ma, H. Wen, T. Hu, T.D. Topping, D. Isheim, D.N. Seidman, E.J. Lavernia, J.M. Schoenung, Mechanical behavior and strengthening mechanisms in ultrafine grain precipitation-strengthened aluminum alloy, Acta Mater 62 (2014). https://doi.org/10.1016/j.actamat.2013.09.042.

[157] F. Trevisan, F. Calignano, M. Lorusso, J. Pakkanen, A. Aversa, E.P. Ambrosio, M. Lombardi, P. Fino, D. Manfredi, On the selective laser melting (SLM) of the AlSi10Mg alloy: Process, microstructure, and mechanical properties, Materials 10 (2017). https://doi.org/10.3390/ma10010076.

[158] G. Bernard-Granger, M. Giraud, E. Pascal, L. Mailhan, T. Larsson, C. Valot, C. Ablitzer, C. Gatumel, H. Berthiaux, Rheological properties of alumina powder mixtures investigated using shear tests, Powder Technol 345 (2019). https://doi.org/10.1016/j.powtec.2019.01.027.